

NORTHWESTERN UNIVERSITY

Electronic and Structural Studies of DNA Hairpins and Quadruplexes

A DISSERTATION

SUBMITTED TO THE GRADUATE SCHOOL
IN PARTIAL FULLFILLMENT OF THE REQUIREMENTS

for the degree

DOCTOR OF PHILOSOPHY

Field of Chemistry

By

HUIHE ZHU

EVANSTON, ILLINOIS

December 2007

ABSTRACT**Electronic and Structural Studies in DNA Hairpins and Quadruplexes****Huihe Zhu**

Theoretical analysis of DNA bridge-mediated electron transfer (ET) led to the proposal that photoinduced ET might occur via either superexchange or hopping mechanisms. Electron transfer has been proposed to occur via a superexchange mechanism at short distances and via a hopping mechanism at longer distances. However, a crossover in mechanism has not been directly observed for photoinduced charge transfer in DNA. Using multiple spectroscopic techniques, a detailed analysis of the formation and decay of the stilbene acceptor singlet state and of the charge separated intermediates has been carried out for synthetic DNA hairpins possessing donor and acceptor stilbenes. Studies have shown that the superexchange mechanism is adopted at short bridge distance ($R \approx 10 \text{ \AA}$), while the hole hopping mechanism is dominant when the number of intervening base pairs is three or more. The charge separation, and charge recombination processes are distance dependent, whereas the hole injection and hole trapping are only dependent upon their energetics. Hole migration rates estimated from hole arrival times indicate a low hole mobility in DNA A-tracts.

Tri- or hexa- ethyleneglycol linked hairpins have been designed to prevent competitive absorption from natural nucleobases and chromophoric linkers. The thermal stability studies show both linkers can construct stable hairpins as short as 5 base pairs. The length of the linkers

determine the thermal stability of constructed hairpins due to the impact on base pairing conformations in two types of hairpins as shown by spectroscopic studies and molecular dynamic calculations.

Structures of DNA oligonucleotides are closely related to their biological functions, such as the inhibition of telomerase and thrombin activity by DNA quadruplex structures. Detection of quadruplex formation has been well studied for quadruplexes associated via intramolecular folding or dimerization of hairpin structures. Our work reports studies on intermolecular quadruplex association via monitoring excimer fluorescence of pyrene probed G-rich sequences. In general, chair-type quadruplex structures show high affinity and inhibition to thrombin. Thrombin binding agents possessing modified loop regions have been designed and synthesized. A two-step unfolding mechanism has been proposed and investigated via different spectroscopic techniques.

ACKNOWLEDGEMENTS

I would like to thank Professor Frederick D. Lewis for his guidance and support for my study for the last five years. I have been encouraged by his insight and passion for pursuing truth with a peaceful and steady heart. Moreover, Dr. Lewis has set me an example of being patient, considerate, and supportive toward others, and strongly disciplined toward oneself. His values will influence and benefit me for my life time. Also, I would like to thank every individual in the Lewis group, current and former. Without their help, my work would not have come this far. In particular, I would like to thank Dr. Pierre Daublain for doing kinetics modeling and Dr. Ligang Zhang for guiding my initial work in the lab. I would like to give my special thanks to our productive and loyal collaborators, Professor Wasielewski and Dr. Bioko Cohen, Professor Schatz and Martin McCullagh at Northwestern University, Professor Fiebig, Milen Raytchev and Qiang Wang at Boston College, and Professor Shafirovich at New York University. Last of all, I would like to thank my family for enabling me to finish my Ph.D. study with their continuous love, encouragement, and support.

LIST OF ABBREVIATIONS

Acr	9-Amino-6-Chloro-2-methoxyacridine
Ap	2-Aminopurine
bp	base pair
CD	Circular Dichroism
ddH ₂ O	double distilled H ₂ O
DMAP	4-Dimethylamino Pyridine
DMSO	Dimethylformamide
DMT	4,4'-Dimethoxyl Trityl
<i>E. Coli.</i>	Escherichia coli
Ea	Ethidium
EC-CD	Exciton Coupled - Circular Dichroism
EDTA	Ethylenediaminetetraacetic Acid
EG	Ethyleneglycol
ET	Electron Transfer
FC	Frank-Condon
MALDI-TOF	Matrix Assisted Laser Desorption Ionization - Time of Flight
NMR	Nuclear Magnetic Resonance
ODN	Oigonucleoxynucleic

PAGE	Polyacrylamide Gel Electrophoresis
PEG	Polyethyleneglycol
PET	Photoinduced Electron Transfer
PNA	Peptide Nucleic Acid
Py	Pyrenebutanol
RP-HPLC	Reverse Phase - High Performance Liquid Chromatography
Sa	trans-4,4'-Stilbene dicarboxylic Acid
Sd	bis(3-hydroxypropyl)Stilbene-4,4'-Diether
TBA	Thrombin Binding Agent
TEAA	Triethylammonium Acetate
TEM	Transmission Electronic Microscope
THF	Tetrahydrofuran
TLC	Thin Layer Chromatography

To
the time at Northwestern University

TABLE OF CONTENTS

8

Abstract.....	2
Acknowledgements.....	4
List of abbreviations.....	5
Dedication.....	7
List of Tables.....	13
List of Figures.....	15
List of Schemes.....	21

Chapter 1 Introduction

1.1 Background.....	23
1.2 Structures and properties of DNA.....	24
1.2.1 Structures of DNA.....	24
1.2.2 Electronic properties of DNA.....	33
1.2.3 Electrochemical oxidation and reduction of DNA.....	36
1.2.4 DNA damage.....	37
1.3 Electron transfer mechanisms in DNA.....	38
1.3.1 Electron transfer theory.....	38
1.3.2 Mechanism of electron transfer.....	44

Chapter 2 Mechanism studies for photoinduced charge transfer in DNA hairpin

conjugates

2.1 Background.....	50
2.2 Results	
2.2.1 Synthesis end-capped stilbene hairpin conjugates.....	61
2.2.2 Absorption and fluorescence properties of end-capped hairpins.....	63
2.2.3 Transient spectra of control molecules and hairpin conjugates.....	68
2.2.4 Transient spectra of end-capped hairpin conjugates 1-7	73
2.3 Discussion.....	82
2.3.1 Properties of linker Sa and hairpin Sa-AT	83
2.3.2 Charge separation (hole arrival) in donor-acceptor hairpins.....	86
2.3.3 Hole injection in end-capped Sa/Sd hairpin systems.....	91
2.3.4 Hole migration in A-tracts.....	92
2.3.5 Efficiency of charge separation.....	94
2.3.6 Charge recombination.....	94
2.3.7 Electron transfer mechanism in other hairpin systems.....	97
2.4 Conclusion.....	99

Chapter 3 Thermal stability studies of oligo(ethylene glycol) hairpins

3.1 Introduction.....	102
-----------------------	-----

3.2 Results	
3.2.1 Synthesis of EG -linked hairpins.....	107
3.2.2 Electronic absorption and circular dichroism spectra.....	108
3.2.3 Molecular dynamics simulations.....	111
3.3 Discussion	
3.3.1 Thermal stability of EG -linked hairpins.....	115
3.3.2 Comparison of base pairs in EG3 -hairpins and EG6 -hairpins.....	119
3.4 Conclusion.....	120

Chapter 4 Excimer studies of formation of pyrene probed parallel quadruplexes

4.1 Introduction.....	123
4.2 Results.....	129
4.2.1 Electronic spectra.....	129
4.2.2 CD spectra.....	130
4.2.3 Florescence spectra.....	135
4.2.4 Gel electrophoresis.....	139
4.3 Discussion.....	140
4.3.1 Structures of quadruplexes formed from pyrene-conjugates.....	140
4.3.2 Monomer/excimer emission studies.....	145
4.4 Conclusion.....	146

Chapter 5 Design and thermal stability studies of modified thrombin binding agents

5.1 Introduction.....	149
5.2 Results.....	153
5.2.1 Synthesis of modified thrombin binding agent.....	153
5.2.2 Electronic absorption spectra and thermal dissociation of Sd -conjugates...	153
5.2.3 CD spectra of TBA and Sd -containing conjugates HTS-1 to HTS-4	159
5.2.4 Temperature dependent CD study of TBA and Sd -containing sequences...	159
5.3 Discussion.....	165
5.3.1 Structures of Sd -modified thrombin binding agent sequences.....	165
5.3.2 Thermo stability of Sd -containing sequences.....	167
5.3.3 Proposed two-step dissociation mechanism for DNA aptamer TBA	169
5.4 Conclusion.....	171

Chapter 6 Experiment section

6.1 Materials.....	174
6.2 Instrumental.....	174
6.3 Chemical synthesis.....	179
6.3.1 Synthesis of <i>trans-N, N'</i> -bis(3-hydroxypropyl)stilbene-4,4' -dicarboxamide (Sa) linker and corresponding phosphoramidite.....	179

6.3.2 Synthesis of <i>trans</i> -bis(2-hydroxyethyl)stilbene-4,4'-diether (Sd) linker and corresponding phosphoramidite.....	183
6.3.3 Synthesis the phosphoramidite of pyrenebutanol.....	185
6.4 Solid phase phosphoramidite oligonucleotide synthesis and sample purification.....	186
6.4.1 General procedure.....	186
6.4.2 Treatment of G-rich sequences.....	189
6.5 Characterization of DNA conjugates.....	189
6.5.1 General procedure.....	189
6.5.2 3-hydroxypicolinic acid (3-HPA) matrix.....	189

References

Chapter 1.....	190
Chapter 2.....	197
Chapter 3.....	203
Chapter 4.....	205
Chapter 5.....	209
Chapter 6.....	211

LIST OF TABLES

Chapter 1

Nucleoside oxidation and reduction potentials in aprotic solvents and water.....	36
--	----

Chapter 2

2.1 Sequences of hairpin-forming oligonucleotides with Sa linkers and fluorescence quantum yields of the T6- Sa -A6 and the Sa -linked nG:C or nC:G hairpins.....	53
2.2 Fluorescence quantum yields and rate constants in Acr -DNA duplex.....	55
2.3 Rate constants for charge separation and charge recombination for Acr ⁺ /G - DNA duplex and Acr ⁺ /Z - DNA duplex.....	56
2.4 Fluorescence quantum yields and singlet decay times in Ap /G -DNA duplex.....	57
2.5 Fluorescence quantum yields and decay data.....	67
2.6 Femtosecond pump-probe transient decays.....	70
2.7 Nanosecond laser flash photolysis transient decays.....	77
2.8 Hole trapping quantum yields, hole arrival rate constants, and hole arrival times for charge transfer in hairpin 1-7	82
2.9 Summary of kinetic data for hole arrival, hole injection, and charge recombination.....	85
2.10 Free energy comparison of the charge transfer processes between different acceptor linkers and guanine.....	98

Chapter 3

- 3.1 Melting temperature (T_m) and free energies ($-\Delta G$ (37 °C)) for duplex hairpins bridged by oligo(ethylene glycol) (EG) loops and by a natural T4 loop at pH 7.0.....105
- 3.2 Melting temperatures and thermodynamics data of formation of hairpins having **EG3** and **EG6** linkers.....116

Chapter 5

- 5.1 Structure of **TBA** and designed **Sd**-containing sequences152
- 5.2 Summary of UV- T_m and CD- T_m values for **TBA** and **Sd**-containing sequences obtained from UV melting curves and CD melting curves.....157
- 5.3 The positions of CD peaks of **TBA** and **Sd**-containing sequences.....158
- 5.4 Thermodynamics formation of quadruplexes from **Sd**-containing thrombin binding sequences and **TBA** sequence by Van't Hoff analysis of UV melting curves at 295 nm.....168

LIST OF FIGURES

Chapter 1

1.1 The structure of an oligonucleotide composed of the four natural nucleobase.....	25
1.2 Base pairing in Watson-Crick A:T and G:C base pairs.....	26
1.3 Structure of a B-form DNA dodecamer.....	27
1.4 Structures of stilbene diether, Br-U, and stilbene diether linker hairpin.....	29
1.5 Top: side view of stilbene diether linked hairpin. Bottom: top view of stilbene diether linked hairpin.....	30
1.6 (Left) Structure of G-quartet formed from four guanines via Hoosteen bonding. (Right) Structure of an intramolecular G-quadruplex consisting four layered quartet.....	32
1.7 CD spectra of different quadruplex structures.....	35
1.8 Marcus-type plot of rate constant k_{ET} against driving force $-\Delta G$	44

Chapter 2

2.1 Structures of chromophore linkers in hairpin DNA conjugates.....	52
2.2 Intercalating Acr in DNA duplex.....	54
2.3 Structures of guanine G, 7-deazaguanine Z, 2-aminopurine Ap and inosine I.....	56
2.4 (a), Hole injection and hole transfer in G^+/GGG -DNA duplex;	

(b), rate constants of charge separation with distance in between donor and acceptor.....	59
2.5 (a), structures of Sa and Sd ; (b), end-capped hairpins with Sa* served as acceptor and Sd served as donor.....	61
2.6 Structures of control molecules Sa-AT , Sd-AT , and Sa-An	63
2.7a Comparison of UV absorption spectra for Sa-AT , Sd-AT , and hairpin 6	64
2.7b Comparison of the UV absorption spectra for hairpins 1-7	65
2.8 Fluorescence spectra of hairpins 1-7	66
2.9 Temporal evolution of the pump-probe spectra of Sa (a, left) and Sd (b, right) in the time range of 0.2 ns to 1.2 ns after excitation at 333nm.....	69
2.10 Temporal evolution of the pump-probe spectra of (a, left) Sa-An and (b, right) Sa-AT in the time range of -0.1 ps to 150 ps after excitation at 333 nm.....	69
2.11 Two possible pathways for singlet Sa*-An	72
2.12 Temporal evolution of the pump-probe spectra of hairpins 1 (a, left) and 2 (b, right) in the time range of -0.1 ps to 150 ps after excitation at 355 nm.....	75
2.13 Temporal evolution of the pump-probe spectra of hairpins 3 (a, left) and 4 (b, right) in the time range of - 0.1 ps to 150ps after excitation at 333 nm.....	75
2.14 Time-dependent 525/575 nm band intensity ratios for 1-7	78
2.15 Temporal evolution of the pump-probe spectra of hairpins 5 (top), 6 (middle) and 7 (bottom) in the time range of 0.1 ps to 6 ns after excitation at 355 nm.....	79

2.16 Nanosecond time-resolved spectra of 6	81
2.17 Rate constants for hole arrival in hairpins 1-7	87
2.18 Kinetics of 1	88
2.19a Simplified kinetic scheme using localized hole hopping model for 3	91
2.19b Delocalized hole hopping model for 7	91
2.20 Distance dependence of the rate constants for charge recombination.....	95
2.21 Structures, singlet energies, and reduction potentials of linker Dpa and Pa	98

Chapter 3

3.1 Structures and melting temperatures (T_m) of mini-stilbene hairpins.....	103
3.2 Structures of poly(ethylene glycol) linkers with protecting and activating groups....	104
3.3 Structures of EG3 -hairpins, and EG6 -hairpins.....	107
3.4 Normalized UV spectra of 5 M EG6 -linked hairpins.....	108
3.5 Dissociation profiles for EG3-nH (n=4-8) (top) and for EG6-nH (n=4-7) (bottom) determined at 260 nm	109
3.6 CD spectra of hairpins EG3-nH (top) and EG6-nH (bottom)	110
3.7 Minimized structures obtained from molecular dynamics simulations for EG3-6H (top two), and EG6-6H (bottom two).....	112
3.8 (a, top) Time dependent deviation in the O--HN distance for A-T base pairs BP1 (adjacent to the linker) and BP6 in hairpin EG3-6H . (b, bottom),A-T distance	

distribution for each BP in EG3-6H.	114
3.9 Time dependent deviation in the O--HN distance for A-T base pairs BP1 adjacent to the linker) and BP6 (terminal base pair) for hairpin EG6-6H	115
3.10 Hairpins with natural ACC loop.....	118

Chapter 4

4.1 Structures of guanine monomer and G-quartet formed from four guanines via Hoosteen base pairing.....	124
4.2 Polymorphism of Quadruplex structures.....	125
4.3 Illustration of monomer and excimer emission fluorescence.....	127
4.4 Designed sequences with pyrenebutanol attached at 5'-end of short poly(G) oligonucleotides.	128
4.5 Absorption spectra of the pyrenebutanol in methanol solution and the pyrenebutanol conjugate Py2 in water and in aqueous 0.1 M KCl, 10 mM potassium phosphate.....	130
4.6 Circular dichroism spectra of 1×10^{-6} M conjugates Py1-Py3 (a) in water; (b) in 0.1 M KCl, 10 mM potassium phosphate.....	131
4.7 CD spectra of Py2 in different concentrations of KCl.....	132
4.8 Temperature-dependent circular dichroism spectra of conjugates Py2 and Py3	133
4.9 CD spectra of Py4 in different salt concentrations: (a) in KCl, (b) in NaCl.....	134

4.10 Room temperature fluorescence spectra of 1×10^{-6} M conjugates Py1-Py4 in different salt conditions.....	135
4.11 The fluorescence spectra of 1×10^{-6} M conjugate Py4 in different salt conditions.....	136
4.12 Salt concentration dependence of the pyrene excimer/monomer fluorescence intensity ratio for conjugate Py2	137
4.13 Temperature dependent fluorescence spectra of conjugates Py2 and Py3	138
4.14 Excimer/monomer fluorescence intensity ratio for conjugates Py2 and Py3	139
4.15 Fluorescence spectra of 1×10^{-6} M conjugate Py4 in 0.5 M NaCl and KCl.....	144

Chapter 5

5.1 Schematic drawing of the thrombin aptamer structure.....	150
5.2 NMR structure of oligonucleotide d(G ₂ T ₂ G ₂ TGTG ₂ T ₂ G ₂)	151
5.3 UV spectra of TBA and Sd -linked oligonucleotide conjugates.....	154
5.4 Thermal dissociation profile of TBA sequence	155
5.5 Thermal dissociation profiles of Sd -containing conjugates	156
5.6 CD spectra of Sd -containing sequences and TBA sequence	158
5.7 (a, top), Temperature dependent CD dissociation of TBA . (b, bottom), CD melting profile of TBA obtained at 295 nm.	160
5.8 Temperature dependent CD spectra of HTS-1	161

5.9 Temperature dependent CD spectra of HTS-2	162
5.10 Temperature dependent CD spectra of HTS-3	163
5.11 Temperature dependent CD spectra of HTS-4	164
5.12 CD-melting profiles of of Sd -containing conjugates.....	165
5.13 Molecular modeling of HTS-3	167

LIST OF SCHEMES**Chapter 1**

- 1.1 Kinetic scheme and thermodynamics for photoinduced charge separation and charge recombination in DNA bridged donor acceptor systems.....46

Chapter 4

- 4.1 Proposed folding of conjugate **Py4** in different salt conditions.....43

Chapter 5

- 5.1 Proposed two-step dissociation mechanism of unfolding of chair type quadruplexes formed from two quartets.170

Chapter 6

- 6.1 Synthesis outline of *trans*-4,4'-stilbene dicarboxylic acid, stilbenedicarboxamide diol (Sa) and phosphoramidite.179
- 6.2 Synthesis outline of *trans*-bis(2-hydroxyethyl)stilbene-4,4'-diether (Sd), mono-DMT-Sd and DMT-Sd-phosphoramidite.....184
- 6.3 Conventional 3' DNA solid phase synthesis.....188

Chapter 1

Introduction

1.1. Background

Deoxyribonucleic acid (DNA) plays a critical role in biology in storage and transmission of genetic information in all living species,^{1, 2} and guiding protein synthesis as well.^{3, 4} Based on the similarity between the way DNA works and the operation of a theoretical device known as a Turing machine, DNA has inspired computing research.⁵ Similar to enzymes, the unique chiral nature of DNA can be transferred directly to a metal-catalyzed reaction, in the case of the copper(II)-catalyzed Diels–Alder reaction.⁶ Also the first molecular walking motor has been built from DNA,⁷ using the self assembly feature of DNA. Recently, DNA incorporated into thin film as a potential solid-state photonic device has shown high thermal stability and enhanced light emission properties.⁸ These applications of DNA are made possible by the unique structural features of DNA. As we know, B-form DNA consists of a hydrophobic core of hydrogen-bonded base pairs surrounded by a hydrophilic sugar-phosphate backbone. The base pairs form a one-dimensional π -stacked array with an average stacking distance of 3.4 Å. Construction of similar scaffolds has been attempted via synthesizing π -stacked arrays of aromatic chromophores,⁹ however to approach DNA either in length or diversity of structure is still challenging.

Based on the π - π interactions between stacked base pairs in duplex DNA, Eley and Spivey proposed that DNA could function as a one-dimensional conductor or molecular wire.¹⁰ The early 1990's work by Barton and Turro led to the proposal of ultrafast photoinduced electron transfer (PET) over long distances in duplex DNA.^{11, 12, 13} The proposal of wire-like behavior

stimulated further research on PET reactions in DNA for both experimentalists and theoreticians. A deep understanding of charge transfer in DNA is helpful to realize some particular DNA repair mechanisms, such as repair of a thymine dimer through photolyase,^{14, 15} and structure specific binding interactions between DNA and proteins.¹⁶

1.2 Structures and properties of DNA

1.2.1 Structures of DNA

The two-dimensional structure of an oligodeoxynucleotide (ODN) shown in Figure 1.1,¹⁷ is composed of four nucleic acid bases, adenine (A), thymine (T), guanine (G), and cytosine (C), which are attached on the 1' position of 2'-deoxy-ribose ring. The phosphate groups connect the 3' hydroxyl group of one deoxynucleoside to the 5' hydroxyl group of the adjacent deoxynucleoside, resulting in 5' → 3' polarity in the single ODN strand. Duplex DNA is formed by two complimentary single ODN strands based paired with each other through Watson-Crick hydrogen bonding between G:C and A:T base pairs (Figure 1.2). Duplexes can adopt different structures depending local environment and sequence features, the most common of which is B-form DNA in which the π -stacked base pairs are perpendicular to the helical axis with a stacking distance of 3.4 Å. The long axis of each base pair is rotated approximately 36° with respect to its neighboring base pairs, leading a complete helical turn every 10 base pairs. The structure of a 12-base pair B-form duplex is shown in Figure 1.3.¹⁸

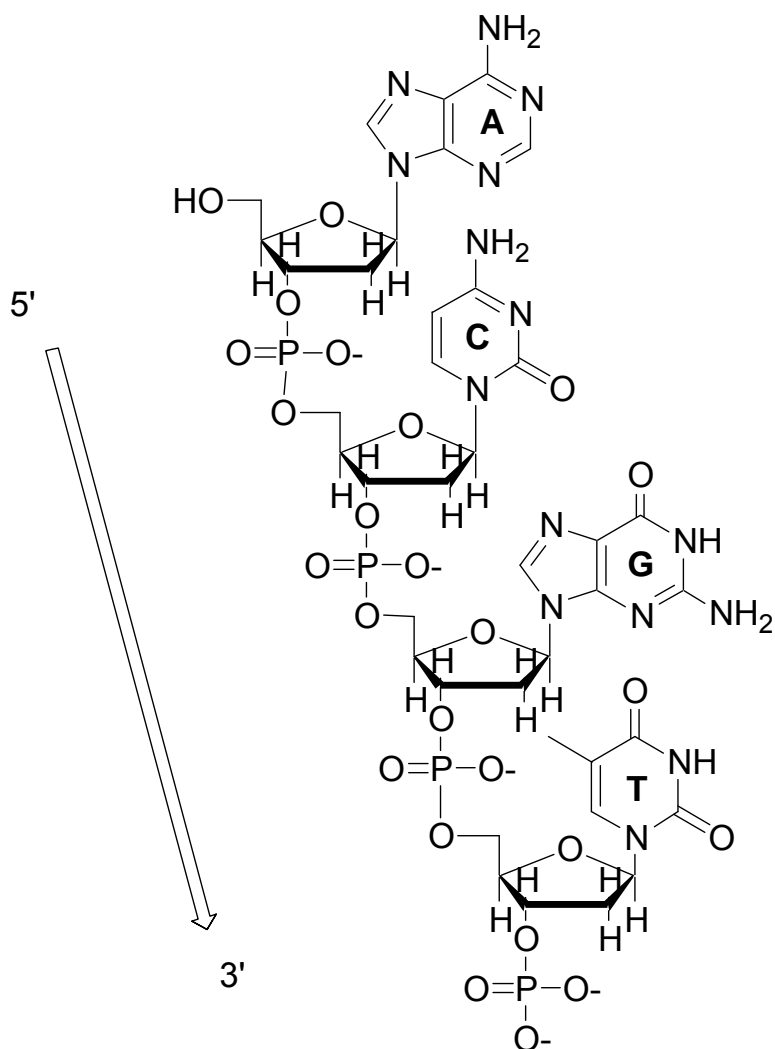
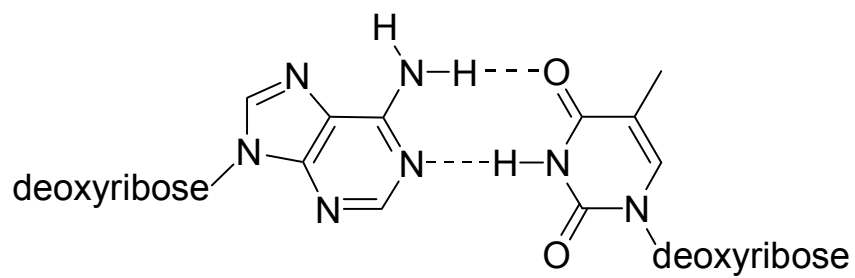
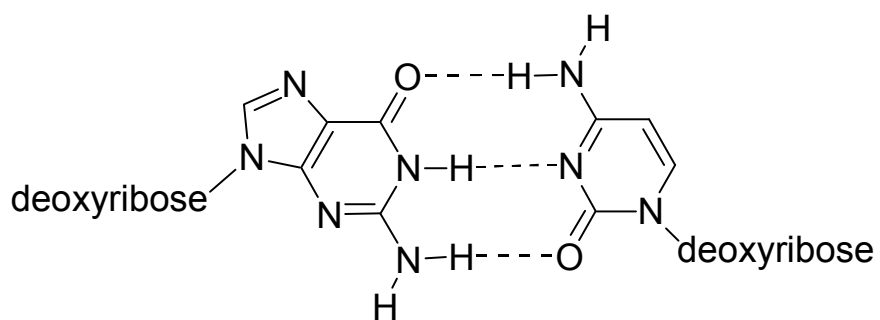


Figure 1.1 The structure of an oligonucleotide composed of the four natural nucleobases, adenine (A), cytosine (C), guanine (G), and thymine (T) with shown sequence polarity, shown by the arrow.



A:T



G:C

Figure 1.2 Base pairing in Watson-Crick A:T and G:C base pairs.

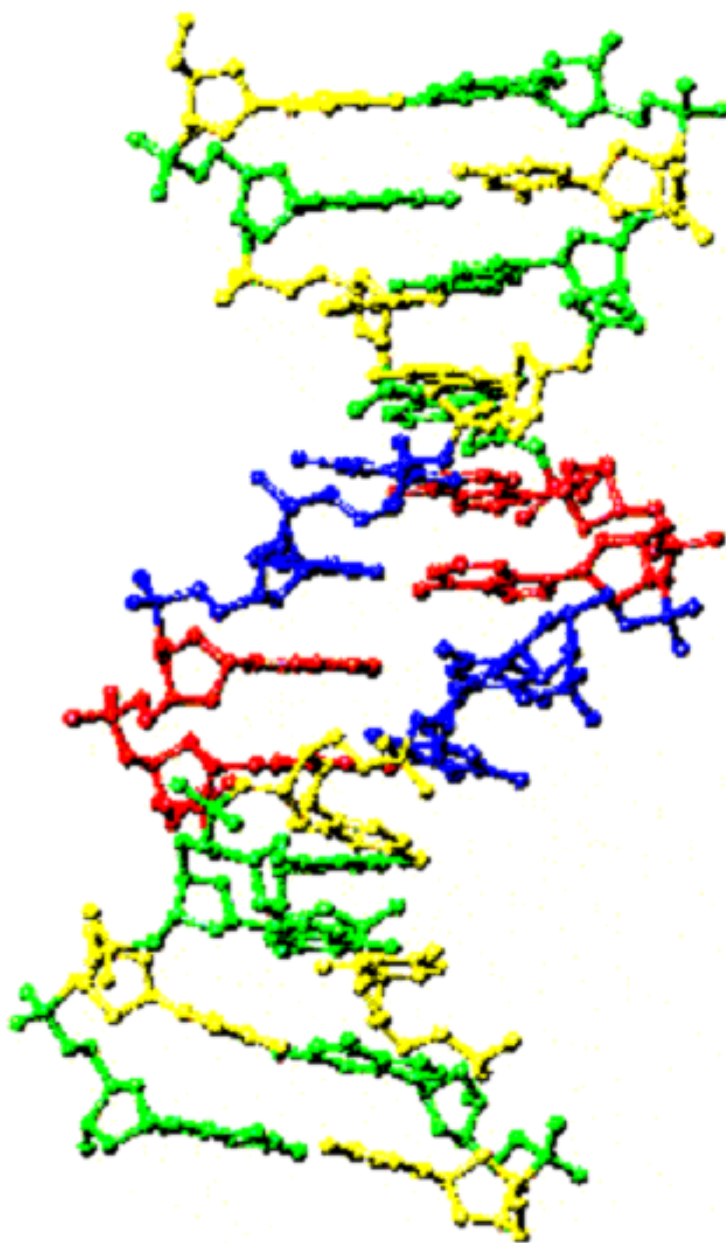


Figure 1.3 Structure of a B-form DNA dodecamer.¹⁸

Due to the presence of potentially rotatable single bonds in the backbone and the energetics of base pairing, DNA can adopt other conformations, such as A-DNA and Z-DNA. A-DNA, like B-DNA, is right handed helix, while Z-DNA is a left handed helix. Z-DNA formation is sequence dependent and mainly formed in alternating (dG-dC)_n sequences. DNA also can adopt intramolecular hairpin structures with different natural loop sequences having high stability. Organic chromophore linkers have been introduced into DNA hairpins by Lestingier and co workers.¹⁹ X-ray crystallography indicates that stilbene diether (Sd) linked hairpin (Figure 1.4) can adopt a B-form structure in which the Sd is π -stacked with the adjacent dG-dC base pair with a plane-to-plane separation of 3.25 Å and twist angles of between 10° and 20° (Figure 1.5). Both ethylenes in the Sd linker adopt gauche conformations, and the average distance between the outer Sd oxygen atoms is \approx 16.5 Å. The average inter-strand distance between phosphorus atoms bound to the Sd linker is 18.1 Å and thus comparable to the average distance of 17.7 Å for phosphorus atoms from opposite strands in B-DNA. The π -stacking interaction between the stilbene diether linker and adjacent base pair contributes the stability of this type of hairpin structure, which enables stilbene hairpins to be used in studies of even shorter base pair stems. Besides the different conformations of duplex structures, DNA also can form other secondary structures having higher stoichiometries, such as triplex and quadruplex structures. In some circumstances, DNA is in a dynamic exchange in between different secondary structures.

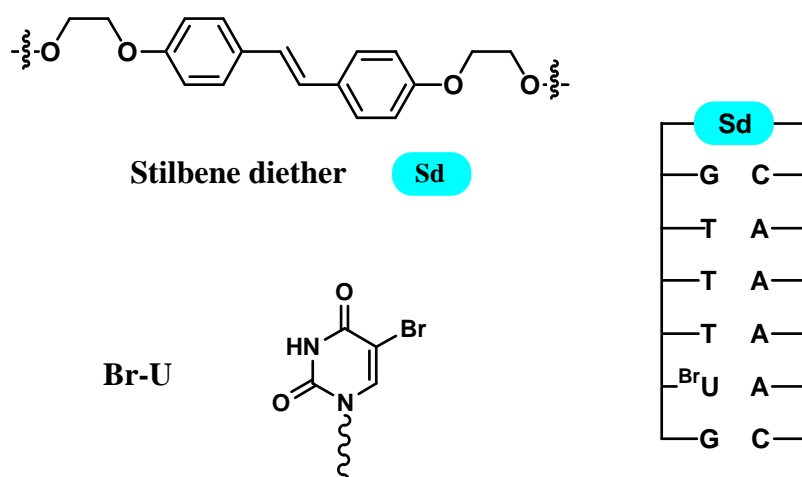


Figure 1.4 Structures of stilbene diether, Br-U, and stilbene diether linker hairpin.

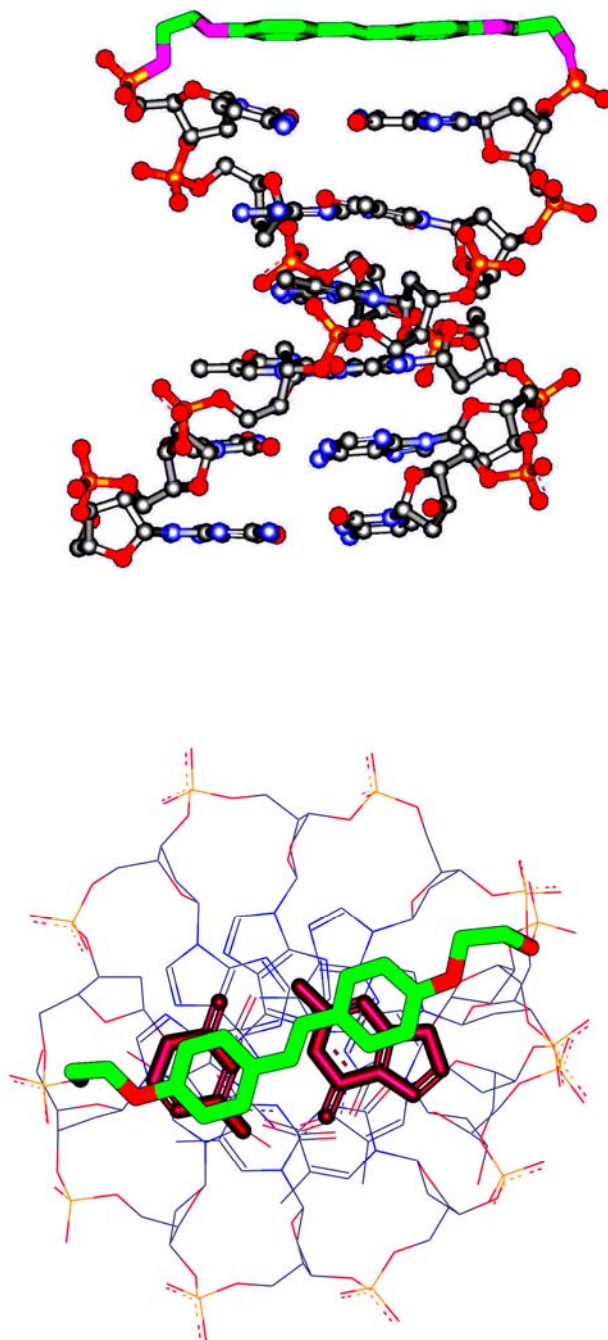


Figure 1.5 Top: side view of stilbene diether linked hairpin. Bottom: top view of stilbene diether linked hairpin.

G-quadruplex DNA is a type of structure found in guanine-rich regions at the end of chromosomes. G-quadruplex DNA has stacked arrays of G-quartets, which are structures formed by four guanines through Hoosteen base pairing (Figure 1.6).^{20, 21} The cavity in the central G-quatet can be stabilized by a cation coordinated with four carbonyl groups from the four guanines.

Guanine-rich sequences can form stable G-quadruplex in the presence of KCl when two or more continuous G-quartets are stacked into G-quadruplexes.²² Since the formation of quadruplexes shows inhibitory activity for telomerase in cancer cells, the stability and structural study of a G-quadruplexes has attracted a lot of interest. Studies have shown some alien small molecules can significantly increase the stability of G-quadruplexes via either binding or intercalating interaction, which consequently reduce the activity of telomerases.²²⁻²⁵ The interaction between these compounds and G-quadruplexes has provided a new class of highly specific therapeutic agents for cancer or other diseases.^{26, 27}

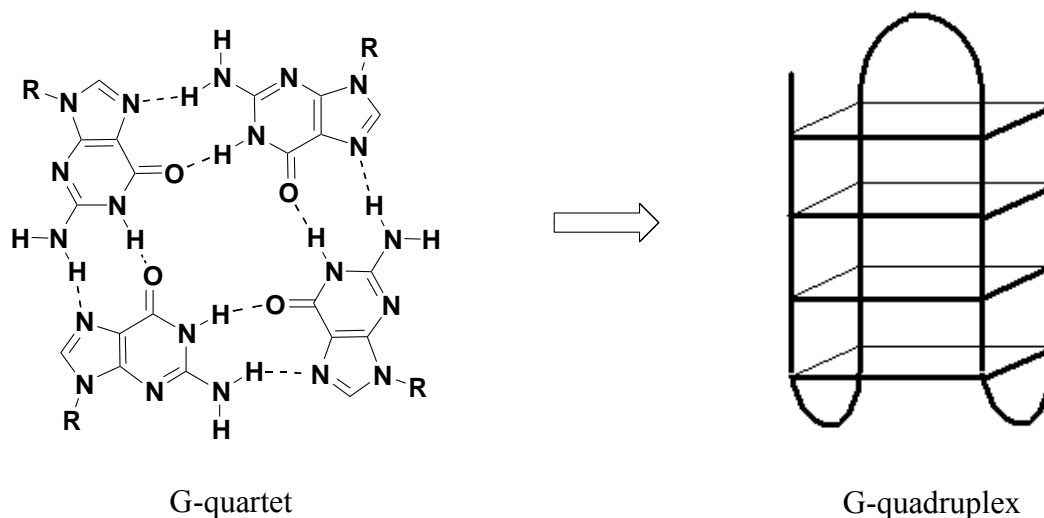


Figure 1.6 (Left) Structure of G-quartet formed from four guanines via Hoosteen bonding. (Right) Structure of an intramolecular G-quadruplex consisting four layered quartets.

The self assembly character of the G-quadruplex also fascinates scientist in different ways. Liphophilic G-quadruplexes have been synthesized as promising materials for constructing of synthetic ionic channels and pores through liposome membranes.²⁸ A variety of base-modified 8-aryl-guanine derivatives has been used in metal ion templated supramolecular chemistry.²⁹ Intramolecular formation of quadruplexes enables this type of structure to be a potent ion detector.³⁰ Modified deoxyguanosine ($dG(C_{10})_2$) containing two long alkyl chains attached on the ribose ring has shown transistor-like properties, which points out the potential application as planar solid-state biomolecular electronic devices.³¹

All of the above applications of quadruplexes are closely related to its structural

characteristics. G-quadruplexes can be associated by different means, depending on the nature of substrate sequences, such as intramolecular folding of a single sequence possessing four G-rich domains, dimerization of sequences possessing two G-rich domains, or intermolecular assemble of sequences possessing a single G-rich domain. NMR and X-ray studies of quadruplexes associated from 4 single strands have shown that all four strands are oriented in the same direction and adopt the same anti glycosidic conformation.^{32, 33} There are four identical grooves in the parallel G-quadruplex and they are about the same size as the minor groove of B-DNA.^{32, 34, 35} For the antiparallel quadruplexes formed from hairpin dimmers or intramolecular folding, the four grooves are not identical.³⁶⁻³⁸ NMR-based solution structures of intramolecular G-quadruplexes show either a diagonal-loop type or an edge-loop³⁵ type central loop,³⁹ and two edge-loop regions. The X-ray structure of the intramolecular G-quadruplex, however, shows three edge-loop regions.⁴⁰ The loop regions of G-quadruplexes potentially have the most topological variation.

1.2.2 Electronic properties of DNA

The individual nucleobases, nucleosides, and nucleotides all have broad absorption bands with maxima near 260 nm, resulting from overlapping $n-\pi^*$, and $\pi-\pi^*$ transitions.¹ Stacking of nucleobases in B-form duplex DNA results in a 20-25% decrease in the 260 nm absorption compared to that of the single strand DNA, an affect known as hypochromism. The observation of hypochromism can provide evidence for duplex formation during hybridization of

complementary strands.

Natural nucleobases, nucleosides, and nucleotides are weakly fluorescent. Singlet lifetimes are less than 1 ps in aqueous solution, with fluorescent quantum yields $< 5 \times 10^{-4}$.⁴¹⁻⁴⁵ Duplex DNA shows even weaker fluorescence.⁴⁶ Intersystem crossing quantum yields for nucleobases, nucleosides, and nucleotides are also low ($< 10^{-2}$),⁴⁷ therefore, the singlet states decay predominantly by non-radiative processes with a rate constants of approximately 10^{13} s^{-1} in gas phase,⁴⁸ and 10^{12} s^{-1} in solution.⁴¹ Short singlet lifetimes and low intersystem crossing quantum yields indicate the difficulty of using nucleobases as excited state donors or acceptors in studying photoinduced electron transfer (PET).

Due to the chiral nature of DNA, different types of DNA also show characteristic circular dichroism (CD) spectra. With different local helical environment, the excitonic coupling between stacked and paired bases results in different absorption of left vs. right-handed circular polarized light. The value of the difference of $(\epsilon_L - \epsilon_R)$ is related to the distance between the transition dipoles of the stacked base pairs.⁴⁰ The CD spectra of duplex B-DNA and hairpin B-DNA have been intensely studied. Recently studies of exciton coupled – CD (EC-CD) of stilbene end-capped hairpins provide a new tool using DNA as a helical ruler to investigate both the distance and angular dependence of the interactions between chromophores separated by a base-pair domain.⁴⁹ The CD spectra for quadruplexes are shown in spectra Figure 1.7. The CD spectra of quadruplexes are dependent upon sequences which construct quadruplexes and salt conditions.

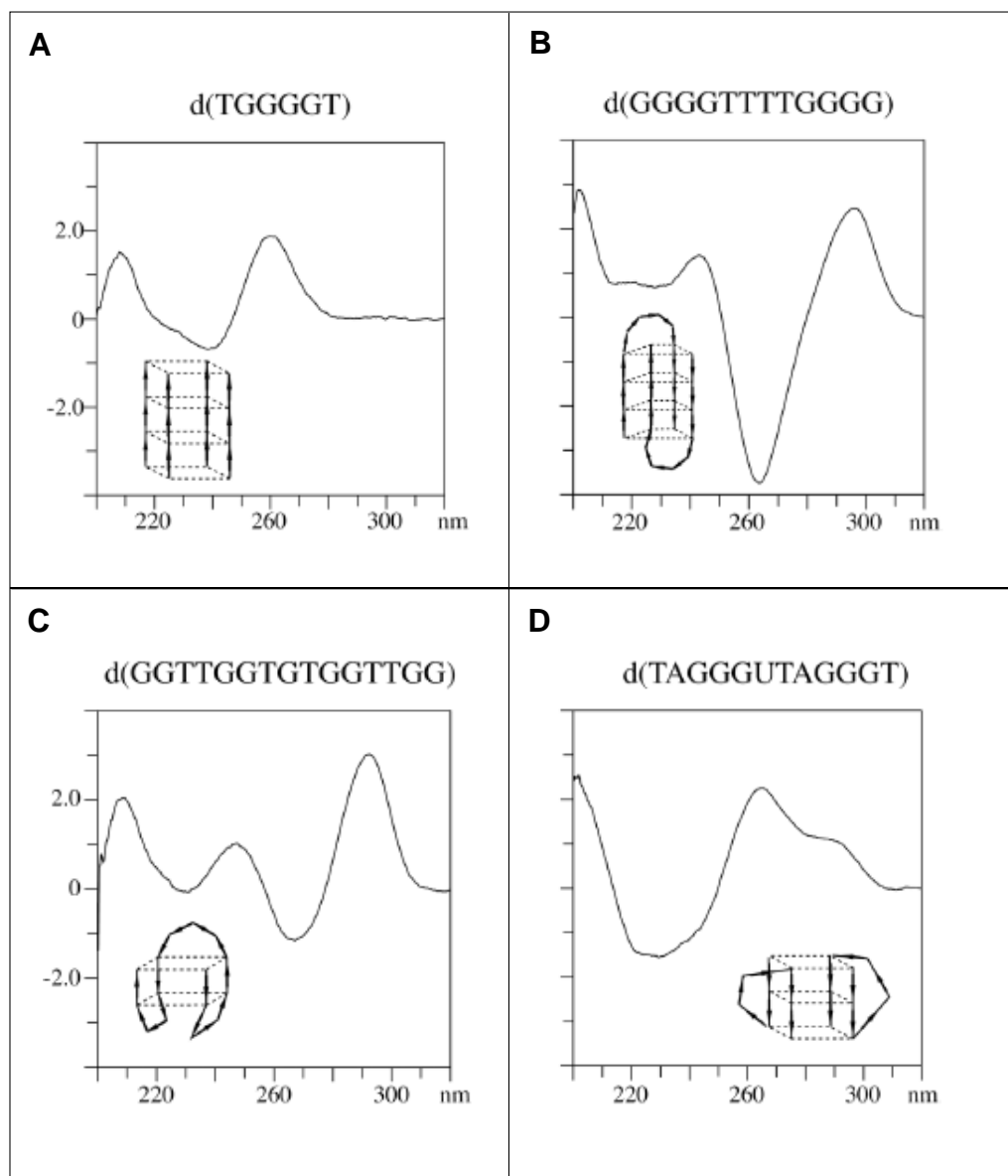


Figure 1.7 CD spectra of different quadruplex structures. A, parallel intermolecular quadruplex structure formed from d(TGGGGT).⁵⁰ B, symmetric basket type anti-parallel hairpin dimer structure formed by d(GGGGTTTTGGGG).^{36,37} C, chair type anti-parallel structure formed by the thrombin binding aptamer d(GGTTGGTGTGGTTGG).^{39,51} D, external loop type structure formed by a dimer of d(TAGGGUTAGGGT).^{52,53}

1.2.3 Electrochemical oxidation and reduction of DNA

Redox potential of the nucleosides in polar aprotic solvent has been measured by Seidel et al. by means of cyclic voltammetry⁵⁴ and the redox potentials in aqueous solution has been determined by Steenken and coworkers by means of pulse radiolysis equilibrium analysis using time-resolved spectrophotometric detection.⁵⁵ (Table 1.1)

Table 1.1 Nucleoside oxidation and reduction potentials in aprotic solvents and water

Base	$E_{\text{ox}}, \text{CH}_3\text{CN}^{\text{a}}$	$E_{\text{ox}}, \text{H}_2\text{O}^{\text{c}}$	$E_{\text{rdn}}, \text{DMSO}^{\text{b}}$	$E_{\text{rdn}}, \text{H}_2\text{O}^{\text{c}}$
Guanine, G	1.49	1.29	< -2.76	
Adenine, A	1.96	1.42	-2.52	
Cytosine, C	2.14	~ 1.6	-2.35	-1.09
Thymine, T	2.11	~ 1.6	-2.18	-1.10
Uracil, U	≥ 2.39	~ 1.6	-2.07	-1.10
7-Deazaguanine, Z		0.95		
Inosine		0.95		

^a All values in V versus SCE.⁵⁴ ^b Data in dimethylformamide (DMSO).⁵⁴ ^c Data obtained at pH 7.0.⁵⁵

The lower oxidation potential (E_{ox}) of guanine is consistent of the observation of selective oxidative cleavage at guanine containing sites. Specifically, guanine located at 5' next to a purine, especially guanine, is more likely to be oxidized than guanine located 5' to a pyrimidine, when stacked in a regular B-form duplex. This was further illustrated experimentally by Saito et al.,⁵⁶ and calculations by this group showed that the trend in ionization potentials is $5'-GGG-3' < 5'-GG-3' < 5'-GA-3' < 5'-GT-3' \sim 5'-GC-3' < G$.⁵⁷ Hickerson et al.⁵⁸ have reported that oxidative cleavage of an 18-mer duplex containing one isolated G, one GG, and one GGG sequence has a ratio of 1.0: 3.7: 5.3. Selective cleavage at GG and GGG sites has been assigned to hole localization at these sites as a consequence of their lower ionization potentials.

1.2.4 DNA damage

DNA damage can occur during the cycle of cell reproduction by spontaneous and inherited gene mutations, or be stimulated by the production of reactive oxygen species in natural cellular processes. DNA damage can also be caused by other external sources, such as ionizing radiation, UV light, or toxic chemicals.

Radiolysis of aqueous solutions results in the ionization of water to generate the hydrated electron, e_{aq}^- , and $H_2O^+ \cdot$.⁵⁹ The former species can cause the ionization any of four nucleobases.⁶⁰

⁶¹ And $H_2O^+ \cdot$ can transfer a proton to water, resulting in the formation of H_3O^+ and $HO \cdot$.

Abstraction of hydrogen atoms from DNA by $HO \cdot$ results in the majority of the strand cleavage events under radiolysis.

The chemical oxidant *tert*-butyl hydroperoxide (BHP) can generate free radicals and cause DNA strand breaks and various types of base damage. Electrophilic 4-nitroquinoline-1-oxide (4-NQO) forms DNA adducts and causes a wide range of DNA lesions including single-strand breaks, and the formation of pyrimidine-dimers, abasic sites, and oxidized bases. Studies using quantitative PCR methods have shown that under treatment of 4-NQO or BHP, the displacement loop (D-loop), especially in a polycytidine stretch (C-tract) is highly susceptible to mutations because of its vulnerability to DNA damage and inefficient repair mechanisms causing many of the somatic mtDNA mutations in human cancers.⁶²

However, studies using ionizing irradiation and chemical oxidants methods do not provide dynamic information concerning electron transfer. Thus photoinduced electron transfer has been utilized to study the electron transfer processes in DNA. Photoinduced electron transfer also offers site-specificity by means of selectively exciting incorporated photosensitizers. Shafirovich et al.⁶³ have employed two-photon excitation of the nucleobase 2-aminopurine (AP) to site-selectively generate cation radicals in both single-strand and duplex DNA.

1.3 Electron transfer mechanisms in DNA

1.3.1 Electron transfer theory

Electron transfer (ET) is a process in which an electron moves from one molecular entity to another, or between two localized sites in the same molecular entity.⁶⁴ In ET the formal oxidation states of both reaction partners change. Electron transfer processes occurs extensively

in nature, in processes including oxygen binding and transport,⁶⁵ photosynthesis and respiration,⁶⁶ metabolic syntheses,⁶⁷ and detoxification of reactive species.⁶⁸ Therefore studying electron transfer process is essential to understanding these biological processes.

Photoinduced electron transfer is a process in which an electron is transferred from an electron donor species (D) to an electron acceptor species (A). The process is accomplished by two steps. In the first step either the electron acceptor or electron donor species is photoexcited. This results in one electron from the highest occupied orbital (HOMO) being promoted into the lowest unoccupied molecular orbital (LUMO). This electronic transition creates vacancies in low-lying bonding, or non-bonding orbitals, called “holes”, which serve as much better electron acceptors than unoccupied orbitals of higher energy. In the case of excited electron donors, the single electron on LUMO is transferred to electron acceptors nearby. For photoinduced electron transfer between an excited donor molecule (D*) and a ground-state acceptor molecule, or between an excited acceptor molecule (A*) and a ground-state donor molecule, with an infinite separation, the free-energy change can be estimated as equation [1] and [2] respectively.

$$\Delta G(\infty) = -E_{00}(D) + e(E_{\text{ox}}(D) - E_{\text{red}}(A)) \quad [1]$$

$$\Delta G(\infty) = -E_{00}(A) + e(E_{\text{ox}}(D) - E_{\text{red}}(A)) \quad [2]$$

$E_{00}(D)$ and $E_{00}(A)$ are the energy of the zero-zero transition to the lowest excited singlet state of

donor D and that of acceptor A. $E_{\text{ox}}(\text{D})$ and $E_{\text{red}}(\text{A})$ are respectively the first one-electron oxidation potential for donor (D) and the first one-electron reduction potential of acceptor (A) in the solvent under consideration, and e denotes the elementary charge. When donor and acceptor are separated by a certain distance, the Coulombic attraction energy between the radical ion pair during electron transfer process needs to be considered and can be predicted according to a point-charge model as $-e^2/(\epsilon R_c)$. R_c is the center-to-center distance of the ions and ϵ is the dielectric constant of the medium. According to the Born equation, the solvation free-energy of an ion pair is described by equation [3],

$$\Delta G_{\text{solv}} = - (e^2/2) [(1/r_d^+) + (1/r_a^-)] (1-1/\epsilon) \quad [3]$$

where r_d^+ and r_a^- are effective radii of the cation and anion radicals. With overall consideration of Coulombic attraction and solvation effect, equation [4] known as Rehm-Weller equation can be used for calculation of the free-energy change upon photoinduced electron transfer between donor D and acceptor A in a medium with dielectric constant ϵ at a distance R_c .

$$\Delta G_{\text{et}} = e[E_{\text{ox}}(\text{D}) - E_{\text{red}}(\text{A})] - E_{00}(\text{D}) - e^2/(\epsilon R_c) - (e^2/2) [(1/r_d^+) + (1/r_a^-)] (1-1/\epsilon) \quad [4]$$

The effective radii r_d^+ and r_a^- can be obtained through modeling. For aromatic ions, they can be calculated from the molar volume of the neutral molecule if they are treated as spheres. ΔG_{solv} is

small (ca. -0.1 V) in water and polar organic solvents.⁶⁹

According to basic Marcus theory for an outer-sphere electron transfer process in which the free enthalpy of activation can be described in Equation [5],

$$\Delta G^\ddagger = \frac{(\lambda + \Delta G)^2}{4\lambda} \quad [5]$$

where λ is the reorganization energy, and it includes to two parts, λ_i and λ_s . The former is the nuclear reorganization energy, arising from nuclear structural differences between the equilibrium configurations of the reactant and product states, which are due to changes in bond lengths and bond angles of the reactants during electron transfer. It can be estimated using the charge transfer absorption maximum and the charge transfer emission maximum in a non-polar solvent (where $\lambda_s = 0$) of the electron donor-acceptor system studied. The energy difference between these two maxima equals $2\lambda_i$. The latter λ_s is the solvent reorganization energy, which arises from the orientation change of solvent due to the dipole change from reactants to products in electron transfer process. It represents the energy needed to reorient the solvent molecules around the newly formed product.

For a system in which D and A are spatially separated, i.e., the electronic coupling between D and A is weak, the rate constant for electron transfer process from D to A can be calculated from Femi golden rule, equation [6],

$$k_{\text{ET}} = \frac{2\pi}{\hbar} |H_{\text{DA}}|^2 (FC) \quad [6]$$

where H_{DA} is the effective electronic coupling Hamiltonian matrix element resulting from the extent of electronic interaction between D and A. FC is the Frank-Condon weighted density of states. FC reflects the influence from all nuclear modes of the system, often represented in terms of effective coordinates.⁷⁰

At high temperature, since all nuclear vibrational frequencies ω obey the relation $\hbar\omega_i \ll k_B T$, i.e. the nuclear tunneling effects are completely neglected, the FC takes on a limiting classical form [7].

$$(FC)_{\text{classical}} = (4\pi\lambda k_B T)^{-1/2} \exp\left[-\frac{(-\Delta G - \lambda)^2}{4\lambda k_B T}\right] \quad [7]$$

But at lower temperature, where quantum effects are unavoidable for the high-frequency modes ($\hbar\omega_i \gg k_B T$), a semiclassical approach is used to describe FC , with high frequency modes treated quantum mechanically and low frequency modes still treated classically. After considering two electronic states interacting with a large number of vibrational levels in the Hamiltonian matrix element, FC is given by equation [8], where $S = \lambda_i / \hbar\omega$

$$(FC) = (4\pi\lambda k_B T)^{-1/2} \exp(-S) \sum_{n=0}^{\infty} \frac{S^n}{n!} \exp\left[-\frac{(-\Delta G + n\hbar\omega + \lambda_s)^2}{4\lambda_s k_B T}\right] \quad [8]$$

Here λ_s , the solvent reorganization energy, is treated classically. λ_i is the nuclear reorganization energy.

Since photoinduced electron transfer requires the assumption that the initial excited state is vibrationally relaxed, i.e. $\hbar\omega_i \gg k_B T$, the rate of electron transfer can be analyzed within the framework of semi-classical equation [9], which is called the Marcus-Levich-Jortner equation,

$$k_{\text{ET}} = \frac{2\pi}{\hbar} |H_{\text{DA}}|^2 (4\pi\lambda k_B T)^{-1/2} \sum_{n=0}^{\infty} \frac{e^{-S} S^n}{n!} \exp\left[-\frac{(\Delta G + n\hbar\omega + \lambda_s)^2}{4\lambda_s k_B T} \right] \quad [9]$$

where the electronic coupling matrix element $H_{\text{DA}} = H_{\text{DA}}^0 \exp[-(\beta/2) R]$, and β is the exponential parameter.

According to both classic and quantum mechanical Marcus theory, a plot of the rate constant k_{ET} against ΔG , is a bell shape, as shown in Figure 1.8. There are three regions in figure, 1) a normal region for endergonic reactions (where, $-\Delta G < \lambda$), in which k_{ET} increases with increasing driving force; 2) an activationless point where $-\Delta G = \lambda$; and 3) an inverted region for exoergonic reactions (where $-\Delta G > \lambda$), in which k_{ET} decreases with increasing driving force.

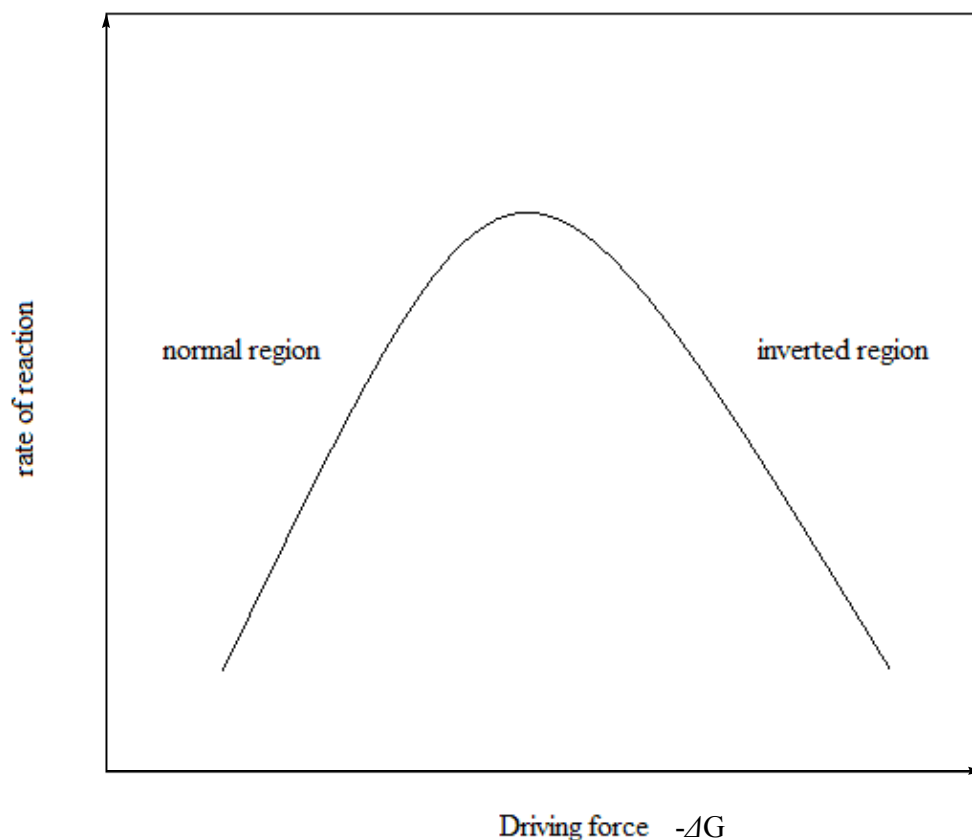


Figure 1.8 Marcus-type plot of rate constant k_{ET} against driving force $-\Delta G$.

1.3.2 Mechanisms of electron transfer

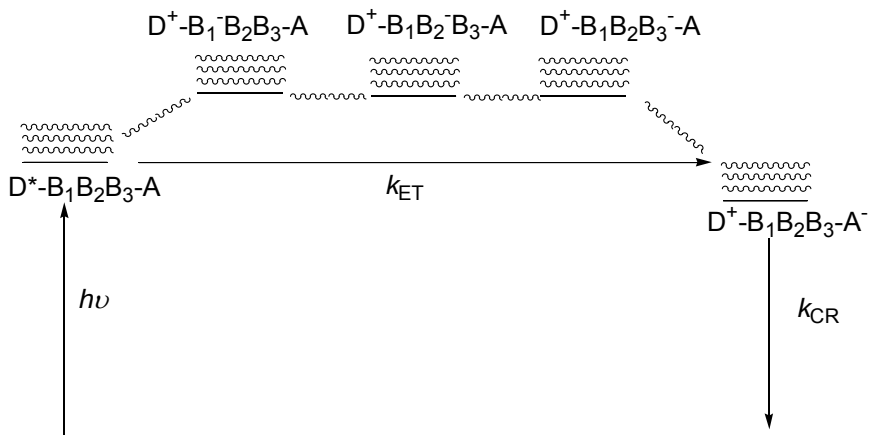
When the bridge states of a bridged donor acceptor system lie well above the initial A^*-B-D and final $A^{\cdot-}-B-D^{\cdot+}$ states, it is assumed that the energetics for bridge-mediated electron transfer are independent of distance, thus in Marcus-Levich-Jortner equation [9] the only distance-dependent term is H_{DA} . Since $H_{DA} = H_{DA}^0 \exp [-(\beta/2) R]$, the rate constant of electron transfer of bridge-mediated donor acceptor system can be described by Equation [10].

$$k_{\text{ET}} = k_0 e^{-\beta R} \quad [10]$$

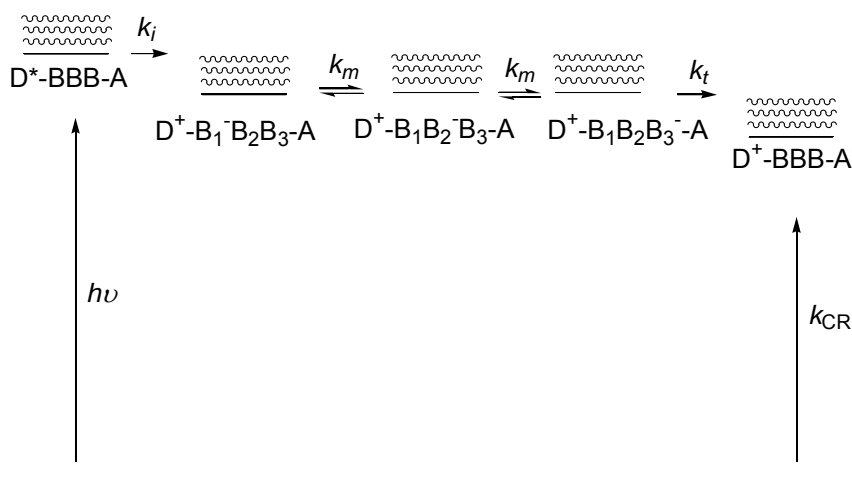
k_0 is mainly dependent on Franck-Condon factors for electron transfer process and R is the distance between donor and acceptor. The exponential parameter β is dependent upon the energy gap between the initial and bridge states, and the electronic coupling matrix element between D and A . Equation [9] predicts that the rate constant for a bridge-mediated donor acceptor system is strongly distance dependent.

Two distinct mechanisms for charge transfer in DNA have been described by Jortner and et al.⁷¹ One is the two-center unistep superexchange mediated charge transfer, which follows Marcus-Levich-Jortner equation. The other is multistep charge transport via some bases of the DNA backbone, which has been explored in molecular crystals⁷² and polymers.^{73, 74} The mechanisms are shown in Scheme 1.1.

A



B



Scheme 1.1 Kinetic scheme and thermodynamics for photoinduced charge separation and charge recombination in DNA bridged donor acceptor systems. (A) Uni-step charge transfer via superexchange. (B) Multistep charge transport via hopping, which includes hole injection, hole migration and hole trapping. k_{ET} is the rate constant of electron transfer, k_{CR} is the rate constant of charge recombination process, k_i is the hole injection rate constant from excited state to adjacent base, k_m is the hole migration rate constant along nucleobases, and k_t is the hole trapping rate constant from bridged nucleobase to electron acceptor.

As shown in the Scheme 1.1A, when the energy gap between singlet excited state and bridge states $\Delta E \gg 0$, charge transfer will occur as a superexchange process. When the energy gap between singlet excited state and bridge states $\Delta E \ll 0$, a multi-step charge transport mechanism (also called hopping mechanism) is preferred. The hopping mechanism involves three steps), charge injection from singlet excited state to most adjacent nucleobase B_1 , charge hopping between bridge nucleobases B_1, B_2, \dots , and charge trapping at the acceptor site.

Jortner and coworkers^{71, 75} have proposed that hole transport could be treated as a series of hops between guanines, with each hop treated as a superexchange process. The efficiency (Φ) of charge transfer is dependent upon the number of hops N as shown in equation [11],

$$\Phi \propto \exp [-N (k_d / k_{\text{hop}})^{1/2}] \quad [11]$$

where k_{hop} is the hopping rate constant for each hopping step, and k_d is the rate constant for chemical reaction of the guanine cation radicals which competes with hopping. This equation can be written as equation [12],

$$\Phi \propto \exp (-\beta' R) \quad [12]$$

where β' is a characteristic of the system, and R is the donor-acceptor distance. However since the hole hopping process is taking place over long distances, static and dynamic disorder caused

by the solvent and counter ions might have more important effects than that in short distance electron transfer process.⁷¹ The charge transfer rate of hopping mechanism can be expressed in equation [13].

$$k_{\text{ET}} = k_0 \times N^{-\eta} \quad [13]$$

where η lies between 1-2 and represents the influence of the medium. Electron transfer studies between intercalated ethidium and diazpyrenium dichloride in calf-thymus DNA ($\beta = 0.88 \text{ \AA}^{-1}$),⁷⁶ stilbene and guanine in hairpin DNA ($\beta = 0.64 \text{ \AA}^{-1}$),⁷⁷ and intercalated acridine and guanine in DNA duplex ($\beta = 1.42 \text{ \AA}^{-1}$)⁷⁸ show strong distance-dependent characters of electron transfer in DNA. However, pulse radiolysis investigations and the studies of photoinduced strand cleavage indicate that charges can migrate over distances longer than several bases.^{79, 80} A similar charge migration independence is observed in the studies of thymine dimer repair via charge transfer from an oxidation of GG located at a remote site ($R=19-16\text{\AA}$).⁸¹⁻⁸³ Analyzing these observations based on Marcus theory, low distance-dependent β values have been obtained leading to the proposal of molecular wire behavior of DNA. In the late 1990s, based on strand cleavage studies, Breslin et al.^{79, 80} suggested that electron transfer over long distance in DNA might occur by an alternative hole hopping mechanism, which explains the experimental observations of low β values in earlier studies.

Chapter 2

Mechanism studies for photoinduced charge transfer in DNA hairpin conjugates

2.1 Background

There are two types of charge transfer in DNA: 1) positive charge or electron hole transfer when a radical cation moves from one base pair to another and, 2) excess electron transfer when a radical anion migrates through the π stack. Extended experimental and theoretical studies of charge transfer in DNA have been related to hole migration, i.e. to the propagation of cation states of nucleobases along the duplex.¹

The initial electron transfer studies employed metal complexes: 1) DNA duplex with two non-covalent bound metallointercalators, and 2) DNA duplexes with charge donor or acceptor covalently attached at the ends of duplexes. The early studies of Barton and Turro are complicated by uncertainty in the location of the metallointercalators that served as electron donor or acceptor.^{2,3} Intercalating two dyes (e.g. donor and acceptor) into DNA duplex requires at least two intervening base pairs, and causes local disruption of the DNA structure.⁴⁻⁶ The electron transfer mechanism is distance-dependent. Studies of structurally defined oligonucleotide conjugates with ruthenium complexes covalently attached at the two opposite ends of a duplex⁷ have shown that when there are eight base pairs in between donor and acceptor, the rate constant of electron transfer is similar to that for a protein bridge of comparable length. However, the π -stacking interaction between the terminal metal complex and neighboring nucleobase remains poor understood.

In the mid-1990s, several systems processing well defined geometries were introduced to study superexchange ET in DNA. The distance dependence of electron transfer in these systems

can be investigated by systematically varying the number of base pairs separating donor and acceptor.

Lewis and coworkers have employed hairpin-forming bis(oligonucleotide) conjugates in which an organic chromophore (structures shown in Figure 2.1) serves both as a hairpin linker connecting two complementary oligonucleotide arms and as an electron acceptor.⁸⁻¹² The crystal structure of a stilbenediether-linked hairpin with six base pairs adopts a B-form DNA conformation, in which the stilbene linker is π -stacked with the adjacent G:C base pair.¹³

For a family of hairpins containing a single G:C base pair at different positions relative to stilbenediamide linker (**Sa**), the fluorescence intensity increases as the G:C base pair moves farther away from the **Sa** linker^{8, 11, 14} (Table 2.1). Similar quenching of the fluorescence intensity and similar fluorescence decay times were observed for sequences with G either in the polyA arm or the polyT arm. Rate constants for charge separation and charge recombination were obtained from analysis of the femtosecond transients assigned to the decay of **Sa*** and **Sa**⁻. Analysis of the kinetic data for **Sa**/G hairpins using a superexchange model provides a distance dependence of $\beta = 0.65 \text{ \AA}^{-1}$ for charge separation and $\beta = 0.95 \text{ \AA}^{-1}$ for charge recombination.⁸

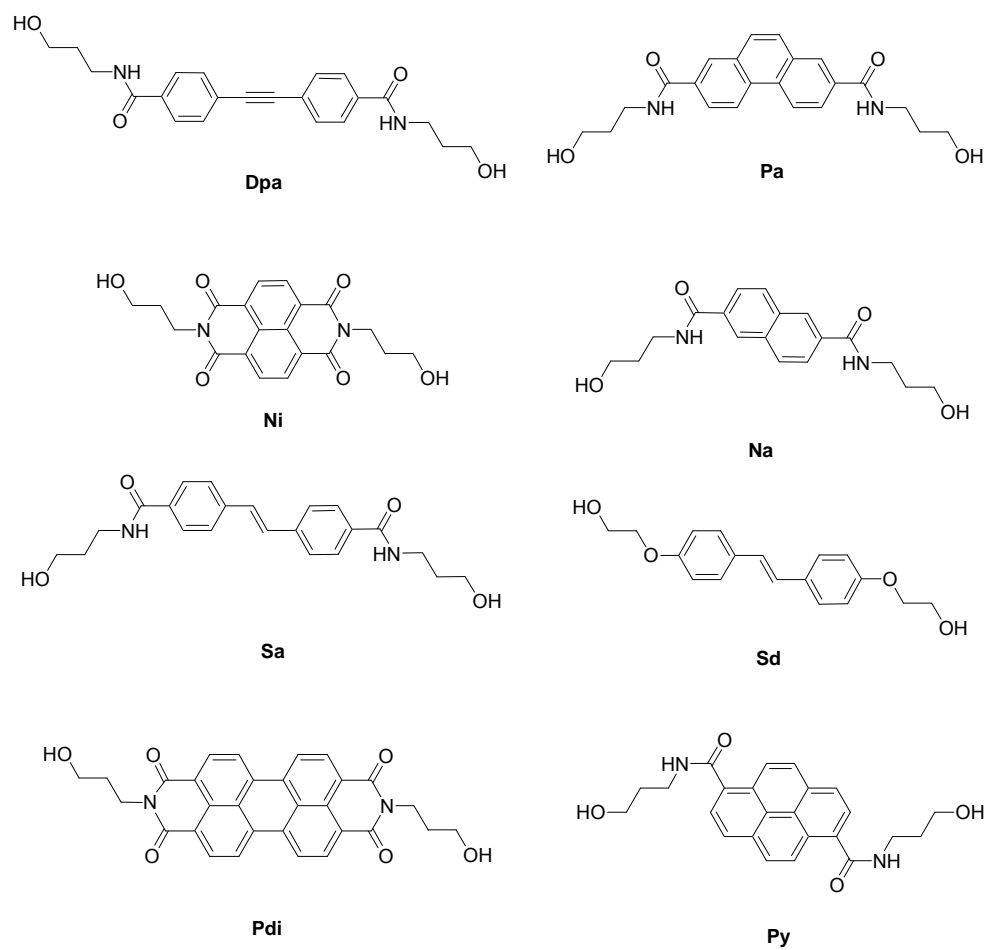


Figure 2.1 Structures of chromophore linkers in hairpin DNA conjugates.

Table 2.1 Sequences of hairpin-forming oligonucleotides with **Sa** linkers and fluorescence quantum yields of the T6-**Sa**-A6 and the **Sa**-linked nG:C or nC:G hairpins.¹¹

Name	Sequence	Φ_f
T6- Sa -A6	5'-TTTTTT- Sa -AAAAAA-3'	0.38 ^a
1G:C	5'-TTTTTG- Sa -CAAAAA-3'	< 0.01 ^a
2G:C	5'-TTTTGT- Sa -ACAAAA-3'	0.040 ^a
3G:C	5'-TTTGTT- Sa -AACAAA-3'	0.14 ^a
4G:C	5'-TTGTTT- Sa -AAACAA-3'	0.26 ^a
5G:C	5'-TGTTTT- Sa -AAAACA-3'	0.35 ^a
2C:G	5'-TTTTCT- Sa -AGAAAA-3'	0.018 ^b
3C:G	5'-TTTCTT- Sa -AAGAAA-3'	0.050 ^b
4C:G	5'-TTCTTT- Sa -AAAGAA-3'	0.20 ^b
5C:G	5'-TCTTTT- Sa -AAAAGA-3'	0.35 ^b

^a Data from ref⁸. ^b Data from ref¹¹.

By means of synthetically incorporating 9-amino-6-chloro-2-methoxyacridine (**Acr**) at a defined internucleotide site of a duplex DNA (Figure 2.2), distance controlled electron transfer between **Acr** and guanine has been studied by Tanaka et. al.¹⁵ The decay in fluorescence

intensity of **Acr** in polyA:polyT duplex is monoexponential with a life time of 22.8 ns.

Introducing neighboring G into the strand dramatically decreases the fluorescent quantum yield of **Acr**. The presence of intervening A:T base pairs between Acr and the G:C base pair results in a pronounced change in fluorescent quantum yield and lifetime (Table 2.2). Assuming electron transfer occurs through the π -stack between **Acr** and guanine, instead of through bonds,

$$k_{\text{et}} = \frac{1}{\tau_0} \left(\frac{\Phi_0}{\Phi} - 1 \right)$$

the rate of intramolecular electron transfer can be evaluated with equation

The β value of this system is 1.42 \AA^{-1} , which indicates a strong distance dependence of the PET process.

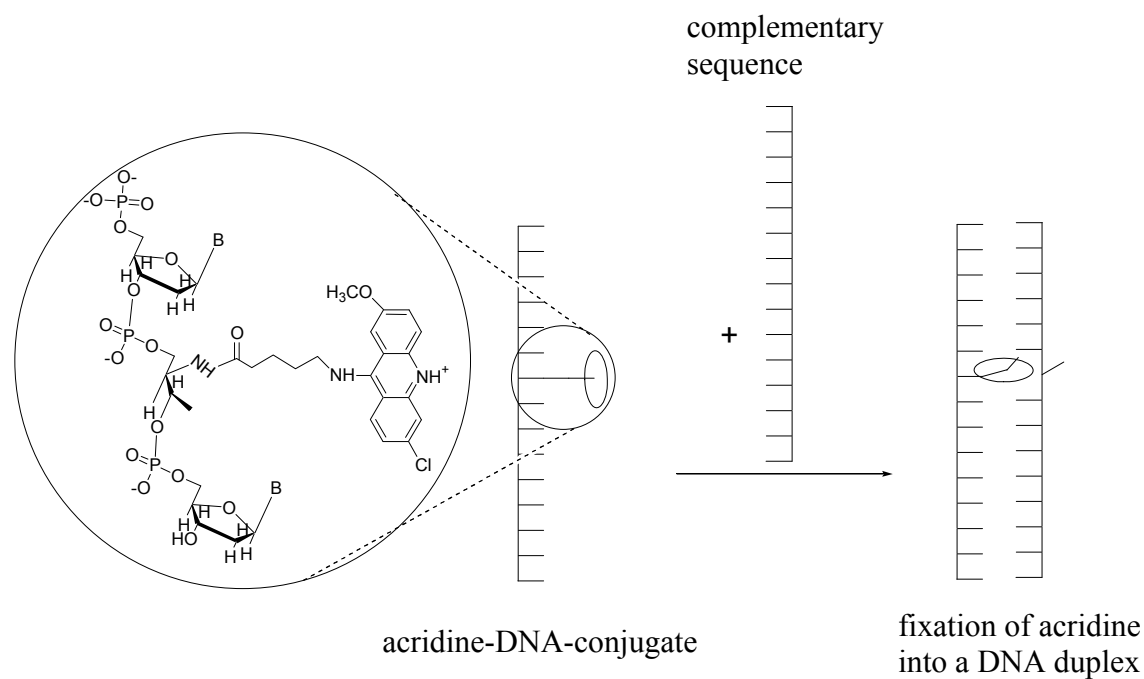


Figure 2.2 Intercalating **Acr** in DNA duplex.¹⁵

Table 2.2 Fluorescence quantum yields and rate constants in **Acr**-DNA duplex.

Sequence	A-D distance, Å	Φ_f	τ_s , ps	k_{cs}
5' [Acr]AA	-	0.655	22.8 x 10 ³	
5' [Acr] GA	3.4	0.015	66	9.5 × 10 ⁹
5' [Acr]AG	6.8	0.307	155	5.0 × 10 ⁷
5' [Acr]AAG	10.2	0.647		3.4 × 10 ⁵

Data from ref. 15.

Using femtosecond to nanosecond time-resolved pump-probe spectroscopy, charge transfer in Acr-G system¹⁵ has been reinvestigated by Michel-Beyerle and coworkers.^{16, 17} In the case of guanine as nearest neighbor, the intermediate radical **Acr**[•] is formed within 4 ps and decays on the 30 ps time scale. With one A:T intervening base pair between **Acr**⁺ and guanine, charge separation rate slows down by 3 order of magnitude, which results in an apparent β value of $> 2.0 \text{ \AA}^{-1}$. However, this apparent distance dependent ET process maybe a consequence of relaxation of singlet **Acr**⁺, which is much quicker than the electron transfer when **Acr**⁺ and G are separated by one A:T base pair. Replacing guanine with an easier-to-oxidize purine analogue, 7-deazaguanine, Z, (Figure 2.3) a similar trend of charge separation rate is found, however, an attenuation factor of 0.8 \AA^{-1} is obtained, which is in good agreement with in the stilbene-DNA system.⁸

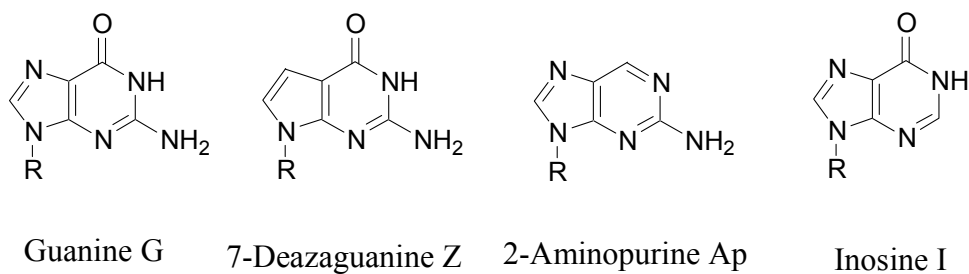


Figure 2.3 Structures of guanine G, 7-deazaguanine Z, 2-aminopurine Ap and inosine I.

Table 2.3 Rate constants for charge separation and charge recombination for Acr^+/G - DNA duplex and Acr^+/Z - DNA duplex.^{17, 18}

Acr^+ -D sequence	τ_s , ns	k_{cs} , s^{-1}	k_{rc} , s^{-1}
Acr^+ -(AT)	18		
Acr^+ -G	0.0059	1.7×10^{11}	2.0×10^{10}
Acr^+ -AG	36	2.8×10^7	-
Acr^+ -Z	0.0009	1.1×10^{12}	1.3×10^{11}
Acr^+ -AZ	0.010	8.3×10^{10}	5.9×10^9
Acr^+ -AAZ	12	3.0×10^7	-

Femtosecond dynamics of singlet population of 2-aminopurine (**Ap**), a fluorescent analogue of adenine (Figure 2.3), in DNA duplex have been reported by Zewail et al¹⁹. The singlet decay time of **Ap** is dependent on the nearest base, with a quenching trend of G > T > A > C > I, which does not follow the trend for the oxidation (G > A > I > C, T) or the reduction (T > C > A > G) potentials of the nucleotides. This indicates the the charge transfer can occur through both oxidative (by G) and reductive (by T) reactions of the nucleotides with **Ap***. Guanine oxidation reveals a strong distance dependence and becomes insignificant after three intervening base pairs, with $\beta = 0.6 \pm 0.1 \text{ \AA}^{-1}$.

Table 2.4 Fluorescence quantum yields and singlet decay times in **Ap**/G -DNA duplex.^a

Ap -G sequence	Φ_f	τ_s , ns	τ_s , ps
Ap -II	0.067	0.54(26), 3.1(74)	512
Ap -GI	0.005	0.070(54), 1.9(46)	10
Ap -AG	0.016	0.18(44), 1.3(56)	65
Ap -AAG	0.027		155
Ap -AAAG	--		179

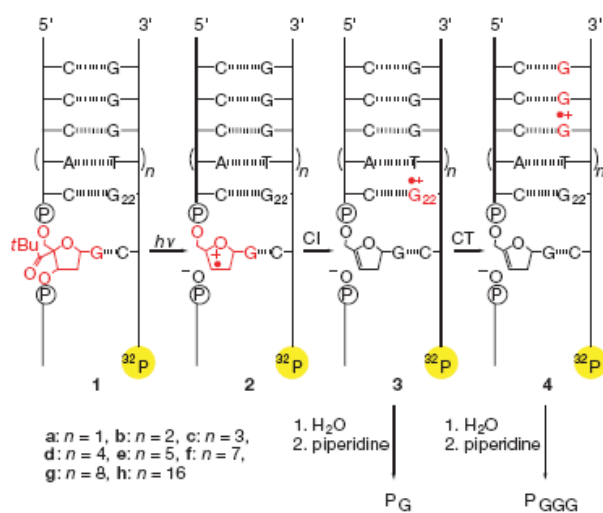
^a quantum yield and ns decay data from ref.²⁰, ps data from ref.¹⁹

In the system with tethered ethidium (**Ea**) serving as acceptor and 7-deazaguanine (**Z**) serving as donor, two ultrafast time constants of 5 ps and 75 ps have been observed.²¹ Since these two time constants are independent of the D-A separation (10-17 Å), a three-step mechanism has been suggested: first, the electronic coupling of excited **Ea**⁺* with the DNA bridge leads to a hole injection (from **Ea**⁺*-**BB**-**Z** to **Ea**[·]-**B**⁺**B**-**Z**), second, the hole transfer or hopping in between bridge bases, and third, an irreversible trapping results in a fully charge separated state (from **Ea**[·]-**BB**^{·+}-**Z** to **Ea**[·]-**BB**-**Z**^{·+}) because of the net driving force ($\Delta G \approx -0.2$ eV).

Theoretical analysis of DNA bridge-mediated ET led to the proposal that photoinduced ET might occur via either superexchange or hopping mechanisms, depending on the energetics of the donor-bridge-acceptor.²² Since the superexchange process is highly distance dependent, while the hopping mechanism is weakly distance dependent, a change in mechanism from superexchange to hopping is expected to occur at intermediate distances.²³⁻²⁵ This crossover has been observed by Giese and co-workers by site selective photochemical generation of a guanine cation radical.²⁶ They observed the hole transport from a guanine cation radical to a GGG unit with increasing the number of the intervening A:T base pairs from 1 to 16 (Figure 2.4 a). The plot of the ratio of the product after and before hole transfer, P_{GGG}/P_G , with the number of intervening A:T base pairs, shows a significant change of distance dependence (Figure 2.4b). The results prompted several theoretical models.²⁷⁻²⁹ Following thermally induced injection of a hole from the guanine cation radical to the nearest adenine, hole migration between adenine bases has been determined to be a

very rapid process, which can be due to efficient electronic coupling. Therefore the initial charge injection rate becomes the rate determine step when the number of bridge A:T base pairs exceeds 3-4.

a



b

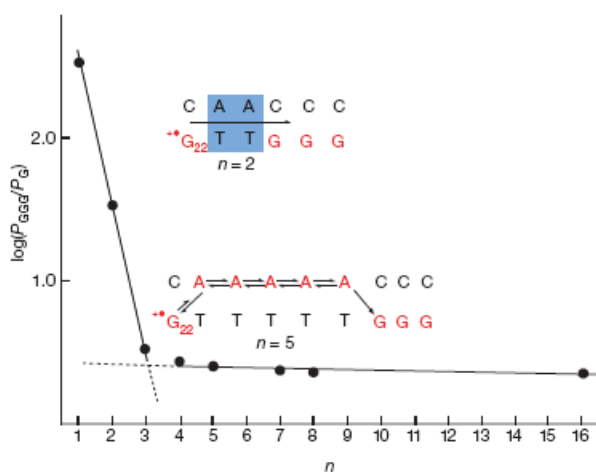


Figure 2.4 (a), Hole injection and hole transfer in G^+/GGG -DNA duplex; (b), rate constants of charge separation with distance in between donor and acceptor. ²⁶ Polt obtained for Ref 25.

We report here the results of the investigation of the dynamics and mechanisms of charge separation and charge recombination in DNA end-capped hairpin conjugates possessing donor and acceptor stilbene chromophores (**Sd** and **Sa** respectively) separated by (A:T)_n base pair domains (Figure 2.5). By observing the singlet **Sa**^{*}, anion radical **Sa**^{•-}, and cation radical **Sd**^{•+} using femtosecond and nanosecond transient absorption spectra combined with picosecond fluorescence decay data, we have for the first time investigated the various kinetic processes that are involved in the photoinduced electron transfer in DNA, which are hole injection, hole arrival, and charge recombination. We find that each process has a distinctive distance dependence, resulting in a crossover from superexchange to hopping as the mechanism for charge separation at an intermediate distance of ca. 10 Å. Previous experimental studies of DNA charge separation and charge recombination dynamics can be analyzed in terms of these two limiting mechanisms.

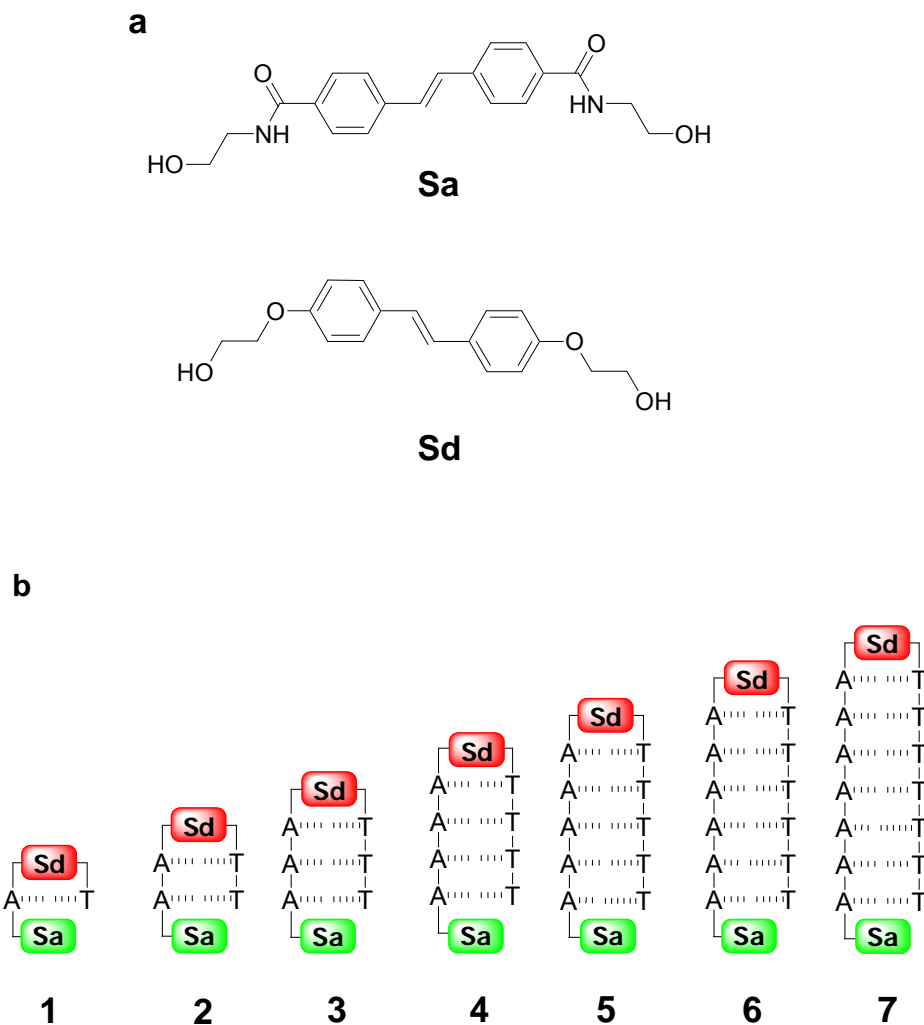


Figure 2.5 a, structures of **Sa** and **Sd**; b, end-capped hairpins with **Sa*** served as acceptor and **Sd** served as donor.

2.2 Results

2.2.1 Synthesis end-capped stilbene hairpin conjugates

Stilbene-4,4'-dicarboxylic acid was obtained from toluic acid by treatment with sulfur powder at high temperature.³⁰ The bis(3-hydroxypropyl)amide (**Sa**) synthon used as the end-cap in DNA hairpin structures was prepared via sequential reactions of stilbene-4,4'-dicarboxylic acid

with thionyl chloride and 3-hydroxy-1-propylamine.^{14,31} The preparation of the bis(2-hydroxyethyl)stilbene-4,4'-diether (**Sd**) followed the procedure of Letsinger and Lewis.^{14,31} Prior to incorporation of **Sa** and **Sd** diols into a synthetic oligonucleotide conjugates, they were converted to the monoprotected, monoactivated diols by sequential reaction with 4,4'-dimethoxytrityl chloride and with 2-cyanoethyl diisopropylchlorophosphoramidite.^{14,31} The **Sd** is chosen as the hairpin linker and **Sa** is chosen as the end-cap because of the higher coupling yield of **Sd**. The detailed synthetic procedure is described in Experiment Section **6.3**. Control hairpins **Sa-AT** and **Sd-AT** (Figure 2.6), and all end-capped oligonucleotide hairpin conjugates were prepared via conventional phosphoramidite chemistry. All conjugates in this study were first removed from solid support, and then isolated as trityl-on derivatives by RP-HPLC and detritylated in 80% acetic acid for 30 min. The presence of the stilbene linker was confirmed by UV absorption and fluorescence spectroscopy. Molecular weights were determined using a MALDI-TOF mass spectrometer.

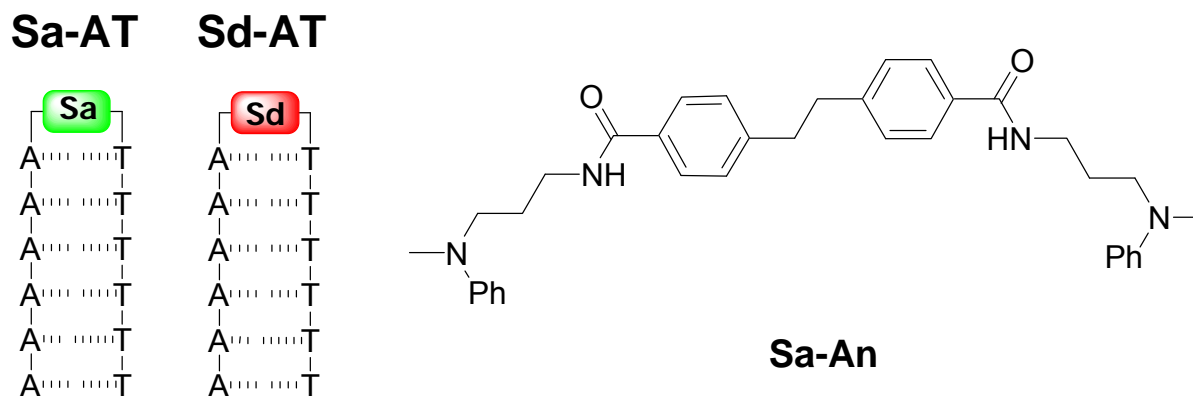


Figure 2.6 Structures of control molecules **Sa-AT**, **Sd-AT**, and **Sa-An**.

2.2.2 Absorption and fluorescence properties of end-capped hairpins

The UV absorption spectra of **Sa-AT**, **Sd-AT**, and **6** are shown in Figure 2.7 a. The 260 nm bands of all three conjugates are dominated by the absorption of base pairs, and the absorption at long wavelength is due to the stilbene absorption.^{11, 32} The stilbene region in **Sa-AT** extended to longer wavelength compared to the stilbene region in **Sd-AT**, resulting from the larger conjugation from the attached carboxylic amide groups. Since both **Sa** and **Sd** are incorporated in end-capped hairpins, **6** shows similar long wavelength absorption as **Sa-AT**. The UV absorption spectra of **1-7** are shown in Figure 2.7b. The absorption bands at long wavelength of can be superimposed, while the intensity at base pair region increases with increasing the number of intervening (A:T) base pairs.

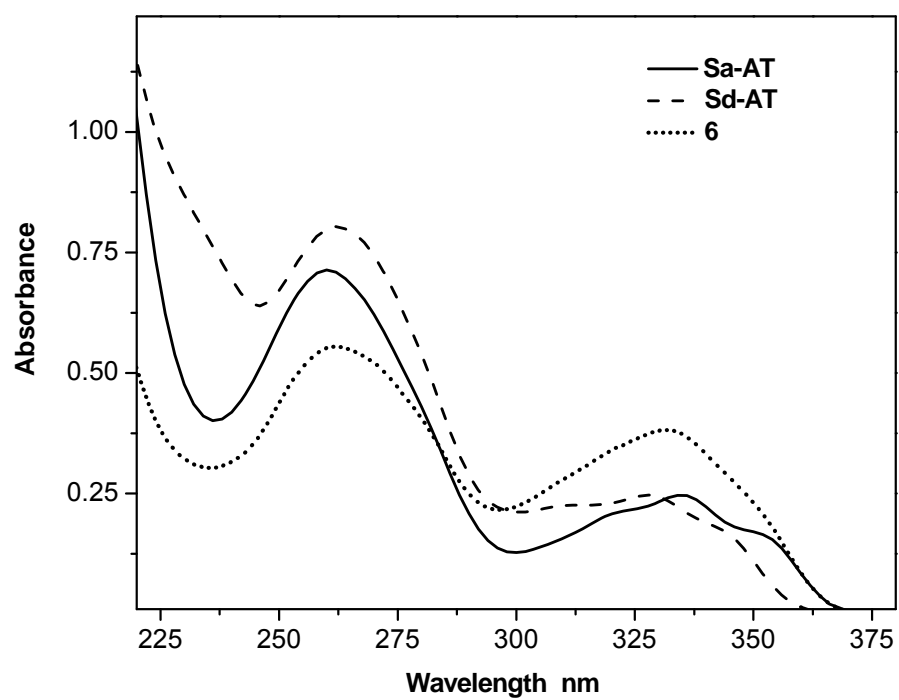


Figure 2.7a Comparison of UV absorption spectra for **Sa-AT**, **Sd-AT**, and hairpin **6**.

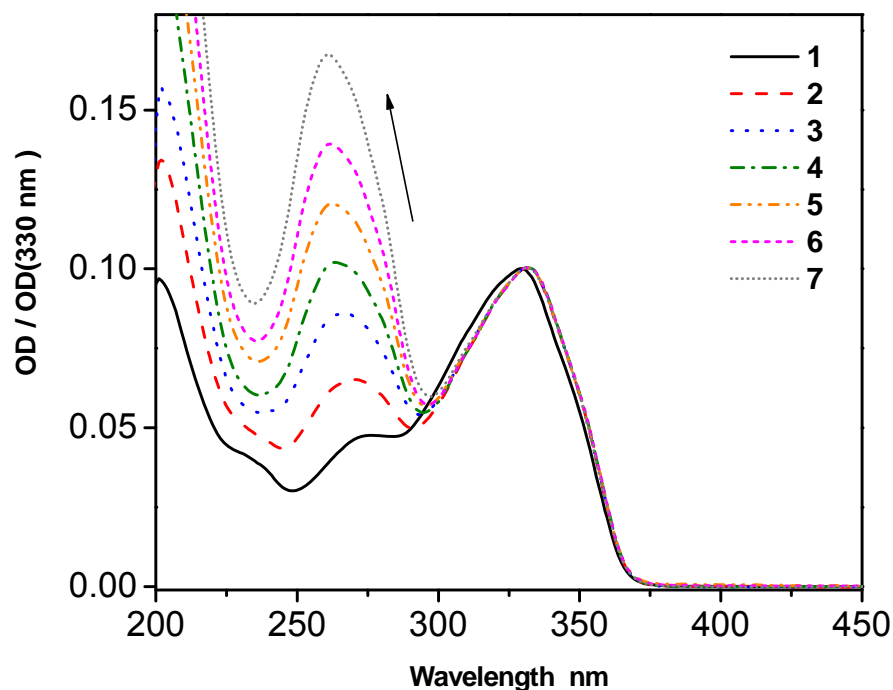


Figure 2.7b Comparison of the UV absorption spectra for hairpins **1-7**.

The fluorescence properties of **Sa** and **Sd** in methanol have been studied.^{33, 34} **Sa** has maximum emission at 386 nm with a fluorescence quantum yield of 0.11, while **Sd** has maximum emission at 374 nm with a fluorescence quantum yield of 0.32. Both have shown a single exponential fluorescence decay with lifetimes of 0.28 ns and 0.35 ns respectively. The control **Sa-AT** has fluorescence maximum at 389 nm, with a quantum yield of 0.38.¹¹ The fluorescence decay time has been reinvestigated with a time resolution of ca. 35 ps using a Ti-Sp based laser system. Consistent with previous observations with 0.2 ns instrument resolution, a long-lived decay component shows a lifetime of 2.0 ns. Interestingly, two additional short-lived

components have been observed for the first time, 45 ps and 860 ps, with about 70% amplitude in the former. **Sd-AT** is non fluorescent in aqueous solution. Control molecule **Sa-An** (Figure 2.6) shows no fluorescent as well.

Hairpin **1** is non-fluorescent, while **2-7** show the same band shape as **Sa-AT** (Figure 2.8). Fitting the fluorescence decay of **2-7** to triple exponential function shows two short-lived components and a long-lived component. The decay times and fluorescence quantum yield are summarized in Table 2.5. The decays are dominated by a short-lived component having decay times of 38-95 ps and amplitudes of 71-82%, which are similar to that of **Sa-AT**. The quantum yields for **2-7** in Table 2.5 were obtained by comparing the peak intensity to that of Sa-AT, under excitation at 355 nm.

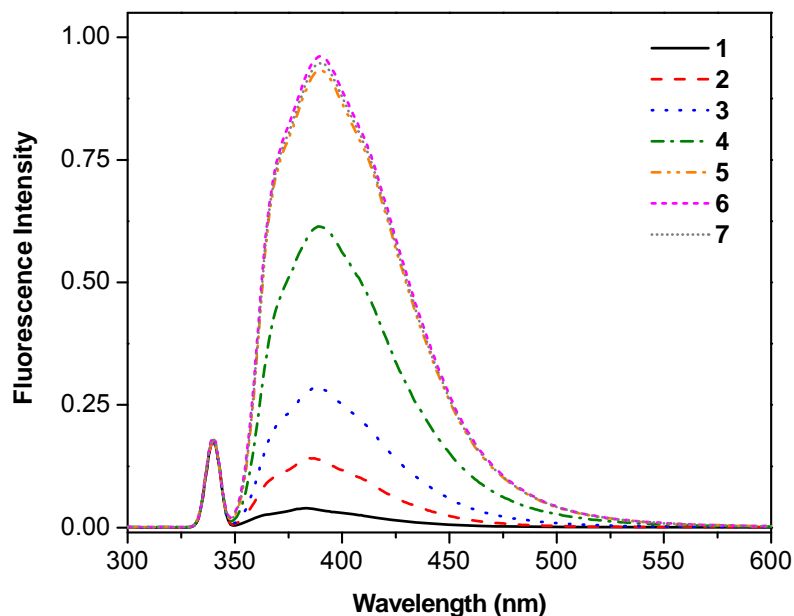


Figure 2.8 Fluorescence spectra of hairpins 1-7. (Excitation wavelength is 355 nm)

Table 2.5 Fluorescence quantum yields and decay data.^a

conjugate	Φ_f^b	τ_1 (amp), ps ^c	τ_2 (amp), ns ^c	τ_3 (amp), ns ^c
Sa ^d	0.11	280, 362 ^f		
Sd ^e	0.32	350, 379 ^f		
Sa-An				
Sa-TA	0.38 ^d	45 (71)	0.86 (8)	2.2 (21)
Sd-TA				
1	<0.01			
2	0.033	38 (73)	1.7 (25)	^g
3	0.15	66 (76)	0.37 (20)	1.4 (3)
4	0.26	40 (75)	0.58 (12)	1.4 (11)
5	0.29	81 (75)	1.24 (20)	2.0 (10)
6	0.31	95 (71)	1.26 (19)	2.0 (12)
7	0.37	43 (82)	0.89 (6)	1.9 (12)

^a Data for **Sa** and **Sd** in methanol solution. Data for **Sa-TA** and **1-7** in aqueous solution (standard buffer). ^b Quantum yield data for **1-7** determined using 355 nm excitation by comparison of the peak intensity with that for **Sa-TA**. Estimated error $\pm 10\%$. ^c Decays and amplitudes for **Sa-TA** and **1-7** determined from triple exponential fits of the 390 nm fluorescence decay. ^d Data from ref.³³ ^e Data from ref.³⁴. ^f Data from transient absorption measurements. ^g The third component ($\tau_3 = 12.7$ ns) is not considered to be significant.

2.2.3 Transient spectra of control molecules and hairpin conjugates

Femtosecond time-resolved transient absorption spectra were collected for control molecules, providing a wider probe range from 350 nm to 750 nm, compared to the previous range of 450-750 nm.^{11, 34} The spectra of **Sa** and **Sd** are shown in Figure 2.9. **Sa** and **Sd** show negative bands at 380 nm and 360 nm, which were not observed previously, with decay times of 276 ps and 380 ps. These bands are due to the simulated emission from their singlet excited states since they have similar fluorescence maxima of **Sa** and **Sd**. Also both **Sa** and **Sd** have maximum absorptions at 575 nm rising within ca 3 ps, and decay components of 362 ps and 379 ps, respectively, (Table 2.6), similar to their corresponding fluorescence decay times (Table 2.5) and decay times of stimulated emission.

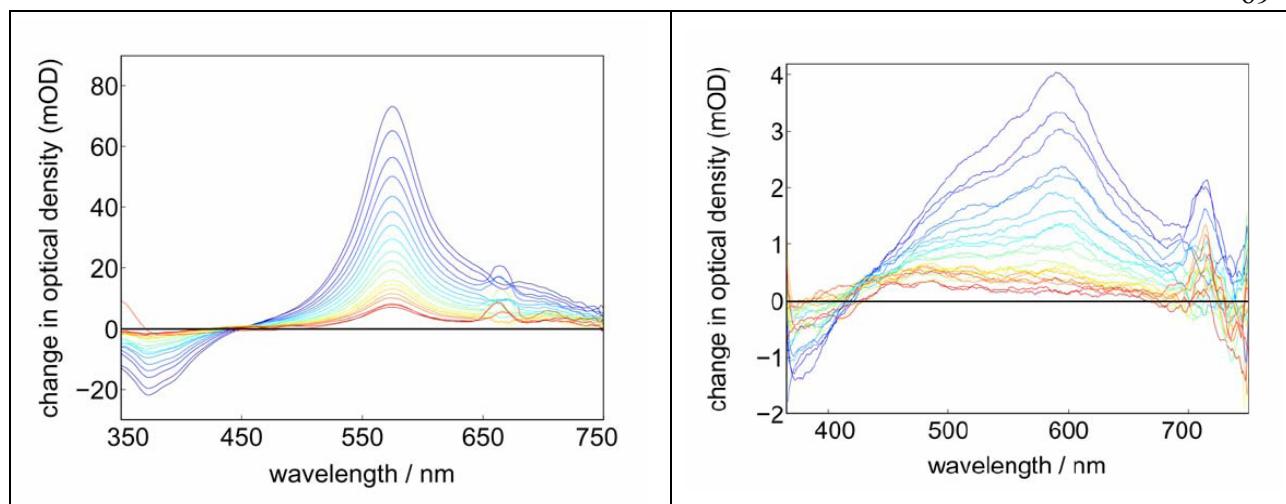


Figure 2.9 Temporal evolution of the pump-probe spectra of **Sa** (a, left) and **Sd** (b, right) in the time range of 0.2 ns to 1.2 ns after excitation at 333nm. Early spectra are shown in blue/green and late spectra are shown in orange/red colors. [Decay times for **Sa** at 570 nm are: 1.8 ps (-7.4) and 362 ps (34.7). Decay times for **Sd** at 575 nm are: 2.8 ps (19%), 7.6 ps (-23%), and 379 ps (58%).]

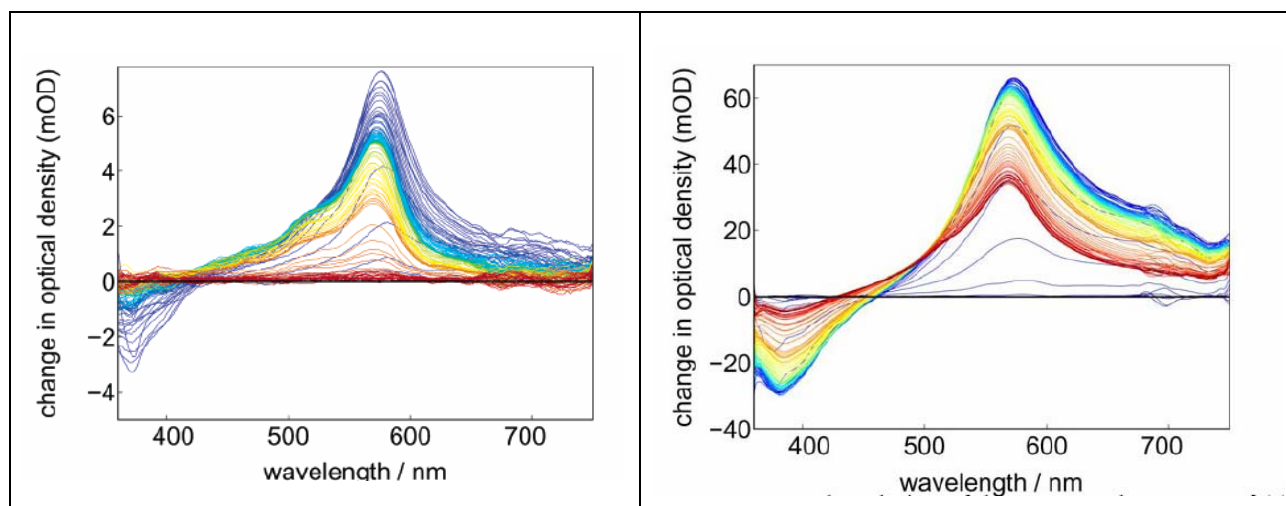


Figure 2.10 Temporal evolution of the pump-probe spectra of (a, left) **Sa-An** and (b, right) **Sa-AT** in the time range of -0.1 ps to 150 ps after excitation at 333 nm. Early spectra are shown in blue/green, and late spectra are shown in orange/red colors.

Table 2.6 Femtosecond pump-probe transient decays.^a

conjugate	380 nm τ , ps ^b	575 nm τ , ps ^c	525 nm, τ , ps ^d	525/575, ps ^e
Sa ^j		1.8 (-7.4)		
		362 (134.7)		
Sd		2.8 (19%)		
		7.6 (-23%)		
		379 (58%)		
Sa-An		20	20	<3ps
Sa-TA	23 (-19)	18 (25) ^f	930 (17)	30
	470 (-5)	790 (32) ^g	> 2 ns (3.8)	
		> 2 ns (8.4)		
Sd-TA ^h		0.6 ^f	32	
		35		
1	2.2 (-3.8)	1.5 (6.0) ^f	\sim 1.0 (-3.8) ^f	1.7
		9.3 (5.8) ^g	9.9 (9.8) ^g	
		490 (1.9) ^g	360 (4.2) ^g	
2	25 (-3.4)	24 (3.4) ^f	31 (-5.1) ^f	36
		>1 ns (7.6) ^g	> 1 ns (11) ^g	
3	53 (-0.57)	33 (1.1) ^f	41 (1.5) ⁱ	290
		> 1 ns (1.3) ^g	440 (-1.0) ^f	340 ^k
			> 1 ns (1.8) ^g	
4	77 (-1.1)	56 (2.4) ^f	43 (2.7) ⁱ	> 1 ns
		> 1 ns (2.7) ^g	> 1 ns (1.7) ^g	2.3 ns ^k
5				> 6 ns ^k
6				> 6 ns ^k
7				> 6 ns ^k

^a Rise and decay times (preexponentials in parentheses are negative for components with increasing optical density and positive for components with decreasing optical density). ^b Decay times for the stimulated emission of **Sa***. ^c Decay times for the transient absorption of **Sa*** or **Sd*** (shortest decay times) and **Sa**⁻ (longer decay times). ^d Rise and decay times for the transient absorption of **Sd**⁺ and/or **Sa**⁻. ^e Rise time for the 525/575 nm band intensity ratio attributed to hole injection for **Sa-AT** and hole arrival for **1-4**. ^f Component attributed to hole injection or hole arrival. ^g Component attributed to charge recombination. ^h Data from ref³⁴. ⁱ Component attributed to charge recombination of **Sd**⁺/**T**⁻. ^j Decay of **Sa** obtained at 570 nm. ^k Data from 0-6 ns transient spectra.

Control molecule **Sa-An** was designed to study the spectroscopic properties of the anion radical **Sa⁻**, by attaching two efficient electron donating methylaniline groups. The femtosecond transient spectra of **Sa-An** (Figure 2.10 a) show that there is a rapid rise at 575 nm and 380 nm within ca. 1ps, which is assigned to **Sa***. Within a few picoseconds, the 380 nm band and the long-wavelength tail of 575 nm band decay accompanied by a rise in the 525 nm shoulder. The intensity ratio of 525 nm to 575nm, $525/575$, reaches a maximum value of ca. 1:3 within a few picoseconds, and then both peaks decay with a decay time of ca. 20 ps. There are two possible reaction paths for **Sa*-An**. One is to return back to ground state by either fluorescence or a non-irradiative decay, and the other is to undergo charge transfer occur resulting from the different electron affinity properties of stilbene diamide motif and methylphenylamine motif (Figure 2.11). Since fluorescence was not observed for this molecule, the dominant pathway for **Sa*-An** is to form the charge separated state **Sa⁻-An⁺**. Therefore, the above changes in the transient spectra are attributed to charge separation with formation of the **Sa⁻-An⁺** radical ion pair, followed by decay due to charge recombination.¹¹ Because the **An⁺** radical cation does not have an absorption band in the range of 350 nm-750 nm, both the 575 nm band and the 525 nm shoulder are attributed to **Sa⁻**. Thus, the growth of the $525/575$ nm band intensity ratio provides a direct measurement of the charge separation time constant.

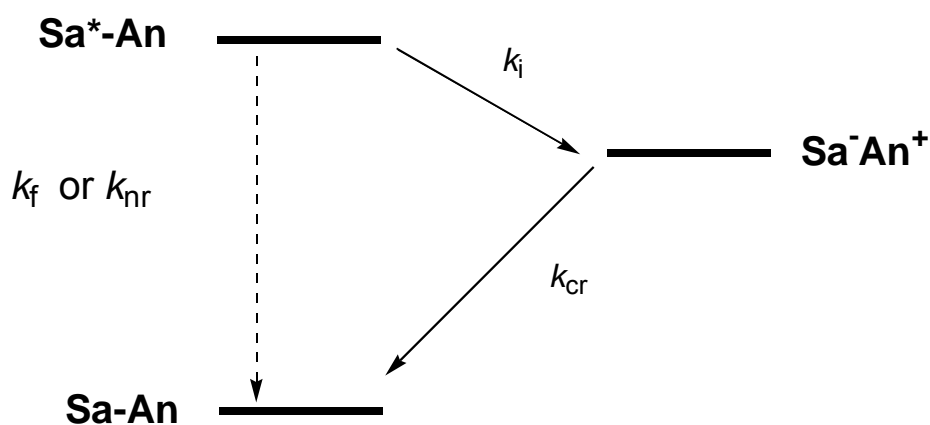


Figure 2.11 Two possible pathways for singlet Sa*-An.

Transient spectra of **Sa-AT** (Figure 2.10 b) have a similar rapid rise at 575 nm band and 380 nm negative band within ca. 1 ps after the laser pulse, both of which are assigned to Sa*.

Fitting the decay at 380 nm results two components, 23 ps and 470 ps, similar to the fitting for the 575 nm band with 18 ps and 790 ps. During the short decay component of the 380 nm and 575 nm bands there is a rise in the 525 nm shoulder, which was not observed previously.¹¹ The 525 nm and 575 nm bands reach a constant intensity ratio of ca. 1:3 with a rise time of 30 ps, indicating the formation of **Sa⁻** and then decay together with a 0.8-0.9 ns component (i.e. 790 ps for 575 nm band, and 930 ps for 525 nm band), which is similar to the long decay component at 380 nm. Meantime for 575nm and 525 nm bands, a component longer than the instrument time widow of 1.9 ns is observed. The transient data for **Sa-AT** are summarized in Table 2.6.

For **Sd-AT**, previous studies³⁴ have shown that the 575 nm band assigned to **Sd*** decays with a time constant < 0.5 ps concomitant with the growth of the 525 nm band assigned to **Sd⁺**, due to the charge separation from **Sd*-T** to **Sd⁺-T⁻**. The 525 nm band has a decay time of 32 ps assigned to charge recombination from charge separated state to ground state.

2.2.4 Transient spectra of end-capped hairpin conjugates 1-7

Femtosecond resolved transient spectra were measured for end capped hairpin conjugates **1** and **2** using 350-355 nm excitation which permits selective excitation of the **Sa** capping group, and hairpin **3** and **4** using 333 nm excitation. The nanosecond resolved transient spectra for hairpin **3-7** were measured using 355 nm excitation.

In the transient spectra of **1** (Figure 2.12 a) there is an ultrafast rise (< 1 ps) in the 575 nm band, which is assigned to the absorption of **Sa*** and a negative band at 380 nm assigned to **Sa*** simulated emission since **Sd-AT** is nonfluorescent. The initial ultrafast rise of 575 nm band and 380 nm band is followed by the decay with time constants of ca. 2 ps. Since there is only one (A:T) base pair in between donor **Sd** and acceptor **Sa***, a charge separation process is expected to occur with formation of **Sa⁻** with a ratio of 1:3 of 525/575 nm band, as observed for **Sa-TA**. However, in a time constant of 1.7 ps the ratio of 525/575 nm bands was directly observed, reaching the maximum of 2.2:1, (Figure 2.13) followed by decay of both bands. If a full charge separation between **Sa** and **Sd** occurs, then an additive absorption spectrum of **Sa⁻** and **Sd⁺** is expected. This will result in a ca. 2:1 ratio of 525/575 nm band intensities from overlapping

Sa^{•-} (1:3 of 525:575 nm) and **Sd^{•+}** (525 nm only), assuming that both radical ions have similar molar absorbance. The observed ratio of 2.2:1 of 525/575 nm bands indicates charge separation between **Sa** and **Sd** has occurred and the time of reaching the maximum ratio of 525/575 nm bands is the time required for charge separation, i.e., hole arrival time. The decays of the 525 nm and 575 nm bands have time constants of ca. 9 ps and 0.4 ns (Table 2.6).

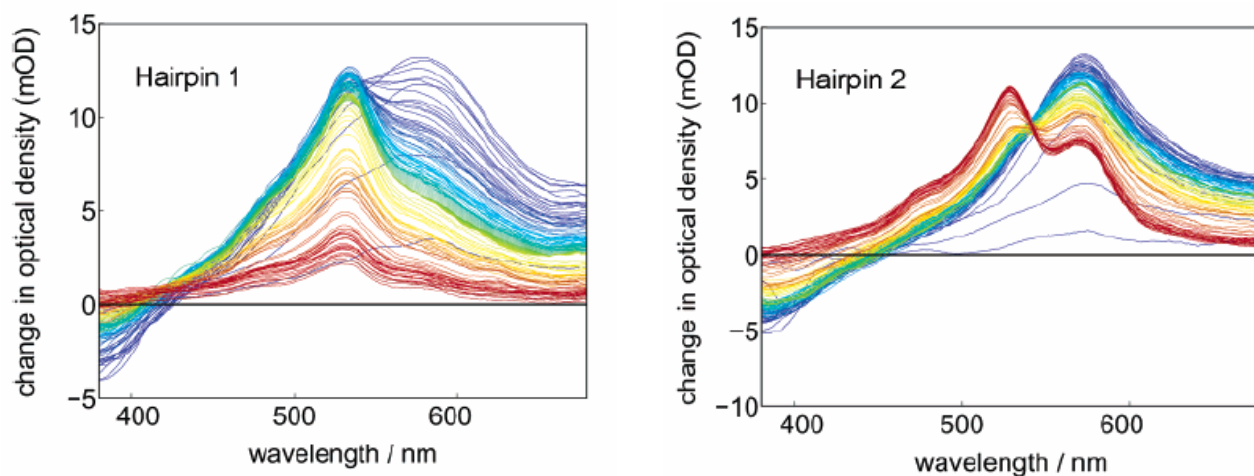


Figure 2.12 Temporal evolution of the pump-probe spectra of hairpins **1** (a, left) and **2** (b, right) in the time range of -0.1 ps to 150 ps after excitation at 355 nm.

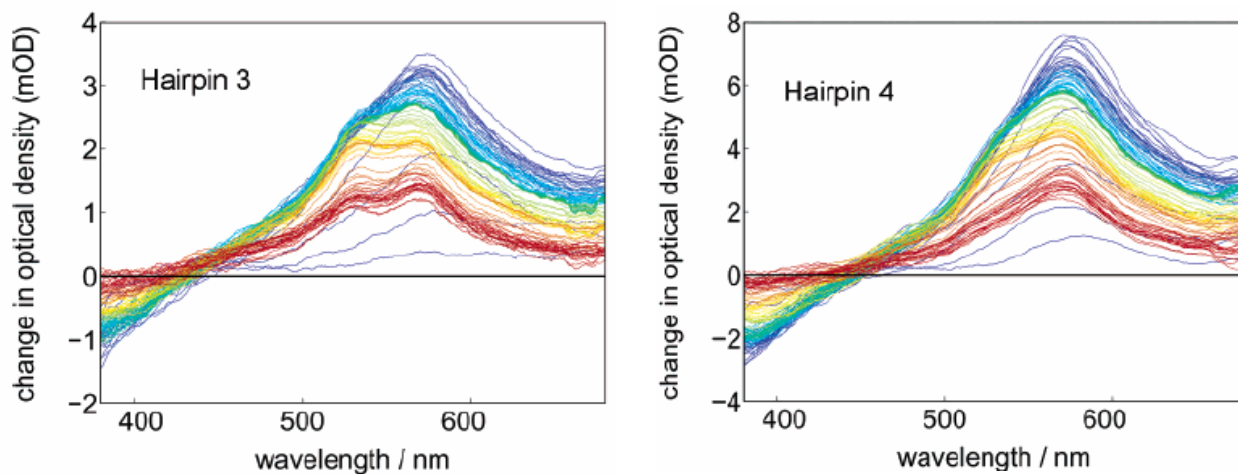


Figure 2.13 Temporal evolution of the pump-probe spectra of hairpins **3** (a, left) and **4** (b, right) in the time range of - 0.1 ps to 150ps after excitation at 333 nm.

The spectral changes observed for hairpin **2** (Figure 2.12 b) are similar to **1**. They shows an initial ultrafast rise (< 1 ps) of 575 nm of the transient absorption of **Sa*** and **Sd***, which is similar to **1**. The rise is followed by a fast decay of the 380 nm and 575 nm bands (ca. 1 ps), attributed to relaxation of the singlet excited states. Then the decay of 380 nm band and the 575 nm band, and the rise of 525 nm band occur with a time constant of 24-36 ps. The changes in the ratio of 525/575 nm bands is in slower than for **1** (Table 2.6). The 525/575 nm band intensity ratio rises with a time constant of ca. 36 ps. (Figure 2.14) The decay of the 525 and 575 nm bands is incomplete after 1.9 ns, which indicates a slow charge recombination process from fully charge separated state **Sa⁻-(AT)₂-Sd⁺** to ground state.

Changes in femtosecond transient spectra of **3** (Figure 2.13 a) occur more slowly than in the case of **1** and **2**. Following the fast relaxation process occurring within 1-2 ps, the 380nm band and 575 nm band start to decay with a time constant of 33-53 ps, which is assigned to the time needed for hole injection since it has the same time scale as for control hairpin **Sa-AT**. When hairpin **3** is excited at 333 nm, before the rise of 525 nm band there is a decay component of 41 ps. This is due to the decay from **Sd⁺-T⁻** to **Sd-T**, since the excitation at 333 nm also cause the direct excitation of **Sd**, and this time constant is similar to the one in control **Sd-TA**³⁴ (32 ps, Table 2.6). However no initial decay at 525 nm has not been observed in the case when hairpin **3** is excited at 355 nm (data not shown) Following this initial decay at 525 nm, a rise with time constant of 440 ps has been observed, which is attributed to charge separation between **Sa** and **Sd**. A similar decrease-increase phenomenon is observed in the 525/575 nm band intensity ratio

(Figure 2.13), which has a rise time constant of 0.29 ns in 2 ns instrumental resolution or 0.34 ns in 6 ns instrumental resolution. Decay of the 525/575 nm bands is incomplete in 2 ns instrumental resolution, which indicates a slow charge recombination process. Using nanosecond detection, decay time constants of 220 ns for 575 nm band, and 230 ns for 525 nm band have been obtained (Table 2.7).

Table 2.7 Nanosecond laser flash photolysis transient decays.^a

conjugate	575 nm, μ s	525 nm, μ s
Sa-TA	0.29	
2	0.0084 ^b	
3	0.22	0.23
4	8.5	8.4
5	30	30
6	160	140
7	590	830

^a Single exponential fits to the transient decays. ^b Data from ref.³⁵.

The changes of hairpin **4** are very similar to **3**, except for occurring in a much slower manner (Figure 2.13 b). In the 6 ns detection window, the ratio of 525/575 nm band reaches its maximum in a time constant of 2.3 ns, which is longer than previously estimated 1 ns³⁶ in 2 ns detection window.

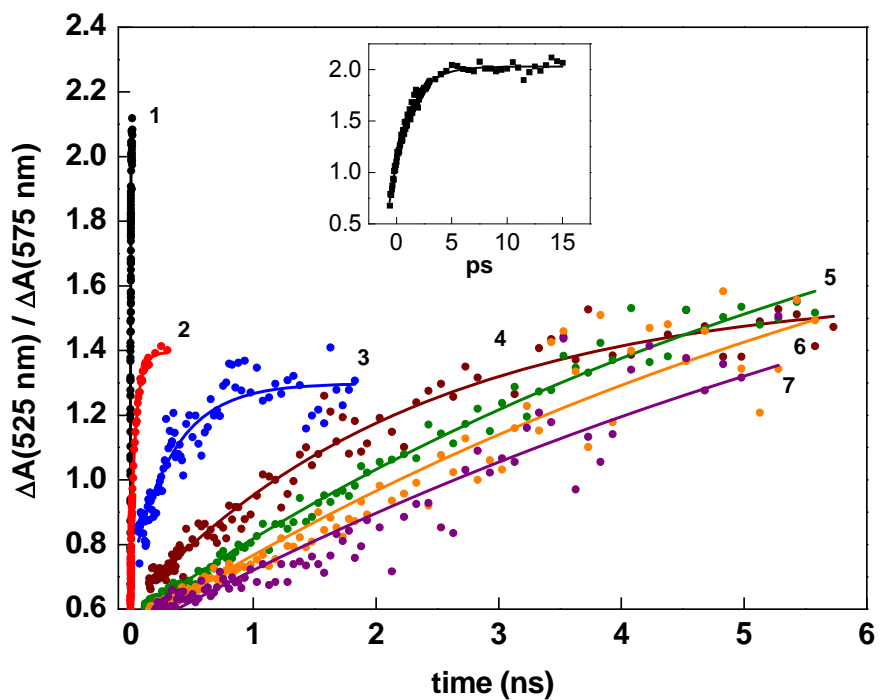


Figure 2.14 Time-dependent 525/575 nm band intensity ratios for **1-7**. (data for **1** and **2** from reference³⁶). The curved lines for **3-5** are single exponential fits to the data obtained following the initial fast rise attributed to hole injection (≈ 100 ps). The straight lines for **6** and **7** are linear fits to the 0.2–2.0-ns data.

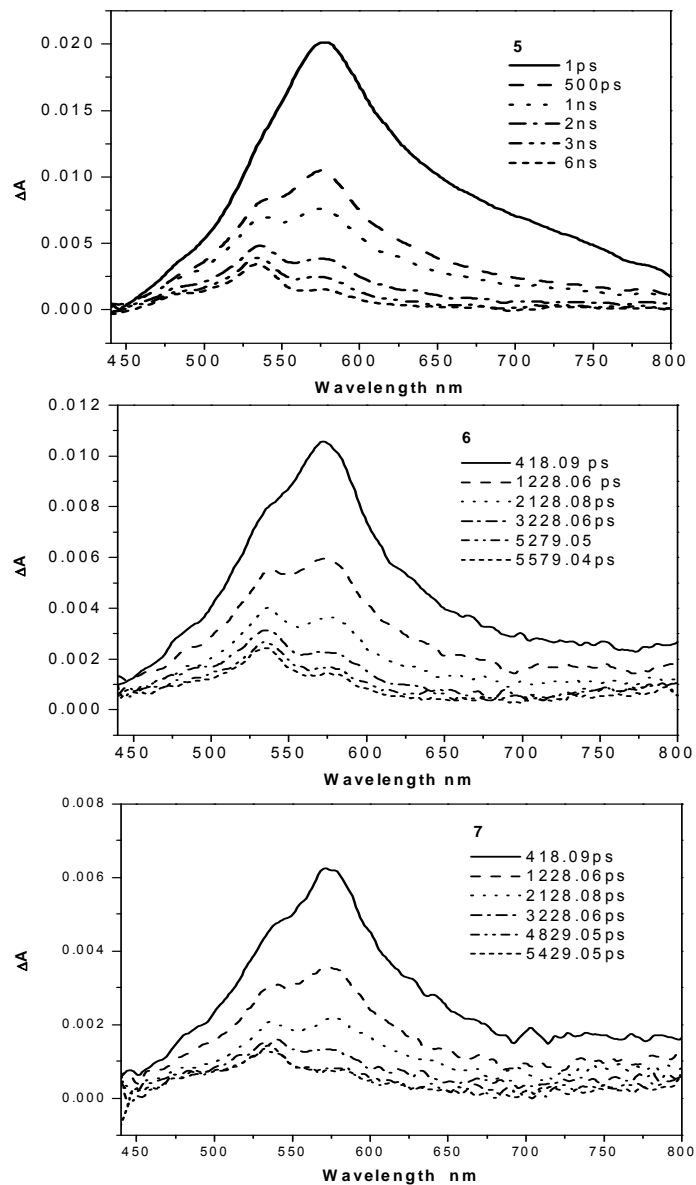


Figure 2.15 Temporal evolution of the pump-probe spectra of hairpins **5** (top), **6** (middle) and **7**(bottom) in the time range of 0.1 ps to 6 ns after excitation at 355 nm.

For hairpins **5-7**, longer time constants are expected for hole arrival, which is consistent with an incomplete rise of the 525/575 nm band intensity ratio in 6 ns (Figure 2.15 and 2.14). In the nanosecond transient spectra, only decay of 525 nm and 575 nm bands was observed, with no observable rise of the ratio of 525/575nm bands (Figure 2.16). This indicates the rise times for **5-7** are either comparable to or faster than the instrument response time (30 ns) in nanosecond detection. Decay traces obtained at 525 and 575 nm are best fit by single-exponential functions, which are assigned to charge recombination. The data for **3-5** in Figure 2.14 obtained following the initial rise in the 525/575 nm intensity ratio (≈ 100 ps), which occurs upon hole injection, was fit to first order kinetics.³⁶ The rate constants for hole arrival (k_a) and hole arrival times ($\tau_a = k_a^{-1}$) obtained from these fits are reported in Table 2.8. The straight lines for **6** and **7** are the initial slopes for the rise in the 525/575-nm ratio (0.2-6.0 ns). Comparison of these slopes with that for **5** provides values of k_a and τ_a for **6** and **7**. The values of $\tau_a = 6-8$ ns for **5-7** are consistent with previous failure to observe hole arrival on the time scale of 2 ns.

The efficiency of charge separation (Φ_t) to the hole trap **Sd** can be estimated by comparing the integrated area of the transient spectra at approximately 10 ps, which indicates the amount of excited **Sa***, with the integrated area of the transient spectra after the 525/575-nm band ratio reaches its maximum value, data shown in Table 2.8. In the case of **1** and **2**, the $\Phi_t \approx 1.0$ is assumed based on the faster hole arrival times and absence of significant **Sa** fluorescence. The values of Φ_t decrease rapidly for **2-4** and more gradually for **5-7**.

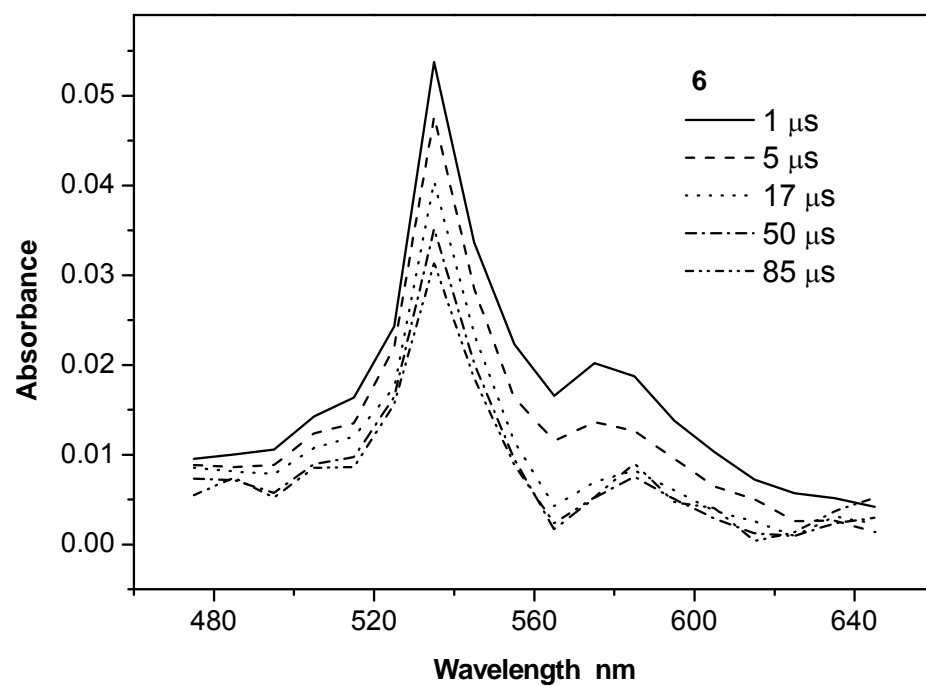


Figure 2.16 Nanosecond time-resolved spectra of **6**. The 525 nm band is assigned to overlapping absorption of Sd^+ and Sa^- , and the 575 nm band is assigned to absorption of Sa^- .

Table 2.8 Hole trapping quantum yields, hole arrival rate constants, and hole arrival times for charge transfer in hairpin **1-7**.

hairpin	$\Phi_t^{[a]}$	τ_a , ns ^[c]	$10^{-9} k_a$, s ⁻¹ [b]
1	1.0 ± 0.1	0.0017 ^[d]	580 ^[d]
2	1.0 ± 0.1	0.036 ^[d]	27 ^[d]
3	0.2 ± 0.04	0.34	2.9 ± 0.3 (3.4 ^[d])
4	0.05 ± 0.02	2.4	0.42 ± 0.06
5	0.04 ± 0.02	5.9	0.17 ± 0.02
6	0.02 ± 0.01	6.6	0.15 ± 0.03
7	0.02 ± 0.01	7.8	0.12 ± 0.04

[a] Estimated quantum yields and errors for hole trapping (see text). [b] Rate constants for hole arrival and estimated errors obtained from single exponential fits to the data in Figure 2.15. [c] Hole arrival time $\tau_a = k_a^{-1}$. [d] Data from ref. 16.

2.3 Discussion

Rate constants for charge separation and charge recombination in **Sa/G** systems (Table 2.1) were obtained from analysis of the femtosecond transients assigned to the decay of **Sa*** and **Sa⁻**. The formation and decay of **G⁺** is not directly observed due to the absence of measurable transient absorption. Analysis of the kinetic data for **Sa/G** hairpins using a superexchange model provided a distance dependence of $\beta = 0.65 \text{ \AA}^{-1}$ for charge separation and $\beta = 0.95 \text{ \AA}^{-1}$ for charge recombination.⁸

Donor-acceptor capped hairpin systems related to **2-7** were introduced several years ago

for the study of DNA electron-transfer dynamics and exciton-coupled circular dichroism.^{35, 37}

The lower oxidation potential of **Sd** ($E_{\text{ox}} = 0.92$ V vs SCE) versus G results in more exergonic photoinduced electron transfer ($\Delta G_{\text{et}} = -0.52$ eV) than the value estimated with G as the electron donor. The well-resolved transient absorption spectra of the **Sa⁻/Sd⁺** charge-separated state provide definitive evidence for the occurrence of charge separation and charge recombination via a DNA bridge. The values of β for charge separation and charge recombination in these systems are similar to those for the **Sa/G** hairpin systems.³⁵ However, in the published transient data neither the **Sa/G** nor the **Sa/Sd** system serves to distinguish between a single-step superexchange process and a multistep hopping process, in which the distance-dependent time constant for charge separation would, in effect, become the hole arrival time on guanine.

2.3.1 Properties of linker Sa and hairpin Sa-AT

The wider spectral range of the femtosecond pump-probe measurements permits observation of the stilbene stimulated emission, which has the same decay time as the fluorescence and transient absorption (Table 2.5 and Table 2.6). The covalently linked donor-acceptor **Sa-An** serves as a model for conversion of the **Sa*** singlet state to the anion radical **Sa⁻**.¹¹ Its pump-probe spectra in methanol (Figure 2.10a) display growth of the **Sa*** 575 nm transient absorption and 380 nm stimulated emission within the first picosecond, followed by rapid decay of the 380 nm band and of the red-edge of the 575 nm band, as well as growth of the 525 nm shoulder, with time constants of ca. 1.0 ps. The resultant spectrum is assigned to **Sa⁻**. It

has a 525/575 nm band intensity ratio of ca. 1:3 and a decay time of ca. 20 ps. The rise and decay times are faster than those previously determined in tetrahydrofuran solvent,¹¹ in accord with the known effect of solvent polarity on the dynamics of charge separation and charge recombination in donor-acceptor systems with flexible tethers.^{24, 38}

The high fluorescence quantum yield, long fluorescence decay time, and absence of pronounced changes in the transient absorption band shape, in previous studies of **Sa-AT**, were taken as evidence for the absence of photoinduced charge separation in **Sa-AT** after excitation.¹¹ The femtosecond pump-probe spectra of **Sa-AT** (Figure 2.10b) reveal both a fast decay of the stimulated emission of **Sa*** and a rise of the 525/575 nm band intensity ratio, similar to the changes observed for **Sa-An** (Figure 2.10a). The decay and rise processes have time constants of 20-30 ps (Table 2.6). Reinvestigation of the fluorescence properties of **Sa-AT** with picosecond time resolution reveals a major fluorescence decay component having a decay time of 45 ps, near the time resolution (35 ps) of the picosecond fluorescence instrument (Table 2.5). Both the decay of the fluorescence and the 575 nm femtosecond transient absorption of **Sa-AT** display longer lived components with decay times of 0.5-2.0 ns (Tables 2.5 and 2.6).

From these observation, hole injection to the poly(A:T) base pair domain has been proposed for **Sa-AT**, resulting the fast decay of **Sa*** and formation of **Sa[·]** in **Sa-AT**. The hole injection occurs with a rate constant of $k_i \approx 3 \times 10^{10} \text{ s}^{-1}$ (Table 2.9), significantly slower than the

Table 2.9 Summary of kinetic data for hole arrival, hole injection, and charge recombination.

conjugate	hole arrival $10^{10} k_s, s^{-1}{}^a$	hole injection $10^{10} k_i, s^{-1}{}^b$	charge recombination $10^8 k_{cr}, s^{-1}{}^c$
Sa-TA		3.3 ^b	
1	58		24
2	2.7	2.6(4.0)	1.2
3	0.29 ± 0.3(0.34)	1.5 (1.9)	4.4 × 10 ⁻²
4	0.043 ± 0.03	2.5(1.3)	1.2 × 10 ⁻³
5	0.015 ± 0.02	1.2	3.3 × 10 ⁻⁴
6	0.012 ± 0.03	1.1	6.7 × 10 ⁻⁵
7	0.008 ± 0.03	2.3	1.4 × 10 ⁻⁵

^a from the Table 2.8. ^b Estimated from the fast component of fluorescence decay (Table 2.5) or from the decay of the 380 nm stimulated emission (data in parentheses, from Table 2.6.). ^c Estimated from the average of the 525 and 575 nm transient decays (Tables 2.6 and 2.7).

rate constant of $1 \times 10^{12} s^{-1}$ previously reported for oxidation of a neighboring guanine by **Sa***.¹²

The longer lived 0.86 and 2.2 ns fluorescence decay components (Table 2.5) and similar transient decays (Table 2.6) for **Sa-AT** are attributed to the charge return processes from charge separated states with one or more A:T base pairs separating the radical ions. This charge return process to regenerate the fluorescence singlet state is commonly observed for singlet contact radical ion pairs and donor-bridge-acceptor charge separated states.³⁹⁻⁴² Alternatively, the longer lived fluorescence decays might be attributed to multiple hairpin conformations with different lifetimes, as has been suggested for aminopurine fluorescence decay in DNA duplex structures.^{19,}
⁴³ However, molecular dynamics simulations for **Sa**-capped hairpins indicate that they are conformationally homogeneous.⁴⁴ Furthermore, the similarity of the fluorescence and 575 nm

transient decay times for **Sa-AT** suggests that the decay of **Sa*** and of **Sa[•]** are related processes, in accord with the occurrence of reversible hole injection.

2.3.2 Charge separation (hole arrival) in donor-acceptor hairpins

The observation of hole injection in **Sa-AT** suggests that charge separation in **1-7** might occur via either previously proposed superexchange mechanism^{35,37} or hopping mechanism not observed before. Since the rise time of the 525/575 nm band intensity ratio provides the time required for arrival of a hole on **Sd**, rate constants for hole arrival, k_a (τ_a^{-1}), for **1-4** can be obtained from femtosecond³⁷ pump-probe data (2 ns detection limit for **1-2**, 6 ns detection limit for **3-4**), which are summarized in Table 2.8, and Figure 2.17. Hole arrival rates for **5-7** are too slow for study with our femtosecond apparatus and too fast for our nanosecond apparatus. However through fitting method as described in results section 2.2.4, hole arrival times for **5-7** have been estimated as reported in Table 2.8. The plot of k_a versus R_{DA} for hairpin **1-7** parallels Giese's plot for relative hole-transport efficiencies from G to GGG²⁶ (Figure 2.17), indicating a possible change in mechanism as proposed in Giese's system.

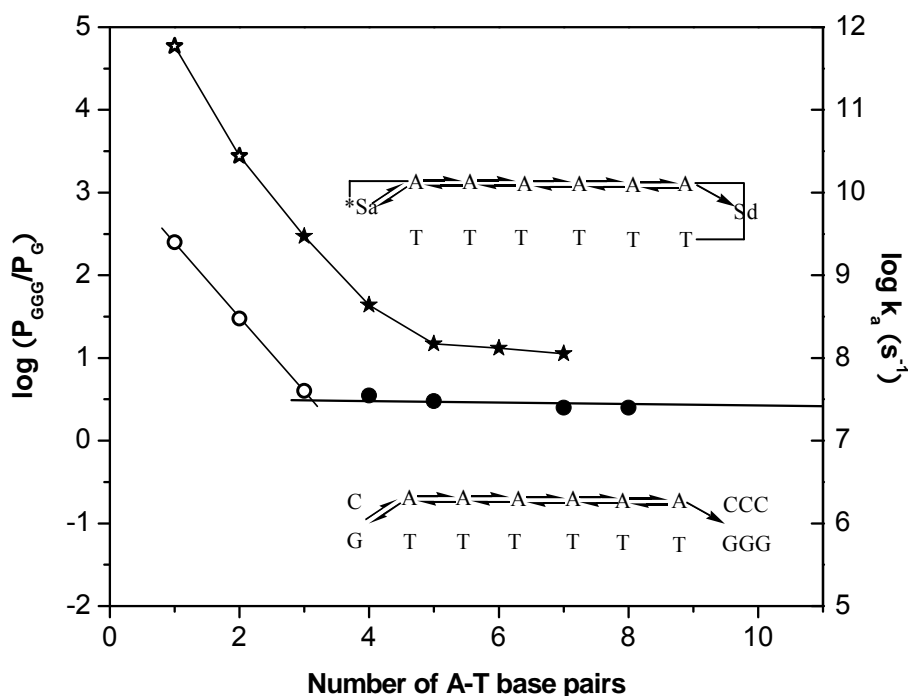


Figure 2.17 Rate constants for hole arrival in hairpins **1-7** (right Y axis, data from Table 2.8) and Relative efficiencies of strand cleavage at G vs. GGG (left Y axis, data from ref ²⁶). Open symbols for tunneling and filled symbols for hopping mechanisms.

The **Sa*** decay times for **1-4** can be obtained from the decay of the 380 nm stimulated emission (Table 2.6), and the decay times for **2-7** can be obtained from the fluorescence decays (Table 2.5).

In the case of **1**, the decay time of **Sa*** at 380 nm (2.2 ps) is similar to the rise time for **Sd⁺** (1.7 ps), both of which are significantly faster than the hole injection time for **Sa-AT**. In the case of **2**, the decay time of **Sa*** at 380 nm (25 ps) is similar to the formation time of **Sd⁺** (36 ps), both of which are similar to hole injection time for **Sa-AT**. This leads to a conclusion that

charge separation occurs through single-step superelectron transfer process. The assignment of transients and the kinetic behavior of **1** can be summarized in Figure 2.18. It is possible that the behavior of **1** is influenced by nondegenerate exciton coupling between the two stilbenes. A 5 nm red-shift in the absorption maximum is observed for a capped hairpin possessing two **Sa** chromophores separated by a single base pair, in agreement with a calculated exciton splitting of 560 cm^{-1} .²² However, there is no detectable shift in the absorption or fluorescence spectra of **1** when compared to **2-7**.

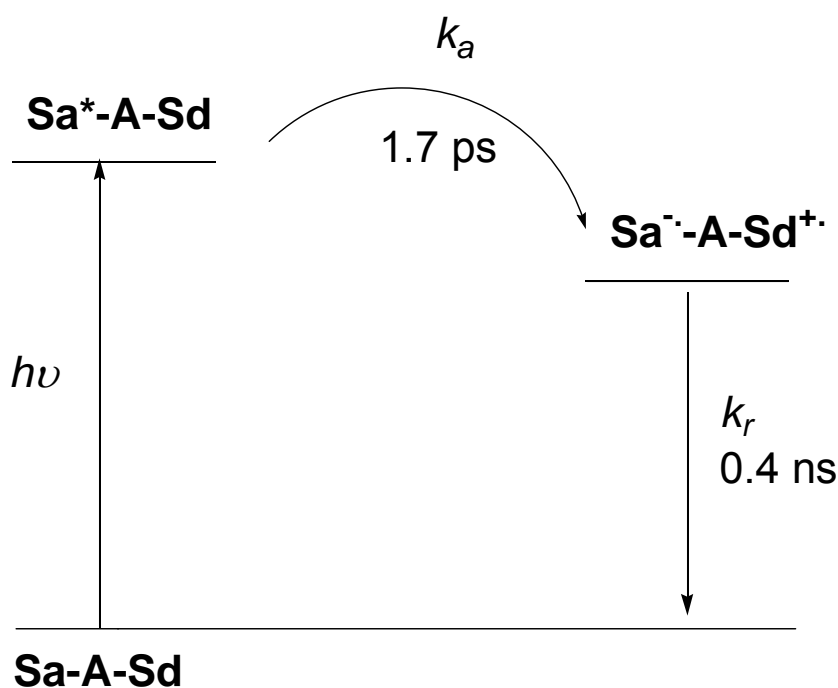


Figure 2.18 kinetics of **1**.

In the case of **3-4**, with a time window of 0-6 ns, the observed hole arrival times (Table 2.6, 340 ps for **3**, and 2.3 ns for **4**) are much longer than the fast decay component of **Sa***, which is attributed to hole injection. Therefore a hole-hopping mechanism for charge separation is proposed for **3** and **4**. The hole arrival times for hairpins **5-7** are too long to be measured by femtosecond transient spectroscopy (6 ns time window), and they are also too short for measurement by conventional nanosecond transient spectroscopy (≈ 20 ns time resolution), therefore the hole arrival times are obtained as described in result section 2.2.4 (Table 2.8). Values of k_i for **5-7** estimated from the fluorescence and 380 nm transient decays are reported in Table 2.9. Comparing k_a with k_i for **3-7**, the fact that k_a is smaller than k_i indicates that hole-hopping mechanism is adopted for **3-7**. This mechanism involves a hole injection (k_i), hole migration or hole transport via A-hopping (k_m), and hole trapping by **Sd** (k_t), in which hole migration is rate determining step, assuming hole trapping is faster than hole migration. The crossover in the mechanism for charge separation occurs at 3 intervening base pairs or ca. 10 \AA , while in studies of Giese et al, the onset of crossover occurs when there are 4 intervening base pairs.²⁶ The slope obtained from a linear fit to the data for **1-4** provides a value of $\beta = 0.67 \text{ \AA}^{-1}$, essentially the same as that reported previously for charge separation in **Sa/G** hairpin systems ($\beta = 0.65 \text{ \AA}^{-1}$)⁸. The slope obtained for **4-7** provides a value of $\beta = 0.05 \text{ \AA}^{-1}$.

The photoinduced charge-separation process for **3-7** can be described in terms of hole migration through either a localized hole-hopping model²⁸ (Figure 2.19a), or through a delocalized hole model (Figure 2.19b). Several theoretical models that have been developed to

explain Giese's results.²⁶ Berlin et al. have described A-tract hole migration as a motion in the tight-binding band.²⁷ Conwell has advanced a polaron model in which the hole is delocalized over 3–5 adenine molecules,^{45, 46} and an ion-gated polaron-like hole-transport model has been proposed by Schuster, Landman, and co-workers.⁴⁷ Renger and Marcus proposed a delocalized state model in which the splitting between bridge states increases as the bridge becomes longer.⁴⁸ The Conwell and Renger–Marcus models are consistent with our observation of a more-pronounced decrease in the hole-transport rate for **3 - 5** than is obtained at longer distances, at which point transport of the delocalized hole becomes possible.

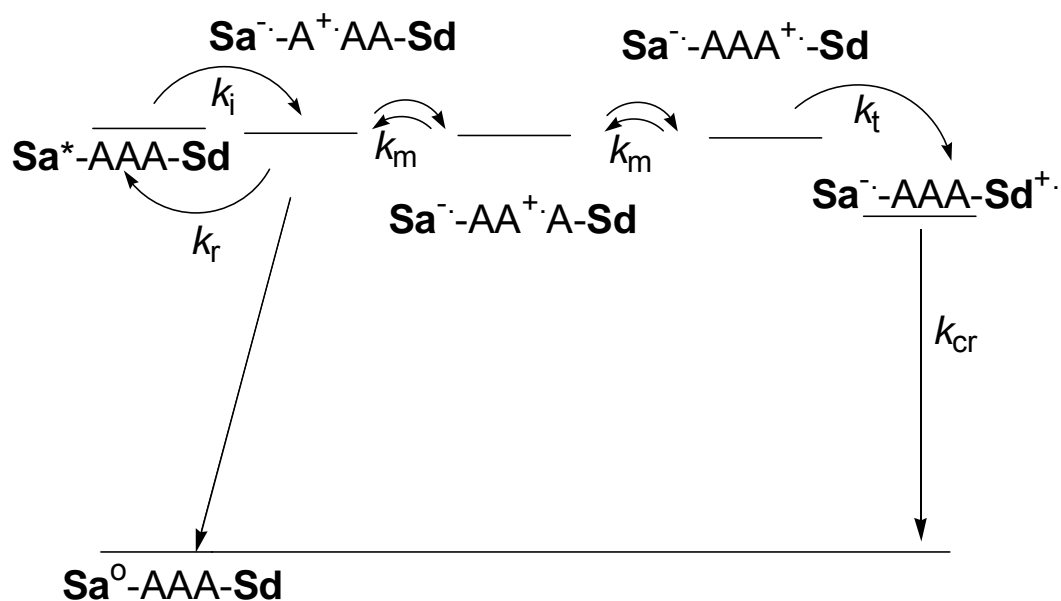


Figure 2.19a Simplified kinetic scheme using localized hole hopping model for **3**. hole injection (k_i), hole hopping or hole migration (k_m), hole trapping (k_t), charge return of $\text{Sa}^{\cdot-}/\text{A}^+$, charge recombination of $\text{Sa}^{\cdot-}/\text{Sd}^{\cdot+}$ (k_{cr}).

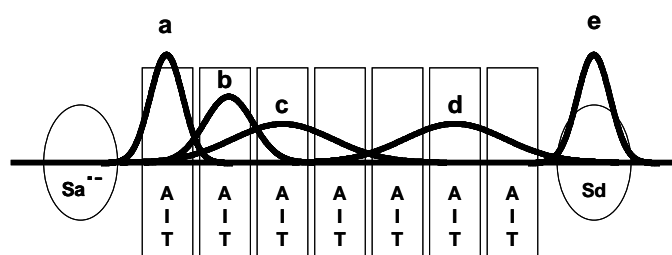


Figure 2.19b Delocalized hole hopping model for **7**. (a) the $\text{Sa}^{\cdot-}/\text{A}^+$ contact radical ion pair, (b and c) hole delocalization, (d) hole migration, and (e) hole trapping on **Sd**.

2.3.3 Hole injection in end-capped Sa/Sd hairpin systems

The observation of both short-lived and long-lived components for the fluorescence decay of hairpin **3-7** and stimulated emission in **Sa-AT** indicates that the hole injection process is

reversible. Therefore two components are from two different kinetic processes. The fast 40-90 ps fluorescence decay components presents the formation of a $\text{Sa}^{\cdot-}/\text{A}^{\cdot+}$ contact radical ion pair, while the longer lived components may come from the charge return from $\text{Sa}^{\cdot-}/\text{A}^{\cdot+}$ contact radical ion pairs separated by two or more A:T base pairs. These short-lived fluorescence decay times are independence of the length of the A-tract in **3-7**, and they are much slower than the 1 ps hole injection time of $\text{Sa}^*-\mathbf{1GC}$ for the Sa^*/\mathbf{G} system.¹² Studies of the driving force dependence of hole injection to an adjacent nucleobase in DNA hairpins indicates that a Sa^* decay time of ca. 40 ps is corresponding to a value of $\Delta G_i(\text{Sa}^*-\mathbf{AT}) \approx 0$ eV.¹² Comparison to the value of $\Delta G_i(\text{Sa}^*-\mathbf{1GC}) = -0.2$ eV for photooxidation of G suggests that the difference in oxidation potentials for G versus A is ca. 0.2 eV. However, the $\Delta G_i(\text{Sa}^*-\mathbf{AT}) = -0.2$ eV calculated from the Weller equation using nongaseous oxidation potentials⁴⁹ provides a difference in oxidation potentials for G vs A is ≈ 0.4 eV. The smaller difference we observed is consistent with estimates from time-resolved charge-transfer dynamics in bimolecular nucleotide complexes and with studies of hole transport dynamics and equilibria.^{50, 51} Therefore we conclude that hole injection from Sa^* to adjacent adenine in end-capped **Sa/Sd** hairpin systems occurs with in a time constant of 40 ps in a reversible fashion.

2.3.4 Hole migration in A-tracts

Poly(dA)-poly(dT) base pairs have been adopted in our donor-acceptor end-capped **Sa/Sd** hairpins for electron transfer study. Studies have shown that positive charge is able to migrate

over long distances in poly(dA)-poly(dT) base pairs domains, known as “A-tracts”.⁵² Takada et al. have estimated a value of $2 \times 10^{10} \text{ s}^{-1}$ for the rate constant for A-hopping from an analysis of the distance dependence of the quantum yields for charge separation in systems having a naphthaldiimide acceptor and phenothiazine donor.⁵³

In our study, the similar values of hole arrival time τ_a (Table 2.8) for **5–7** suggests that hole transport becomes weakly distance dependent at long distances. The differences in τ_a values for **5–7** provide an incremental value of approximately 2 ns per bp for a hole-hopping mechanism (Figure 2.19a), which may become shorter at even longer distances as the hole moves further away from Sa^- . This value is slower than the value of 50 ps per bp, which was estimated by Takada et al.⁵³ An estimated hopping rate of approximately 10^9 s^{-1} can be used to calculate a value of $4 \times 10^{-5} \text{ cm}^2 \text{ V}^{-1} \text{ s}^{-1}$ for A-tract hole mobility, μ , from the relation $\mu = (e/kT)w\delta^2$, where e is the charge, w the hopping rate, and δ the distance between base pairs (3.4 Å).⁵⁴ This value is distinctly smaller than values of μ for discotic liquid crystals of planar aromatics such as triphenylene, which has a value of $\mu \approx 0.1 \text{ cm}^2 \text{ V}^{-1} \text{ s}^{-1}$.^{55, 56} This value is also smaller than the values calculated for hypothetical poly(dG)–poly(dC) oligomers, even when corrected for static disorder.⁵⁷ Both static and dynamic disorders are expected to reduce A-tract hole mobility.^{48, 57} Basko and Conwell have considered the effects of solvent and counterions on hole mobility in DNA.⁵⁸ Their value of $t = 0.65 \text{ ns}$ calculated through Debye–Hückel screening by counterions is consistent with our estimate of the effective hole-transport rate per base pair.

2.3.5 Efficiency of charge separation

The quantum yields Φ_1 in Table 2.8 show the relative efficiency of charge separation to **Sd**. The values of Φ_1 decrease rapidly for **2-4** and are more constant for **4-7**. The rapid decrease for **2-4** is related to the competition between forward hole migration which leads to hole arrival and backward hole migration which leads to reformation of **Sa*** in case **3** and **4**. Also the relative fast charge recombination from **Sa⁻/Sd⁺** also may contribute to the decreased Φ_1 . When **Sa** and **Sd** are separated by 4 bps or more, the charge recombination rate k_{cr} of **Sa⁻/Sd⁺** (see section 2.3.7) is much smaller than charge separation rate k_a , and thus does not significantly affect the efficiency of hole trapping (Φ_1), and Φ_1 is mainly dependent on charge return from **Sa⁻-A⁺** to **Sa*** or the charge recombination from **Sa⁻-A⁺** to ground **Sa**. (Figure 2.19a) Therefore values of Φ_1 for **4-7** are relatively constant. Noticeably, the values of Φ_1 for **4-7** are larger than those reported by Takada et al⁵³ for consecutive A-hopping in a different donor-acceptor pair. Our results indicate that charge migration in longer A-tract is feasible, however the low hole mobility may cause overall low hole-trapping efficiencies in longer A tracts.

2.3.6 Charge recombination

Charge recombination process refers to the process leading from the fully charge separated state **Sa⁻/Sd⁺** to ground state. The observation of similar first-order rate constants for decay of both the **Sd⁺** and **Sa⁻** transient absorption bands after the ratio of 525/575-nm bands has reached its maximum value provides evidence for decay of the charge separated state via charge

recombination. Rate constants for charge recombination (k_{cr}) are summarized in Table 2.9.

Their distance dependence is shown in Figure 2.20. The longer time constant for charge recombination versus charge separation in **1** is consistent with the large energy gap for charge recombination, which is responsible for Marcus inverted kinetics.¹² The values for k_{cr} decrease from $1.0 \times 10^{11} \text{ s}^{-1}$ for **1** to $1.4 \times 10^3 \text{ s}^{-1}$ for **7** (Table 2.9), a dynamic range of nearly 10^8 ! The values of k_{cr} for **1-4** provide a value of $\beta = 0.97 \text{ \AA}^{-1}$, similar to that reported for **Sa/G** systems.¹¹ The values of k_{cr} for **5-7** display a weaker distance dependence with a value of $\beta = 0.42 \text{ \AA}^{-1}$.

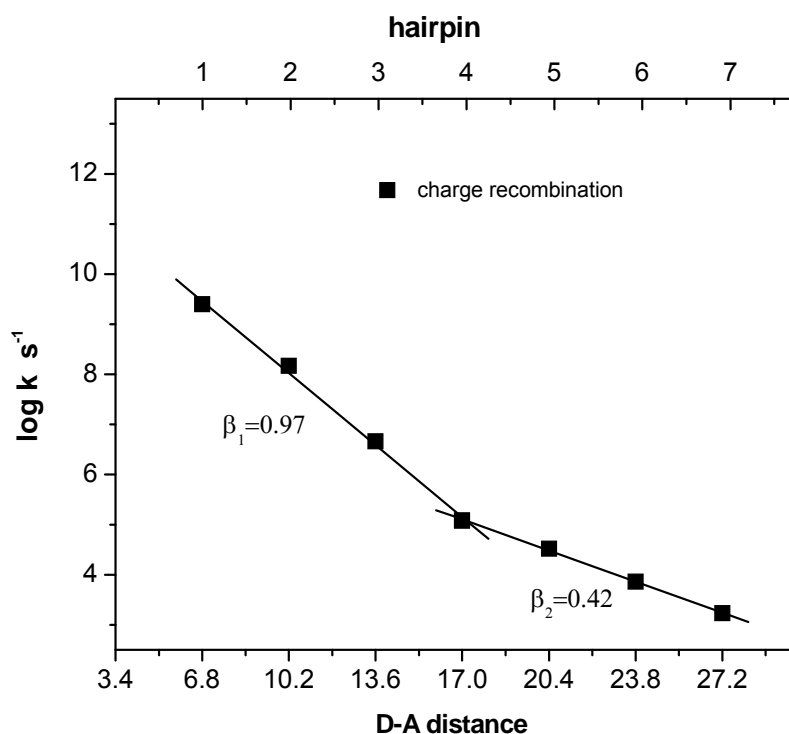


Figure 2.20 Distance dependence of the rate constants for charge recombination (data from Table 2.9).

The values of $\beta \approx 1.0 \text{ \AA}^{-1}$ for charge recombination in **1-4** and **Sa/G** systems are similar to that for charge separation in donor-bridge-acceptor systems with protein β -sheet bridges, which undergo electron transfer via a single-step superexchange mechanism.⁵⁹ The value of $\beta \approx 0.4 \text{ \AA}^{-1}$ for charge recombination in **5-7** is similar to the values reported by Shafirovich et al.⁶⁰⁻⁶² for hole transport from aminopurine cation radical to guanine and by Takada et al. for naphthaldiimide/phenothiazine systems separated by 4-8 A:T base pairs.³⁶ The smaller slope may reflect an increasing contribution of multistep hole hopping to the charge recombination dynamics at longer distances.⁶³ If so, the onset of crossover occurs at much larger value of R_{DA} (five intervening base pairs or ca. 20 \AA) than is the case for charge separation. Abdel Malak et al. have recently reported a crossover in mechanism for electron transfer across helical poly(proline) bridges from superexchange ($\beta = 1.4 \text{ \AA}^{-1}$) to hopping ($\beta = 0.18 \text{ \AA}^{-1}$) that occurs at a donor-acceptor edge-to-edge distance of ca. 20 \AA .⁶⁴

The occurrence of crossover from superexchange to hole hopping at a longer distance for charge recombination than for charge separation is a consequence of donor-bridge acceptor energetics. Whereas reversible hole injection is approximately isoergonic, hole trapping by **Sd** is estimated to be exergonic by ca. 0.5 eV (Figure 2.19a). Paulson et al. have recently reported that rate constants for superexchange are only weakly dependent upon the free energy for electron transfer, whereas rate constants for hopping are strongly dependent upon the free energy change.⁶⁵ Thus, superexchange will dominate at short distances when ΔG_{et} is large, as it is for charge recombination in **2-4**.

2.3.7 Electron transfer mechanism in other hairpin systems

The observation of charge separation via a multistep hole hopping mechanism for **Sa/Sd** hairpin systems possessing three or more A:T base pairs suggested that charge separation in **Sa/G** systems with three or more A:T base pairs also occurs via hole hopping rather than superexchange. This hole hopping mechanism can also readily explain the observation of similar rate constants for charge separation in Sa-linked hairpins possessing **Sd**, G, GG, GGG and Z as hole trap respectively with intervening A:T base pairs as bridge.^{66, 67}

However, different singlet acceptors could alter the competition between superexchange mechanism and hole hopping mechanism, when the singlet acceptor and donor guanine are separated by A:T base pairs. The mechanism of electron transfer process has been reinvestigated in the hairpin with different linkers (Figure 2.21). The free energy data of comparison charge transfer processes between different acceptor linkers and guanine are summarized in Table 2.10. For weaker electron acceptor **Pa**, the hole injection is estimated to be endergonic by 0.25 eV, which indicates a superexchange mechanism will be likely adopted. This is consistent with the observation of distance dependence of singlet quenching of **Pa*** by Z separated by 1-3 A:T base pairs, providing a β value of 1.1 \AA^{-1} .^{12, 68} For stronger electron acceptor diphenylacetylene dicarboxamide **Dpa**, an exergonic value of 0.1 eV is estimated for hole injection to adjacent adenine, which indicates a hole hopping mechanism. The previous observation of rate constants of formation of **Dpa^{•-}** which are independent of the presence of guanine, in which Dpa and guanine are separated by 1-5 A:T base pairs, is consistent with a hole hopping mechanism.⁶⁹

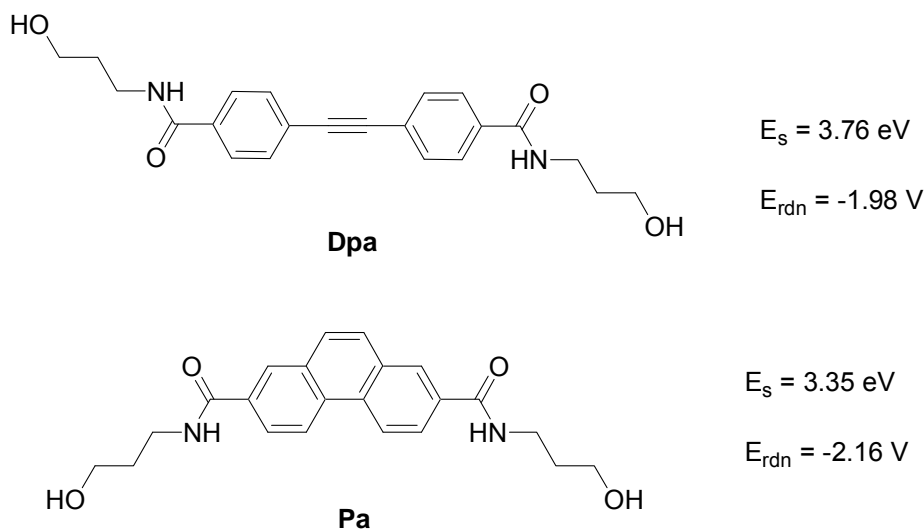


Figure 2.21 Structures, singlet energies, and reduction potentials of linker **Dpa** and **Pa**. Singlet energy data in methanol solution from Ref¹². Reduction potential in DMSO solution vs SCE.¹²

Table 2.10 Free energy comparison of the charge transfer processes between different acceptor linkers and guanine.

Singlet acceptor	ΔG^a	ΔG_i^b
Sa	-0.2 eV	0 eV ^c
Pa	0.05	0.25 eV ^c
Dpa	-0.54	- 0.1 eV

^a The free energy difference when G services as an electron donor, data calculated from Weller equation. ^bThe free energy difference of hole injection to adjacent base A, i.e. A is treated as the electron donor. ^c Data estimated by applying 0.2 eV to the ΔG^a , since the free energy difference is ca. 0.2 eV between G and A. See discussion section 2.3.4.

The behavior of the **Pa/Z** and **Dpa/G** systems provides examples of superexchange and hopping mechanisms, respectively, whereas the **Sa/Sd** system exhibits crossover between these two limiting mechanisms. Another likely example of crossover is provided by the results of Wan et al. for photoinduced electron transfer in systems possessing an aminopurine (**Ap**) acceptor and guanine donor separated by several A:T base pairs.²¹ An increase in **Ap*** lifetime with increasing **Ap/G** separation is attributed to competing superexchange quenching by G and A, but also could result from reversible hole injection followed by distance-dependent charge trapping by G.

2.4 Conclusion

Using multiple spectroscopic techniques, the kinetics of charge separation and charge recombination have been studied for photoinduced electron transfer in DNA. The crossover of from superexchange mechanism to hole hopping mechanism has been observed for the first time. In short bridge distance ($R \approx 10 \text{ \AA}$), superexchange mechanism is adopted, while when the number of intervening base pairs is three or more, the hole hopping mechanism is dominant. The hole hopping mechanism includes hole injection, hole transport or migration in an A-tract, and hole trapping by donor. The charge separation, and charge recombination processes are distance dependent, whereas the hole injection process is independent of donor-acceptor distance, but dependent upon its energetics. Hole migration rates estimated from hole arrival times indicate a low hole mobility in DNA A-tracts. The relatively low hole mobility and rapid charge return in

the **Sa/Sd** system result in low hole-trapping efficiencies in longer A-tracts.

Chapter 3

Thermal stability studies of oligo(ethylene glycol) hairpins

3.1 Introduction

The study of DNA A-tracts (poly(dA) sequences) and their unique structural properties began more than 20 years with the initial investigations of kinetoplast DNA from *Leishmania tarentolae*, which was observed to migrate anomalously on a gel relative to linear DNA.^{1,2} The single strand poly(dA) and the poly(dA):poly(dT) duplex have shown unusual structure properties, the former tending to π -stacking³ while the latter preferring distinct curvature.⁴ Oxidation of A-tracts results in the formation of delocalized excitons which are responsible for rapid and efficient hole transport in DNA.⁵ The electronic excited states of A-tracts have recently attracted considerable attention because of their ability to form relatively long-lived excimers or excitons.⁶ Very recently Fiebig et al. have found that in single strand poly(dA) sequences, the energy absorbed by adenine can be delocalized to minimize the excess energy.⁷ However studies of short poly(dA):poly(dT) duplexes is prohibited due to their poor stability. A minimum of ten to twelve A-T base pairs is required for the formation of a stable duplex under physiological conditions.⁸

In addition to the intense interest in A-tracts, thymine-thymine dimerization under UV exposition leads to various biological consequences, including apoptosis, immune suppression and carcinogenesis.⁹ This ultrafast photoreaction has been studied by Schreier et al.¹⁰, and they have found that the low quantum yields in single (dT)₁₈ strand and double strands containing 18 A:T base pairs are related to the local conformation before light absorption and photodamage. The study of photodimerization in long poly(T) sequences is complicated by the diverse

photoinduced dimerization products. However the investigation of the T-T dimerization in short poly(dT) regions is prevented by the low stability of short duplex-DNA.

DNA hairpins can provide relatively stable B-form DNAs with short poly(dA):poly(dT) domains. Lewis et al. have previously reported that mini-hairpins (Figure 3.1) possessing as few as three A-T base pairs and as two G-C base pairs with stilbenediether as the linker are stable at room temperature.¹¹

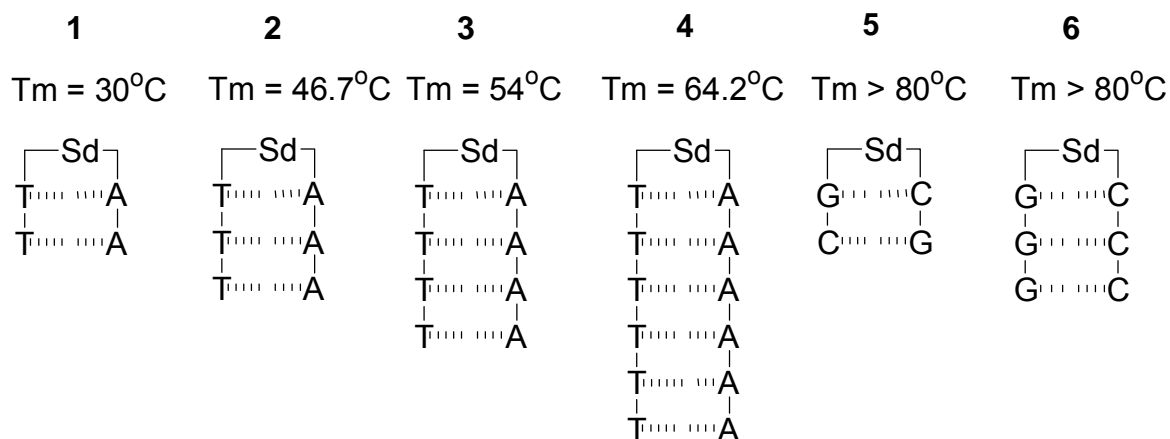


Figure 3.1 Structures and melting temperatures (T_m) of mini-stilbene hairpins.¹¹ Values for 2×10^{-6} M conjugates in standard buffer (10 mM sodium phosphate, pH 7.2) containing 0.1 M NaCl.

However the stilbenediether linker has UV absorption in the base pair region, which will affect the efficiency of absorption of base pairs, for example by adenine or thymine in studies of either T-T dimerization or excited state of A-tract exciton formation. Therefore it is necessary to construct a new type of mini hairpin with non-chromophoric linkers. The synthesis and

properties of hairpin-forming DNA conjugates having poly ethyleneglycol linkers connecting base pair domains consisting of a mixture of A-T and G-C base pairs has been reported by Durand et al.¹² and by Rumney and Kool.¹³ The latter workers investigated the stability of the hairpins 5'-dCGAACG-EG_n-CGTTCG having six base pairs and linkers consisting of 3-8 ethylene glycol units (Figure 3.2 and Table 3.1). Presumably the lower T_m value for the **EG3** linker reflects its inability to span the bridging distance of ca. 15 Å between base-paired nucleotides without distortion of the normal B-DNA geometry; however the nature of the distortion was not determined.

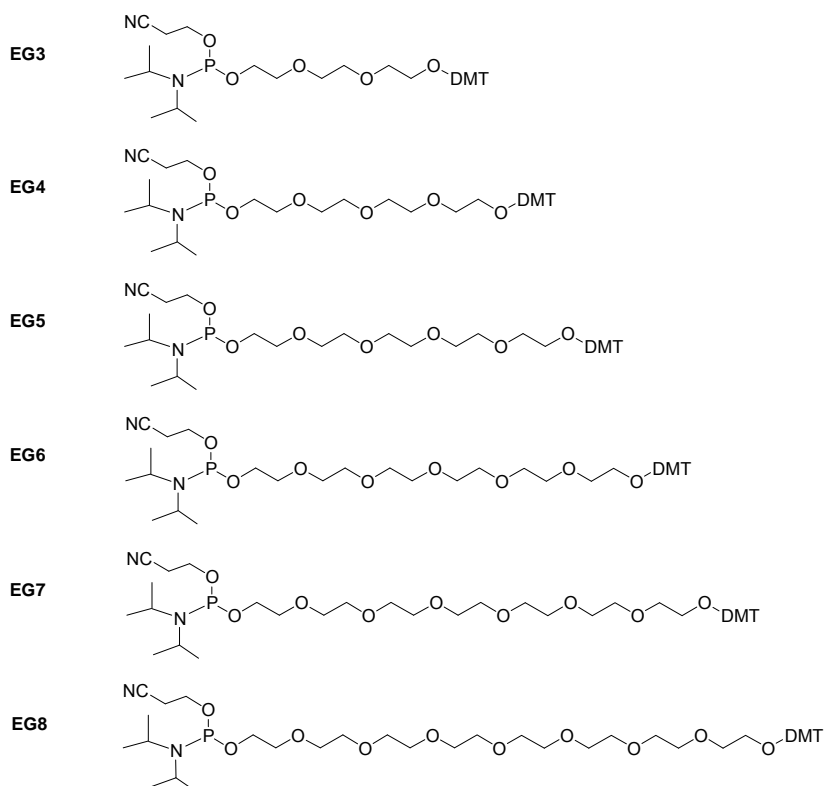


Figure 3.2 Structures of poly(ethylene glycol) linkers with protecting and activating groups.¹³

Table 3.1 Melting temperature (T_m) and free energies ($-\Delta G$ (37 °C)) for duplex hairpins bridged by oligo(ethylene glycol) (EG) loops and by a natural T4 loop at pH 7.0. Data from ref¹³.

Duplex hairpins	T_m ^{a, b} (°C)	$-\Delta G$ (37 °C) ^{a, b} (Kcal/mol)
5' CGAACG 3' GCTTGC EG3	62.5	3.4
5' CGAACG 3' GCTTGC EG4	66.4	4.0
5' CGAACG 3' GCTTGC EG5	71.1	4.6
5' CGAACG 3' GCTTGC EG6	72.9	4.9
5' CGAACG 3' GCTTGC EG7	74.9	3.9
5' CGAACG 3' GCTTGC EG8	73.8	3.7
5' CGAACG ^T T 3' GCTTGC _T T	67.8	4.6

^a Conditions: 2.0 mM total strand concentration, 100 mM NaCl, 10 mM MgCl₂, 10 mM mM NaPIPES buffer. ^b Error limits for individual measurements are estimated at ± 0.5 °C in T_m , and $\pm 10\%$ in free energy. Data shown are the averages from three measurements.

Data have shown that hairpins with **EG6** or **EG7** have the highest thermal stability and retain B-form structure. The absence of UV absorption by the ethylene groups in nucleobase region encouraged us to employ hairpins having a PEG scaffold for studies of the electronic excited states of short A-tracts and T-T dimerization. Therefore we have constructed mini-hairpins with short A-tracts possessing non-chromophore PEG linkers. Hairpins with **EG3** and **EG6** as linkers are shown in Figure 3.3. Thermal stabilities and structural properties of these newly designed hairpins have been investigated through electronic spectra, circular dichroism, thermal melting profile, and molecular dynamics simulations.

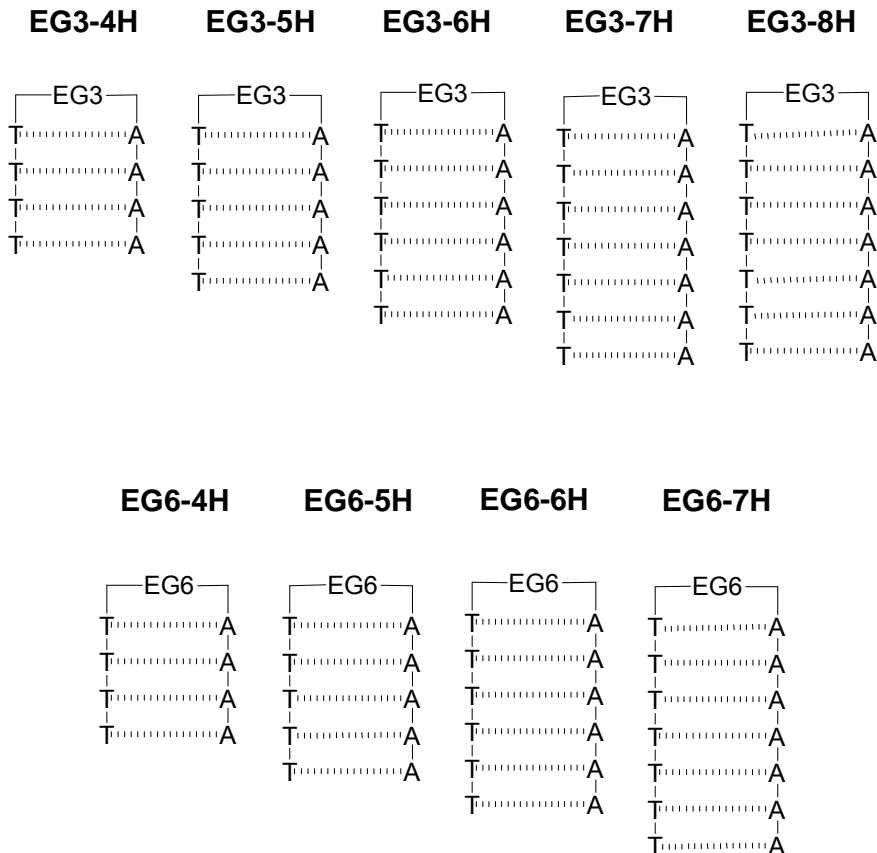


Figure 3.3 Structures of **EG3**-hairpins, and **EG6**-hairpins.

3.2 Results

3.2.1 Synthesis of EG-linked hairpins

The conjugates designed in Figure 3.3 are prepared by means of conventional phosphoramidite chemistry.¹⁴ They are purified by HPLC and characterized by UV and by MALDI-TOF mass spectrometry.

3.2.2 Electronic absorption and circular dichroism spectra

The UV absorption spectra of **EG6**-linked hairpins shown in Figure 3.4 consist of a single broad band having a maximum at 260 nm. No shift in the absorption maxima or change in band shape is observed upon increasing the number of A-T base pairs. **EG3**-linked hairpins are similar to these of **EG6**-linked hairpins.

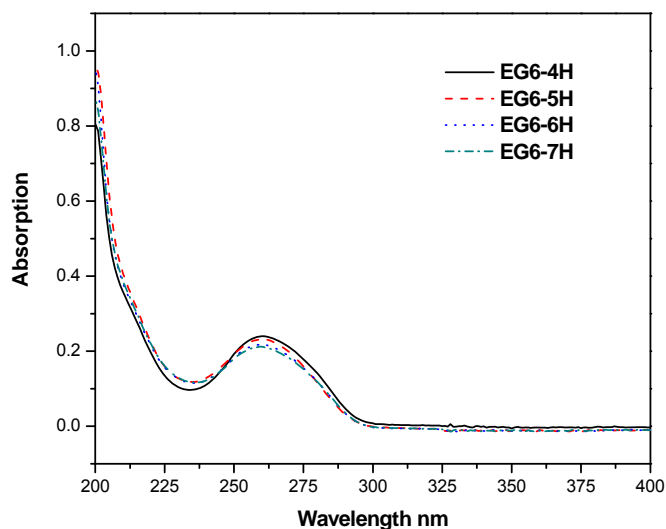


Figure 3.4. Normalized UV spectra of 5 μM **EG6**-linked hairpins in 0.1 M NaCl, 0.01 M phosphate buffer pH 7.2.

The thermal dissociation profiles for hairpins **EG3-nH** ($n=4-8$) and **EG6-nH** ($n=4-7$) are shown in Figure 3.5. **EG3-4H** and **EG6-4H** show poorly defined dissociation profiles, which are similar to that for single strand dA₉. Values of T_m obtained from the first derivatives of the thermal dissociation profiles for conjugates having well-defined melting transitions are reported in Table 3.2.

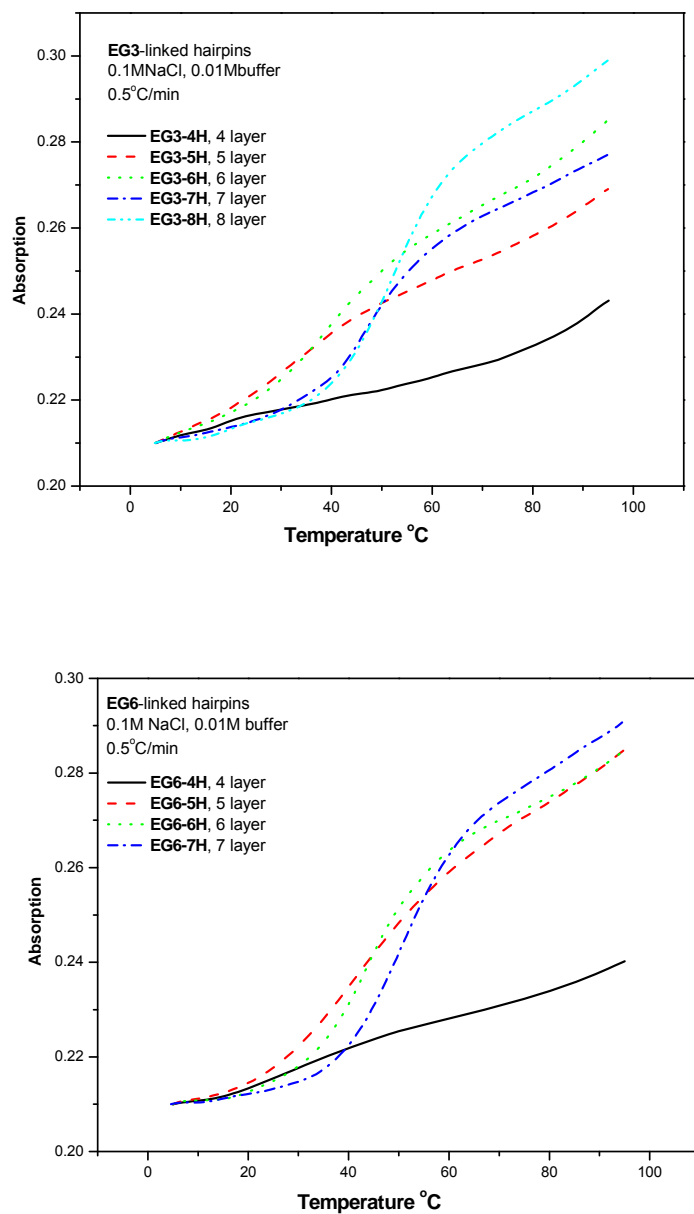


Figure 3.5 Dissociation profiles for **EG3-nH** (n=4-8) (top) and for **EG6-nH** (n=4-7) (bottom) determined at 260 nm (5 μ M conjugate, 10 mM sodium phosphate buffer, 0.1 M NaCl).

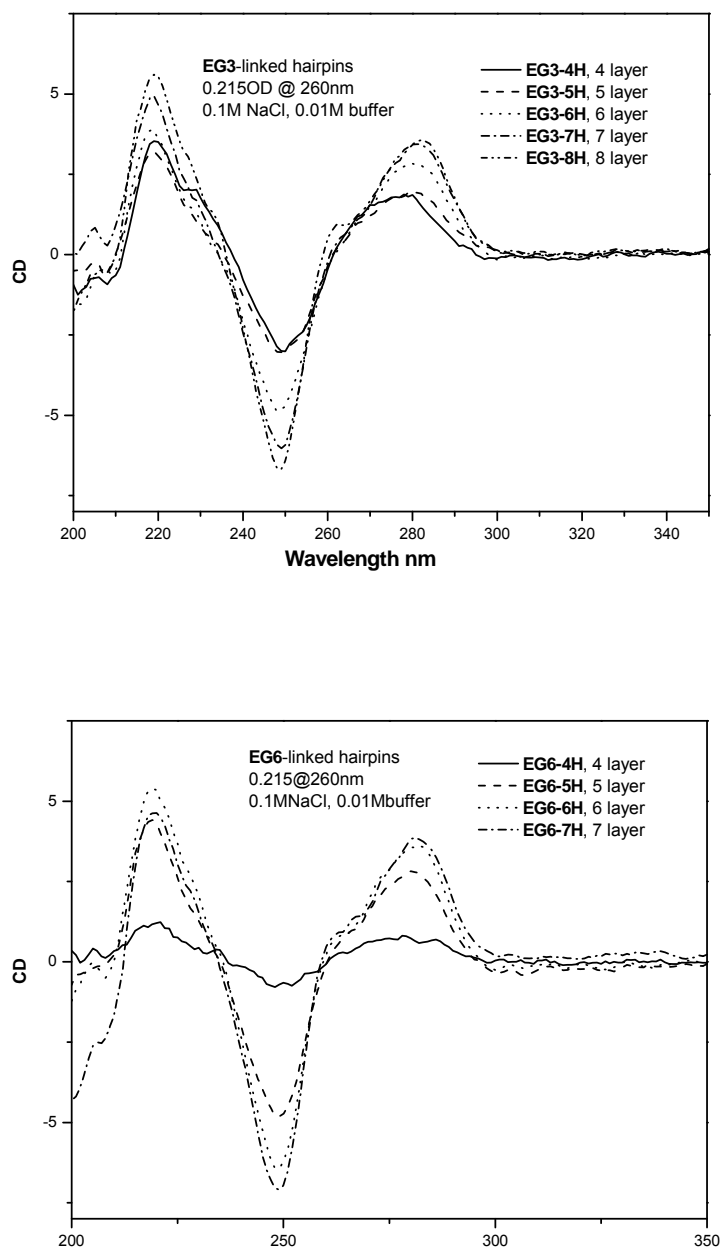


Figure 3.6 CD spectra of hairpins **EG3-nH** (top) and **EG6-nH** (bottom) (5 μ M conjugate, 10 mM sodium phosphate buffer, 0.1 M NaCl).

The CD spectra of the **EG**-linked hairpins are shown in Figure 3.6. The CD maxima and minima of the shortest and longest conjugates occur at similar wavelengths. However, the CD spectrum of conjugates **EG6-4H** which has the shortest base-pair domains (4 A-T base pairs), is broader and weaker than those of the conjugates having longer base-pair domains, even relatively weaker than that of **EG3-4H**.

3.2.3 Molecular dynamics simulations

Molecular dynamics simulations were performed by Martin McCullagh. The hairpins having six A-T base pairs were minimized and equilibrated using the AMBER force field, as previously described for capped hairpin structures having stilbenedicarboxamide linkers.^{15, 16} The Amber 8.0 program was used to run molecular dynamics simulations in an explicit water solution. The total simulation time for each conjugate structure was 3.0 ns with a time step length of 2 fs. Except in the case of the **EG3-6H**, the mass-weighted root mean square deviations (RMSd) do not have large fluctuations with respect to the MD-averaged structure after 1 ns, indicating that the simulations have reached equilibrium.

Structures for hairpins **EG3-6H** and **EG6-6H** obtained by averaging the coordinates of their 2 ns production run followed by a minimization of these coordinates are shown in Figure 3.7. These structures represent local minima arrived at from idealized B-DNA input structures and may not represent global minima or averaged structures. All of the conjugates having **EG6** linkers adopt B-DNA structures with normal base paired geometries and the all of the ethylene

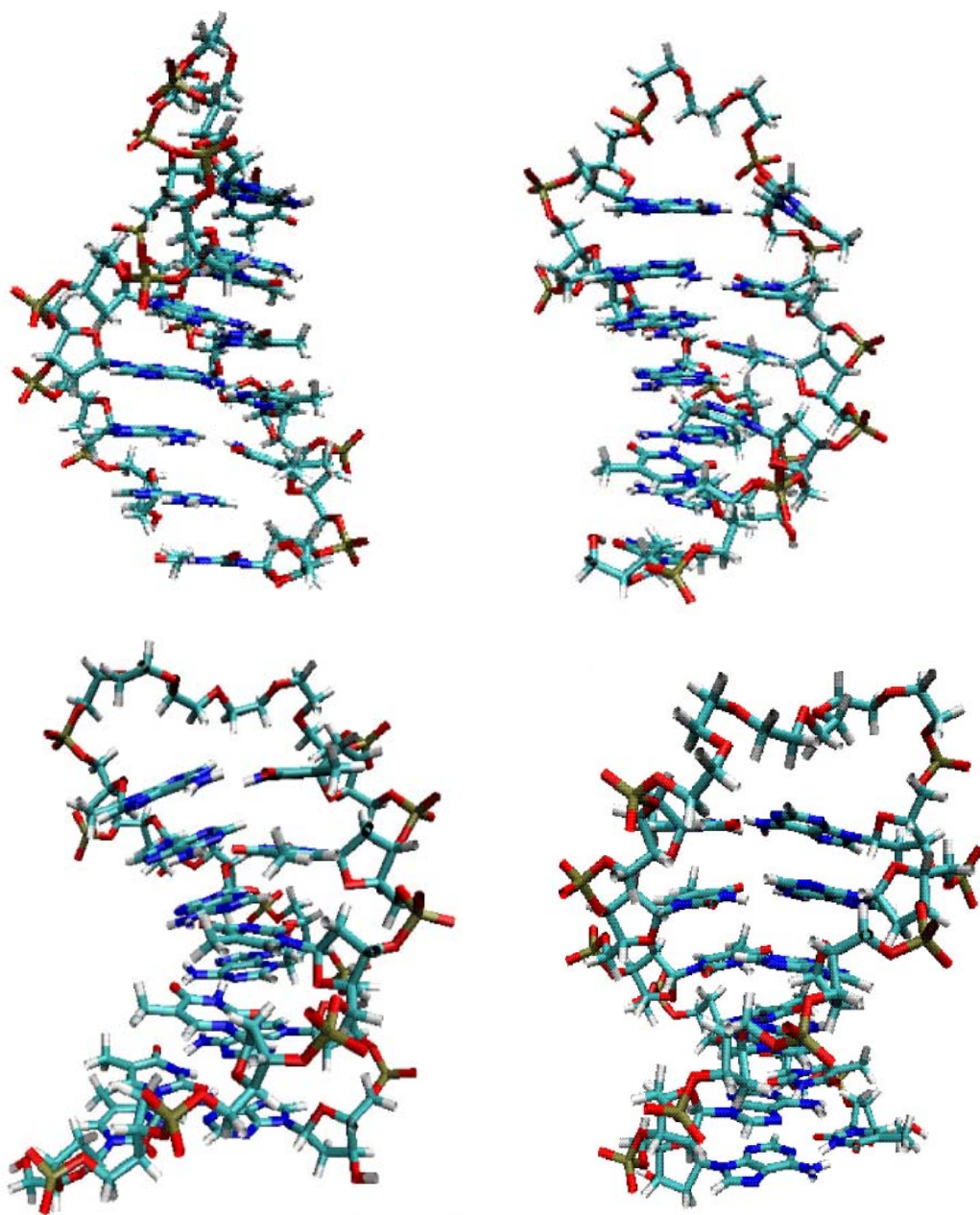


Figure 3.7. Minimized structures obtained from molecular dynamics simulations for **EG3-6H** (top two), and **EG6-6H** (bottom two).

glycol units in the linkers adopt low energy gauche conformations. The average P-P distance for the two **EG6** linkers is ca. 16 Å, slightly shorter than the 18 Å average P-P distance in the base-pair domain.

In contrast to the base-paired structures of the conjugate having **EG6** linkers, the geometries of the base pairs adjacent to the **EG3** linkers are severely distorted. The three ethylene glycol units in **EG3-6H** adopt gauche conformations as well, even though this results in a shorter P-P distance than would be attained with anti conformations. In the minimized average structure of **EG3-6H** (Figure 3.7) the thymine adjacent to the linker (BP1) is flipped out, and the terminal base pair (BP6) adopts a stacked conformation. Notably, the adjacent base pair (BP5) of terminal base pair (BP6) is bent. During the simulation, the trajectory of BP1 fluctuates between paired and flipped out conformations several times, while BP6 is converted to the stacked structure after ca. 0.5 ns and remains in this conformation for the duration of the trajectory. These differences have also been shown in the time dependent base pairing changes in the A-T O--HN hydrogen bonding distance for BP1 and BP6, shown in Figure 3.8a. As a consequence of the unusual geometries for BP1 and BP6, the distribution of distances between the base-pair center of mass for the BP1 is longer than those for BP2-5 and the base-pair center of mass is shortest for BP6 (Figure 3.8b). For **EG6-6H**, hydrogen bonding distances for BP1 and BP6 remain constant (Figure 3.9).

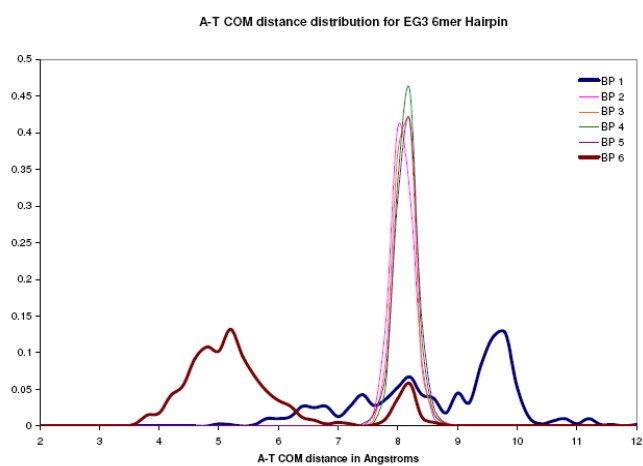
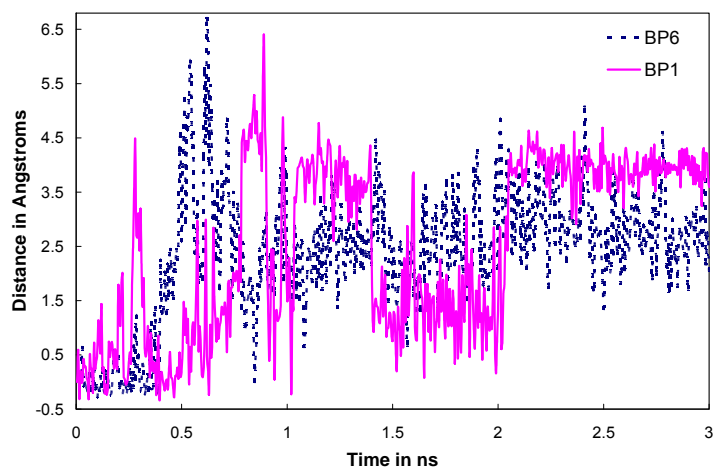


Figure 3.8 a, top) Time dependent deviation in the O--HN distance for A-T base pairs BP1 (adjacent to the linker) and BP6 in hairpin **EG3-6H**. b, bottom), A-T distance distribution for each BP in EG3-6H.

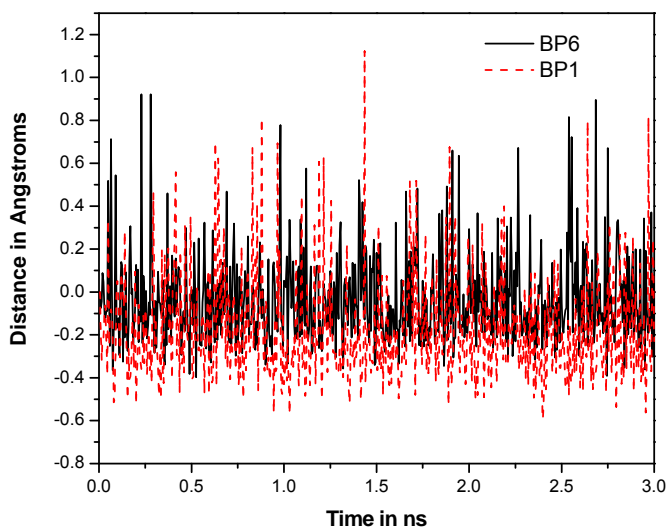


Figure 3.9 Time dependent deviation in the O--HN distance for A-T base pairs BP1 (adjacent to the linker) and BP6 (terminal base pair) for hairpin **EG6-6H**.

3.3 Discussion

3.3.1 Thermal stability of EG-linked hairpins

The melting temperatures and thermodynamics data of **EG**-linked hairpins with well defined melting profiles are summarized in Table 3.2. Thermodynamics data obtained by the method of Breslauer.¹⁷ The melting values **EG3-4H** and **EG6-4H** are not obtained because of their broad melting profiles.

Table 3.2. Melting temperatures and thermodynamics data of formation of hairpins having **EG3** and **EG6** linkers.^a

Number of base pairs	T_m^b	T_m^c	ΔH	ΔS^c	ΔG^{0c}
EG3-4H	N/A ^d				
EG3-5H	33	34	-31.39	-102.2	-0.935
EG3-6H	39	39.1	-35.45	-113.5	-1.62
EG3-7H	46	46.1	-42.16	-132.1	-2.81
EG3-8H	53	50.9	-42.50	-131.1	-3.42
EG6-4H	N/A ^d				
EG6-5H	40	38	-25.65	-82.5	-1.08
EG6-6H	44	43	-36.16	-114.4	-2.08
EG6-7H	50	48.6	-36.96	-114.9	-2.73

^a Data for 5 μ M conjugates in 0.1 M NaCl, 10 mM sodium phosphate buffer, pH = 7.2. Units description: T_m : $^{\circ}$ C, ΔH : Kcal/mol, ΔS : cal/mol/K, ΔG : Kcal/mol. ^b T_m values obtained by UV-melting dissociation with a heating rate of 0.5 $^{\circ}$ C/min. ^c Data obtained by Breslauer methods manually. ^d Data not available.

In comparison to hairpins with a natural “ACC” loop (Figure 3.10), **EG3**-linked hairpins are slightly more stable, while **EG6**-linked hairpins are much more. **EG6**-linked hairpins are more stable than **EG3**-linked hairpins, which is consistent with the observation in work of Durand^{12, 13} and Rumney¹³ with hairpins having a mixture of A-T and G-C base pairs. This difference in stability could be related to the distance difference of **EG3** linker **EG6** linkers. The former is shorter than the average O-O distance of the duplex, while the latter is sufficient to cover that distance. The relative short length of **EG3** linker could cause the distortion of the neighboring base pairs. This distortion is observed in our molecular dynamics simulations of the **EG3-6H** hairpin. In Figure 3.7, the BP1 of hairpin **EG3-6H** shows poor base pairing between A and T as a consequence of the strain resulting from the short linker distance. This poor base pairing causes fluctuations in the time dependent distance observed for H-bonding as well (Figure 3.8a). However for hairpin **EG6-6H**, the H-bonding of BP1 is well established (Figure 3.7 and 3.9) during the simulation period.

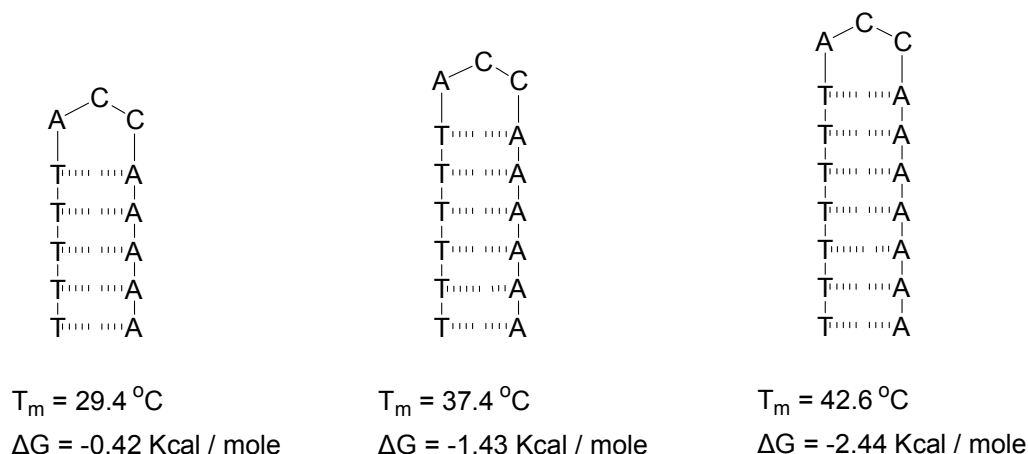


Figure 3.10 Hairpins with natural ACC loop. Melting temperatures and free energy data of each hairpin are calculated using idt's oligo analyzer version 3.0.¹⁸ The concentration of the single strand is 0.25×10^{-6} M, in 0.1 M NaCl.

The T_m values of **EG**-linked hairpins are significantly lower than those of the stilbenediether linked poly(A)-poly(T) hairpins previously studied in our group.¹¹ Besides the suitable link length of stilbenediether (16.5 \AA), the hydrophobic and π -stacking interactions between the planar aromatic stilbene and the adjacent base pair result in the enhanced stability of the stilbene-linked hairpins. The stilbenediether linked hairpin having four A-T base pairs display a well-resolved melting transition, whereas neither **EG3-4H** nor **EG6-4H** do so (Figure 3.5). However, compared to non-chromophoric linked hairpins possessing dodecyl diether as the linker very recently designed in our group, EG6-linked hairpins show higher stabilities.

The melting temperatures obtained by fitting of the thermal dissociation profiles using wither Breslauer's method are similar to those obtained from the first derivatives of the experimental data. Thermodynamic data has been fitted via Meltwin program as well (Data not

shown), however, they show less favored free energy compared to data obtained via method of Breslauer. Most likely this is due to absence of well defined equilibrium states above and below the melting transition. Interestingly, there are continuous hyperchromism changes before and after dissociation of the **EG**-hairpins. Studies in our group has found no similar change for the dodecyl diether linked short poly(A)-poly(T) hairpins (ref to unpublished results of M. Haraiharan). This indicates that the pre-melting and post-melting in **EG**-hairpines might result from the nature of the loop linker.

3.3.2 Comparison of base pairs in **EG3**-hairpins and **EG6**-hairpins

With increasing numbers of base pairs of **EG**-linked hairpins, the CD rotational strength increases and the band widths decrease (Figure 3.6). The CD profiles of these hairpins show typical B-form DNA character similar to that of the anti-parallel hairpin $d(T_{10}C_4A_{10})$,¹⁹ which has maxima near 220 nm and 280 nm with a shoulder at 260 nm, and minimum near 250 nm.

The greater thermal stabilities of **EG6**-linked hairpins vs. **EG3**-linked hairpins are also reflected in the relatively stronger CD profiles of the former. In molecular dynamics simulations of **EG3**-linked hairpins, the fluxional nature of the base pair (BP1) adjacent to the linker and the terminal base pair (BP6) reduces the effective number of base pairs when compared to the hairpins with EG6 linker. Therefore the CD signal of **EG3**-linked hairpins are general weaker than that of EG6-linked hairpins, even though the stacking of the adenine from terminal base pair BP6 on the adjacent base pair BP5 might partially compensate for the decrease in Watson-Crick

base pairing.²⁰

Noticeably, the CD spectrum of **EG3-4H** is stronger than that for **EG6-4H** even though the UV melting profile is better defined for **EG6-4H**. Calculated structures for **EG3-6H** show that after the initial equilibrium process the terminal base pair (BP6) changes from a base paired geometry to a stacked geometry of A and T (Figure 3.7 and 3.8b). Generally, end-fraying is assumed to result from the breaking of base-base hydrogen bonds and reforming of base-water hydrogen bonds when the terminal base pair is exposed to the aqueous environment. The end fraying might further induce the dissociation of duplex.²¹ However, an alternative pathway for end fraying of base pairs which yields a stacked complex between terminal adenine and thymine has been simulated by Tinoco et al.²¹ End fraying has also been observed to improve the stacking overlaps in the interior of the short duplex d(CGTAG).²² Thus the backbone distortions caused by the short hairpin loop in **EG3-6H** may be relieved by end fraying in BP6. The molecular dynamics simulation for **EG3-6H** indicates that base pairs BP1 and BP6 dissociate and reform on the nanosecond time scale, considerably faster than the typical 1-5 ms lifetime of an AT base pair.²³ A recent investigation of ultrafast DNA dynamics placed a lower bound of 40 ns on terminal base pair dissociation time.²⁴ The faster time for **EG3-6H** most likely reflects its highly distorted structure and low thermodynamic stability.

3.4 Conclusion

The synthesis and structure of hairpins having non-nucleoside **EG** linkers with short A-T base pair domains has been explored. Conjugates possessing an **EG3** or **EG6** linkers and five or

more A-T base pairs form stable hairpin structures having well-resolved thermal dissociation profiles and CD spectra.

Molecular dynamics simulations indicate that the **EG6**-linked hairpins can adopt B-DNA base-paired structures. Hairpins possessing the shorter **EG3** linker are less stable, plausibly due to the strain inherent in the hairpin loop regions. Molecular dynamics simulations of **EG3-6H** reveal the occurrence of ultrafast disruption of the A-T base pairs of BP1 and BP6, the former undergoing reversible base flipping and the latter conversion from hydrogen bonded to π -stacked geometry.

The UV spectral band shapes and maxima of the hairpin conjugates are not sensitive to the number of base pairs or choice of linker. However, both the intensity and structure of the CD spectra increase with added A-T base pairs. The absence of UV chromophores makes the **EG6**-linker hairpin suitable for studies of the photochemical behavior of A-T base pair domains possessing four or more base pairs or the excited state of adenine in short A domains with conserved B-form DNA character. For the studies for even short A-tracts, dumbbell conjugates are potential candidates, if the synthesis is approachable.

Chapter 4

Excimer studies of formation of pyrene probed parallel quadruplexes

4.1 Introduction

In eukaryotic systems tandem repeats of guanine-rich sequences, termed telomeric sequences, such as *Oxytricha nova* [d(T₄G₄)], *tetrahymena thermophila* [d(T₂G₄)], and mammalian [d(T₂AG₃)], tend to be concentrated at the ends of chromosomes in a linear fashion.¹ The function of the telomere is to maintain chromosome integrity, avoiding end-to-end fusions and unwanted recombination events, and protecting the ends from chromosomal degradations and from being recognized as damaged DNA.² However due to the “end replication problem”, the length of the telomere gets shortened during cell divisions, causing cell apoptosis. Telomeres can be lengthened by an RNA-containing enzyme known as telomerase. However, telomerase is present in 80-85% of tumor cells, and essentially absent in most somatic cells.¹ This results in an unlimited lifetime for cancer cells. Studies have found the enzymatic activity of telomerase can be directly inhibited by formation of K⁺-stabilized G-quadruplex structures via self association of the G-motifs in telomeres.³ The functional relevance of quadruplex formation has been supported by the isolation of proteins that bind and promote the formation of quadruplex structures, such as transcription factors,⁴ nucleases,⁵ topoisomerase I,⁶ and helicases.⁷ Therefore, to understand the structural properties of G-quadruplexes is essential to obtain critical information covering the construction of stable G-quadruplexes as telomerase inhibitors.

G-quadruplexes can be assembled by stacking of G-quartets connected through Hoogsteen base pairing (Figure 4.1). Depending on the nature of the substrate sequences,

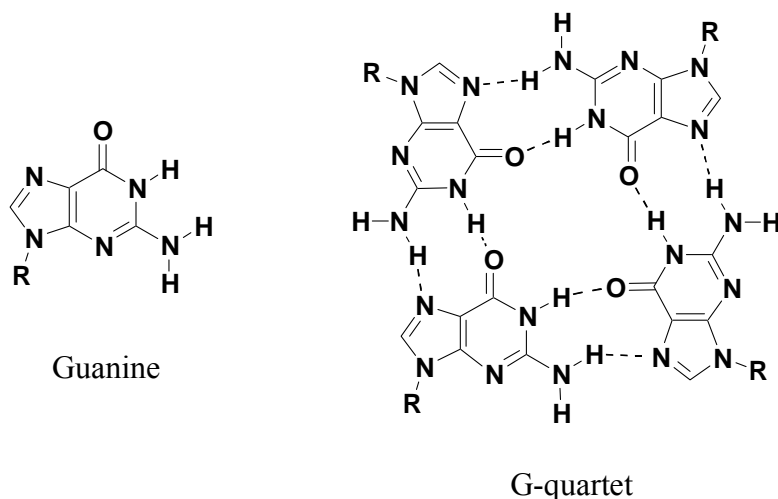


Figure 4.1 Structures of guanine monomer and G-quartet formed from four guanines via Hoogsteen base pairing.

G-quadruplexes can be associated by different means such as intramolecular folding of a single sequence possessing four G-rich domains, dimerization of sequences possessing two G-rich domains, or via intermolecular assemble of sequences possessing a single G-rich domain (Figure 4.2). In terms of the polarity of each strand forming the quadruplex, G-quadruplexes are defined having antiparallel or parallel structures (Figure 4.2). Although the biological relevance of structural polymorphism in telomere tails is not well understood, cytological studies indicate a direct involvement of the telomere domain in interchromosome association. Sen and Gilbert hypothesized that synapsis is facilitated by formation of parallel quadruplex structures at the telomeres, within guanine-rich motifs of the four homologous chromatids during meiosis as well.⁸ Similar association has been promoted by Meiosis-specific yeast Hop1 protein on double strand DNA.⁹

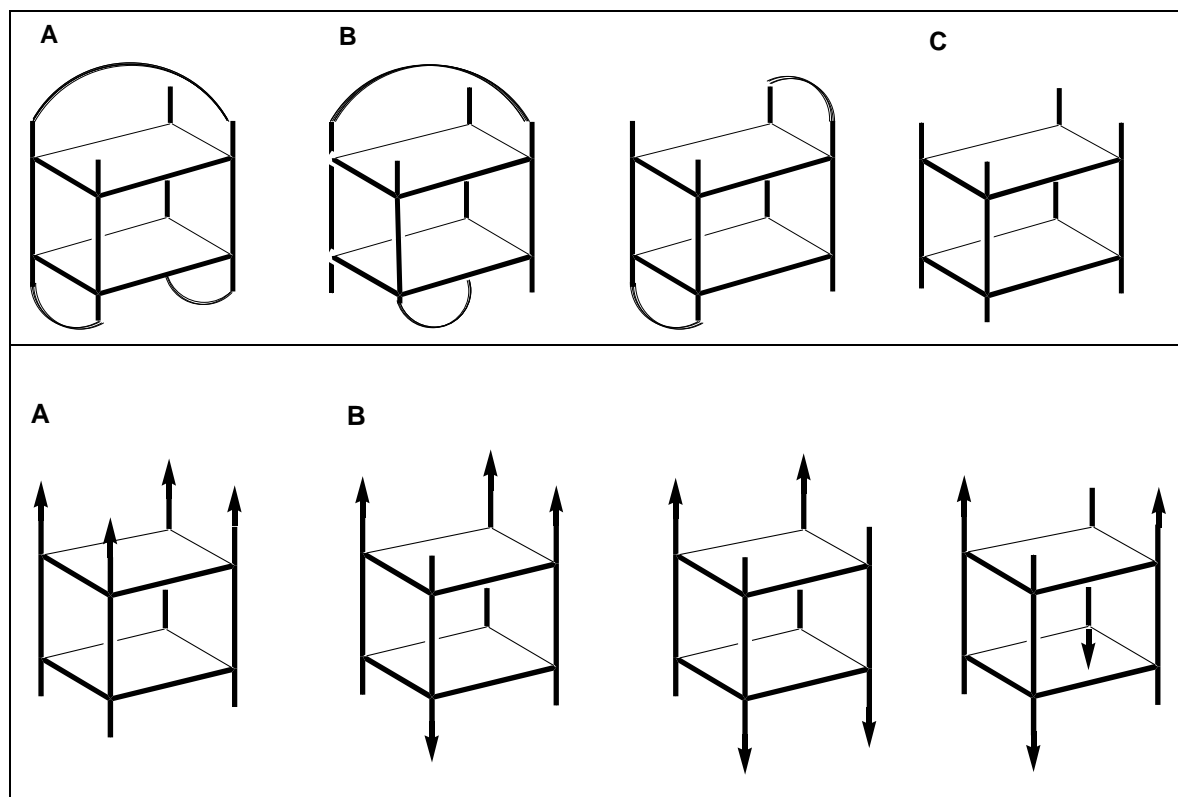


Figure 4.2. Polymorphism of Quadruplex structures. (Top), Various strand stoichiometries of G-quadruplex structures. A, a single sequence possessing four guanine rich motifs yields a unimolecular G-quadruplex. B, two strands with two guanine rich regions in each produce either diagonal, or edge to edge biomolecular G-quadruplex structures. C, Four separated strands intermolecular form a quadrimolecular G-quadruple structure. (Bottom), Different strand polarity arrangements of G-quadruplexes. A, all strand parallel. B, different types of antiparallel quadruplexes. Arrows indicate 5' → 3' polarity.

Fluorescence probes have been used widely in investigation biopolymer structure due to their unique spectroscopic properties. It has been observed that an increase in the concentration of fluorescent pyrene is accompanied by a decrease in the quantum yield of its fluorescence. This phenomena is due to the formation of excimer, which is a dimer of an electronically excited pyrene with a second pyrene in its ground electronic state¹⁰ (Figure 4.3). The excimer is associated in an electronic excited state and dissociative in its ground state. Once one molecule is in the excited state, the stabilized interaction becomes possible due to the half occupied HOMO and LUMO orbitals.¹¹ This results the relative minimum of the excimer on the excited-state potential energy surface, which exhibits usually a longer wavelength “excimer emission” band. This unique excimer fluorescence has been widely employed as a probe for the structure of biopolymers possessing covalently attached pyrene chromophores in aqueous solution, such as micelles or phospholipid membranes.¹⁰ Complementary oligonucleotides possessing pendent pyrene chromophores or pyrene-derived base surrogates in both strands display either monomer or excimer fluorescence, depending on the proximity of the pyrenes.¹²⁻¹⁵ Oligonucleotides possessing a single 5'- or 3'- terminal pyrene have been used to investigate the strand polarity (parallel vs. anti-parallel) of duplex and triplex structures.^{16, 17} Recently, pyrene excimer emission has been observed when two pyrenes are incorporated at both ends of the thrombin-binding aptamer, d(GGTTGGTGTGGTTGG), due to the formation of a chair-type quadruplex structure in the presence of potassium ions.¹⁸

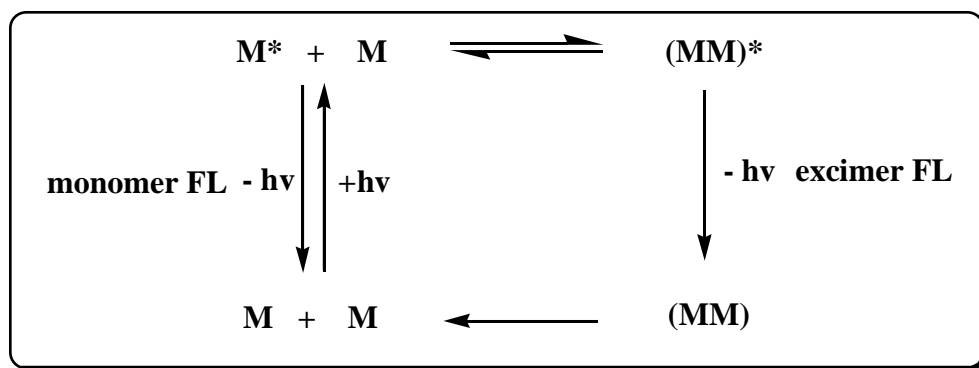


Figure 4.3 Illustration of monomer and excimer emission fluorescence.

However, pyrene has not been used to study the formation of intermolecular quadruplexes. Therefore, we incorporated a pyrenebutanol fluorescent probe at the 5'-end of short poly(G) sequences (Figure 4.4) to study the formation of quadruplex structures. We have found that whereas the single strand oligonucleotides **Py1-Py4** display monomer fluorescence, the quadruplex structures display a mixture of monomer and excimer fluorescence, both of which are assigned to parallel quadruplex structures. This leads to the conclusion that the appearance of excimer / monomer fluorescence can be used as a probe for parallel G-quadruplex formation. Studies also show that the ratio of excimer/monomer intensity is dependent upon both temperature and salt concentration. Enhanced excimer fluorescence at high salt concentrations is due to a hydrophobic salt effect on the pyrene chromophores.

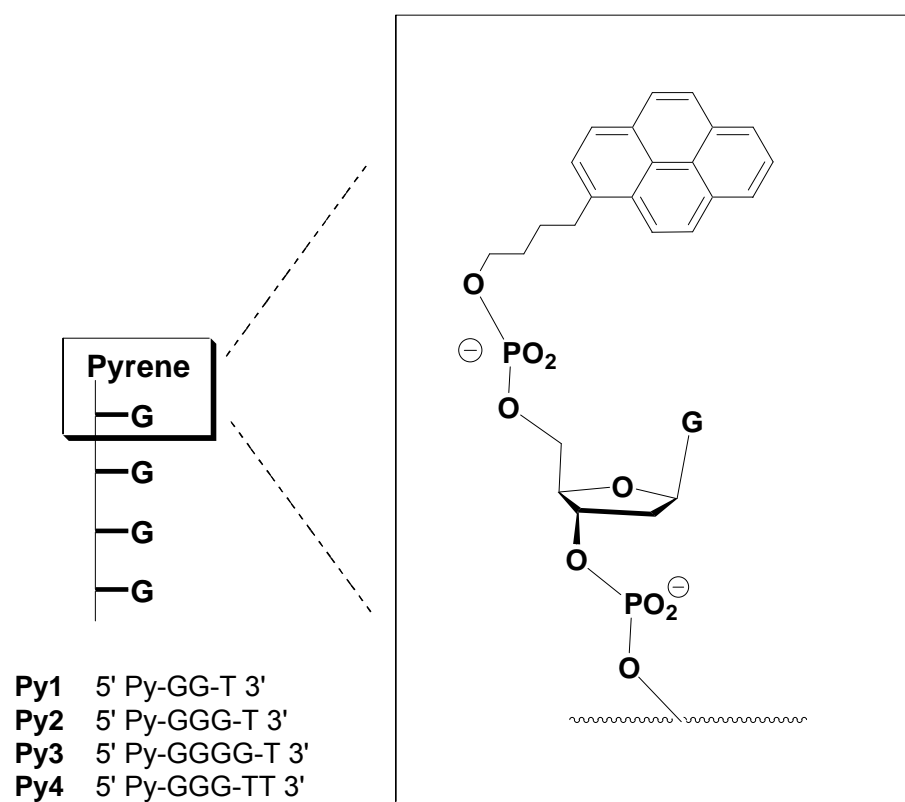


Figure 4.4 Designed sequences with pyrenebutanol attached at 5'-end of short poly(G) oligonucleotides.

4.2 Results

1-Pyrenebutanol has been selected for 5' probe over pyrenemethanol due to the fail of incorporating phosphoramidite of pyrenemethanol via either in solid or solution phase synthesis. 1-Pyrenebutanol was converted to its phosphoramidite by reaction with 2-cyanoethyl diisopropyl chlorophosphoramidite in tetrahydrofuran in the presence of diisopropylethylamine as described in Experimental section 6.3.3. The conjugates **Py1-Py3** were prepared by means of conventional phosphoramidite chemistry and purified via RP-HPLC. Molecular weights were determined by means of MALDI-TOF mass spectrometry. Due to the tendency of aggregation of G-rich sequences, samples were stored in ddH₂O at 4°C.

4.2.1 Electronic spectra

The UV spectra of pyrenebutanol in methanol and conjugate **Py2** in aqueous buffer with 0.1 M KCl are shown in Figure 4.5. The spectrum of **Py2** in water is similar to that obtained in buffer. The long-wavelength π - π^* band of pyrenebutanol is red-shift and broadened in the spectrum of conjugate **Py2**. The short-wavelength bands of the conjugate are the sum of the absorption of the bases and pyrene. Similar spectra have been observed for conjugates **Py1**, **Py3**, and **Py4**, except that they differ in the ratio of the band intensities.

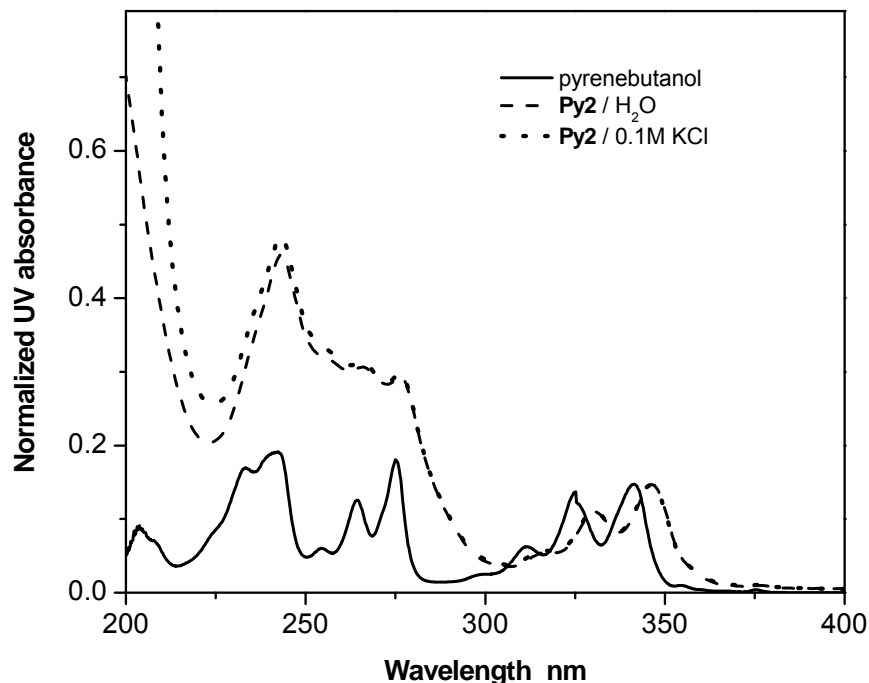


Figure 4.5 Absorption spectra of the pyrenebutanol in methanol solution and the pyrenebutanol conjugate **Py2** in water and in aqueous 0.1 M KCl, 10 mM potassium phosphate.

4.2.2 CD spectra

The CD spectra of **Py1-Py3** in water and in 0.01 M phosphate buffer with 0.1 M KCl at room temperature are shown in Figure 4.6. No CD peaks are observed for **Py1**, either with or without KCl, at room temperature or at 5°C. The CD spectrum of **Py2** in water is weaker than it is with salt. However, the CD spectrum of **Py3** is similar with or without added KCl. Besides the observation of a positive peak at 265 nm and a negative peak at 240 nm, characteristic peaks for parallel G-quadruplexes, for **Py2** and **Py3**, additional peaks are observed at long wavelength, which have vibrational structure similar to that of pyrene UV absorption.

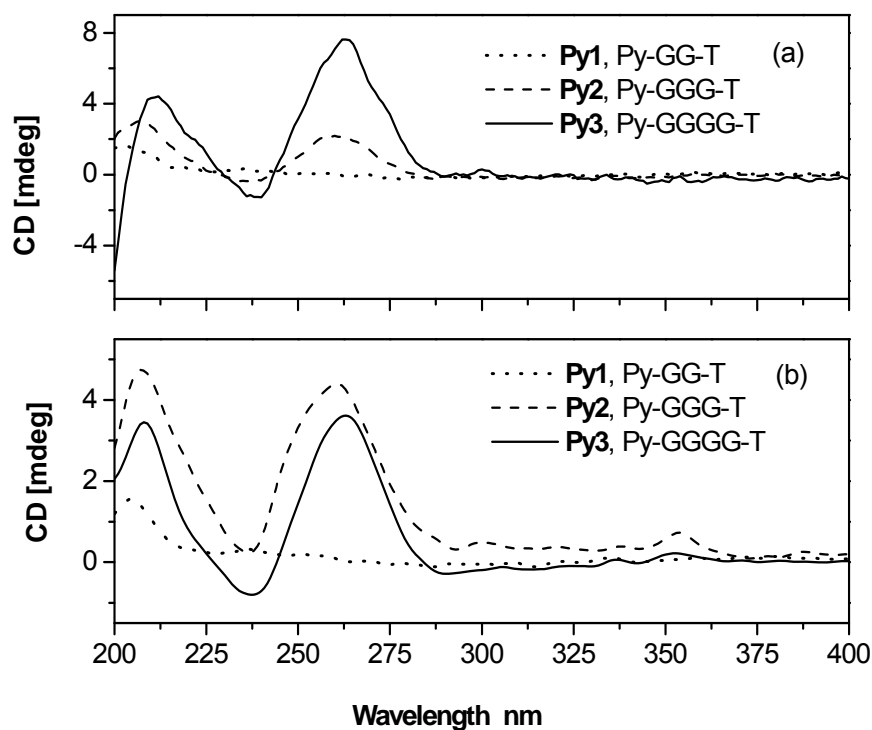


Figure 4.6 Circular dichroism spectra of 1×10^{-6} M conjugates **Py1-Py3** (a) in water; (b) in 0.1 M KCl, 10 mM potassium phosphate.

The intensity of the pyrene CD band for **Py2** increases as the salt concentration is increased from 0.1 to 0.5 M KCl (Figure 4.7). The temperature dependence of CD spectra of **Py2** in 0.1 M KCl and **Py3** in buffer are shown in Figure 4.8. The spectra of **Py3** are independent of temperature, whereas those of **Py2** display a marked decrease in CD intensity between 60°C and 70°C, which is largely reversible upon cooling.

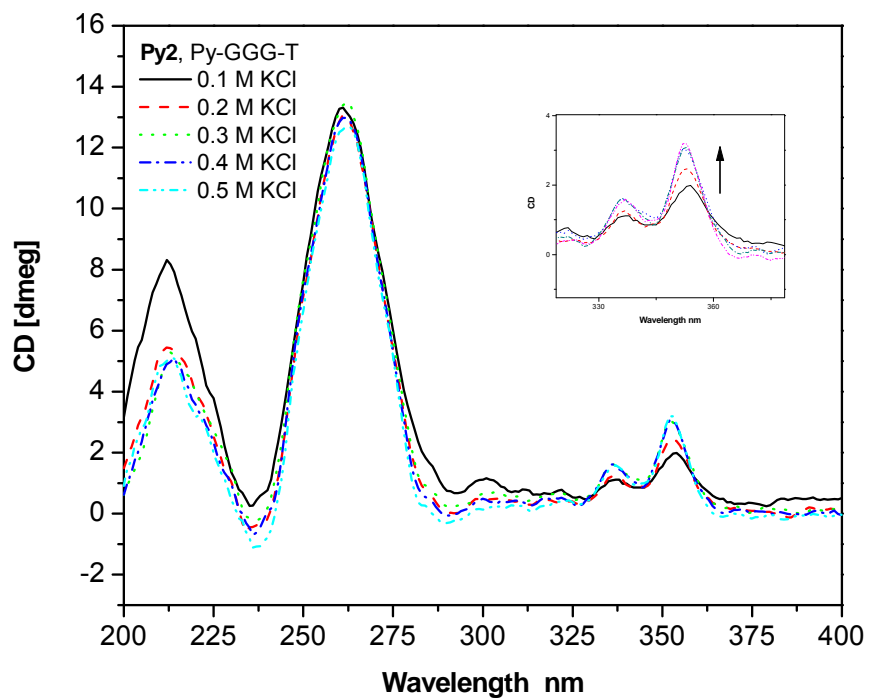


Figure 4.7 CD spectra of **Py2** in different concentrations of KCl (insert shows the expansion of the pyrene region).

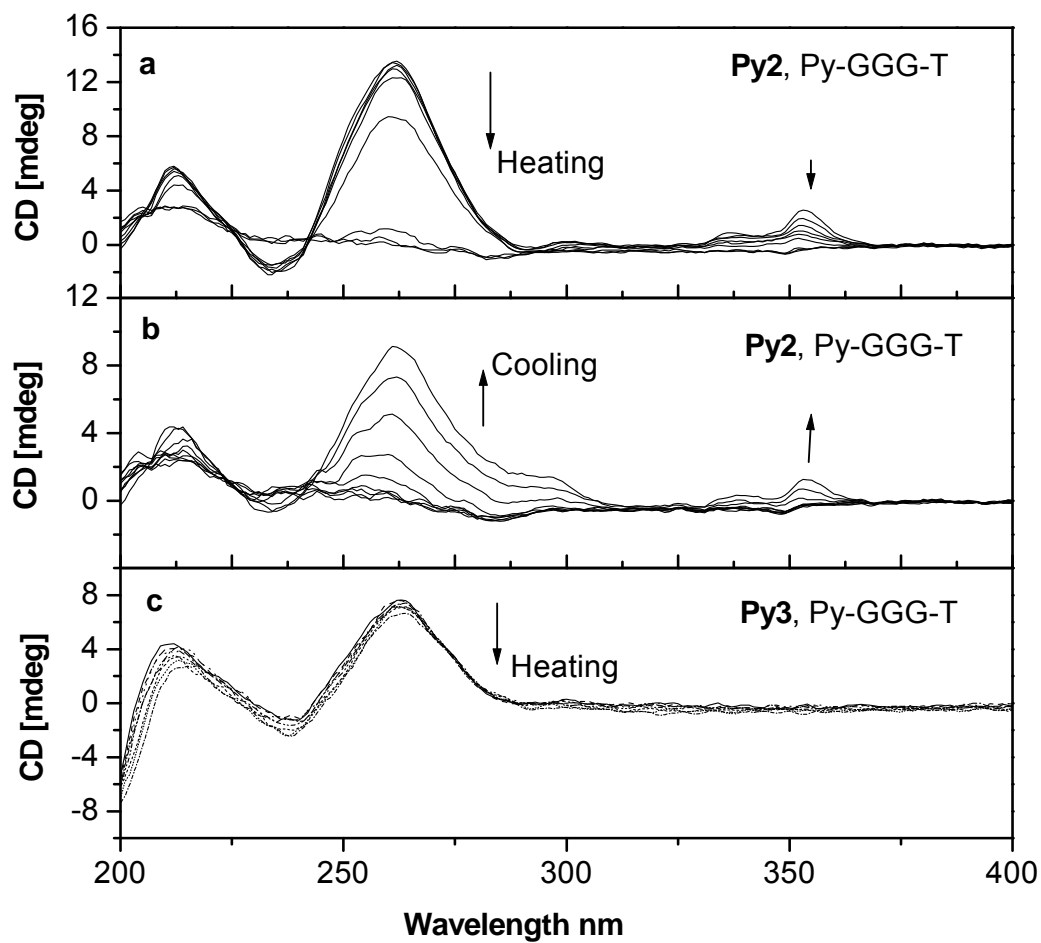


Figure 4.8 Temperature-dependent circular dichroism spectra of conjugates **Py2** and **Py3**, heating rate: 1.5 min / °C. 5×10^{-6} M conjugate **Py2** in 10 mM potassium phosphate with 0.1 M KCl in heating (a) and cooling (b) cycles, and (c) 1×10^{-6} M conjugate **Py3** in water.

Conjugate **Py4** shows a salt dependence different from that observed in **Py2** and **Py3**.

The CD spectra of **Py4** show two positive peaks at 265 nm and 290 nm at relative low KCl concentration, whereas only 290 nm peak disappears at high KCl concentration. However **Py4** shows only one positive peak at 265 nm in NaCl solution (Figure 4.9).

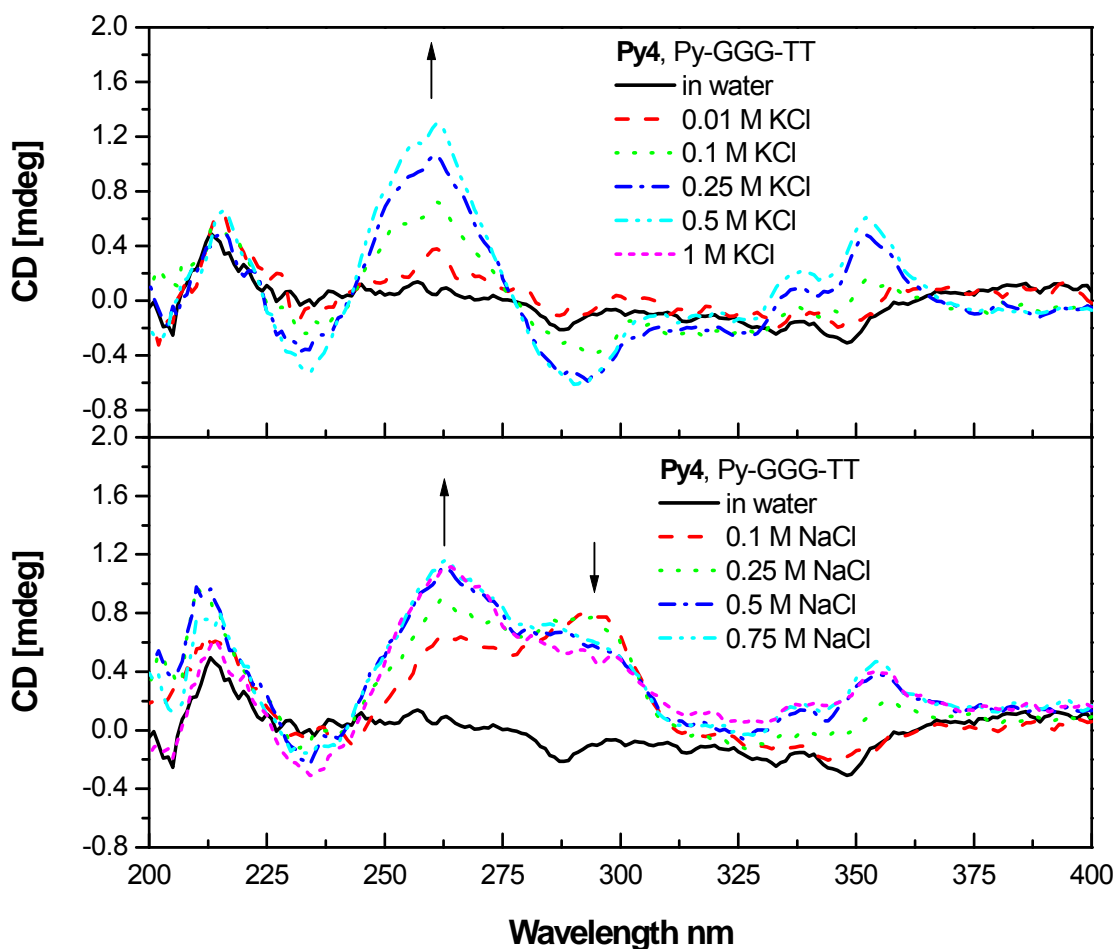


Figure 4.9 CD spectra of **Py4** in different salt concentrations: (a) in KCl, (b) in NaCl.

4.2.3 Fluorescence spectra

The fluorescence spectra of **Py1-Py4** in water and in 0.1 M KCl are shown in Figure 4.10. The spectra of **Py2-Py4** with salt and of **Py3** without salt display a mixture of structured pyrene monomer fluorescence and broad, red-shifted pyrene excimer fluorescence. Only monomer fluorescence is observed for conjugates **Py1**, **Py2**, and **Py4** in water.

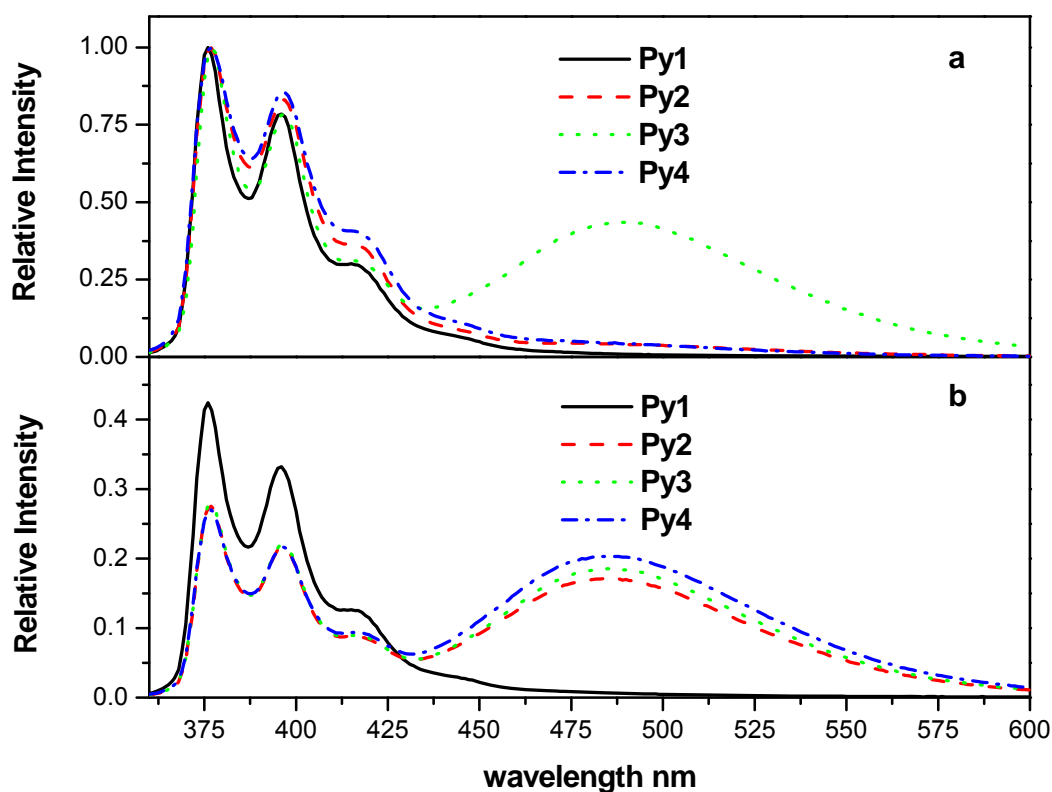


Figure 4.10 Room temperature fluorescence spectra of 1×10^{-6} M conjugates **Py1-Py4** in different salt conditions: (a) in water and (b) in 0.1 M KCl, 10 mM potassium phosphate.

The fluorescence spectra of conjugate **Py4** at KCl and NaCl in different concentration are shown in Figure 4.11. In both salt conditions, the ratio of excimer to monomer emission increases when the salt concentration is increased. The effect of added KCl and LiCl salts

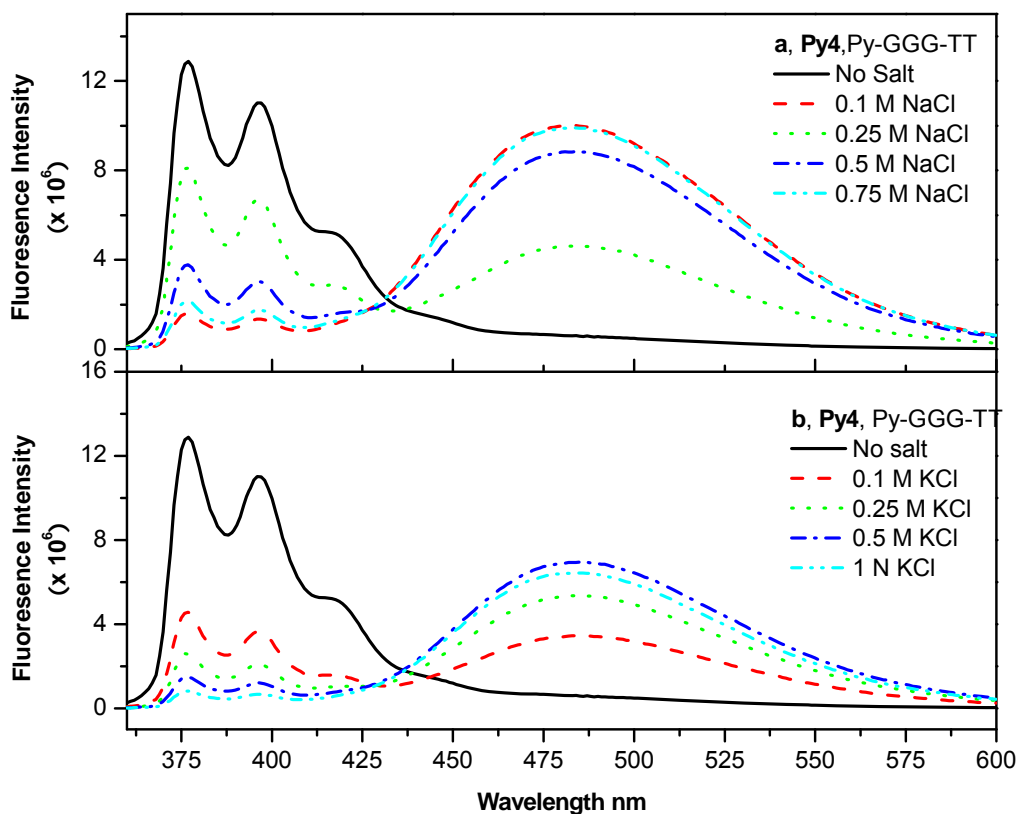


Figure 4.11 The fluorescence spectra of 1×10^{-6} M conjugate **Py4** in different salt conditions: (a) in NaCl and (b) in KCl.

on the ratio of excimer to monomer fluorescence intensity for conjugate **Py2** is shown in Figure 4.12. The ratio $I_{\text{ex}}/I_{\text{m}}$ increases with added KCl to a value of 1.4 at 0.2 M KCl but does not increase further at higher KCl concentrations. The $I_{\text{ex}}/I_{\text{m}}$ ratio also increases upon addition of LiCl to a solution of **Py2** in 0.1 M KCl. Addition of LiCl results in values of $I_{\text{ex}}/I_{\text{m}}$ somewhat

smaller than those for 0.2 M KCl.

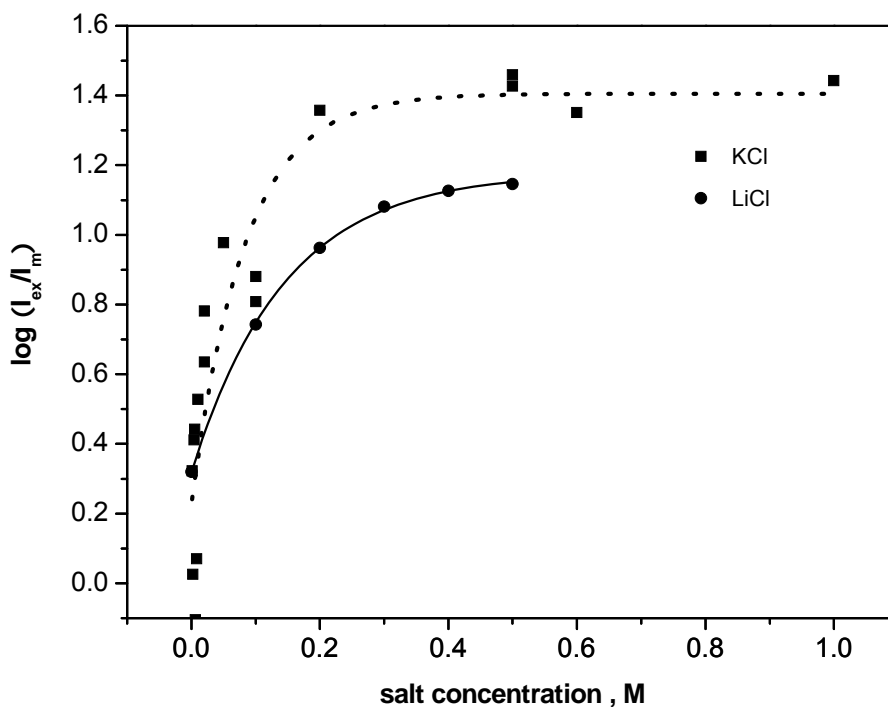


Figure 4.12 Salt concentration dependence of the pyrene excimer/monomer fluorescence intensity ratio for conjugate **Py2** (LiCl added to a solution containing 0.1 M KCl).

The effects of increasing temperature on the total fluorescence of **Py2** (with salt) and **Py3** (in buffer) are shown in Figure 4.13. The ratios $I_{\text{ex}}/I_{\text{m}}$ obtained for both heating and cooling are shown in Figure 4.14. Heating of **Py2** results in a decrease in both monomer and excimer fluorescence intensity (Figure 4.13a). The ratio $I_{\text{ex}}/I_{\text{m}}$ remains fairly constant up to ca. 50 °C, but decreases at higher temperatures (Figure 4.14a). Cooling to 0 °C is necessary for recovery of the $I_{\text{ex}}/I_{\text{m}}$ ratio. Heating of **Py3** effects a larger decrease in I_{m} than I_{ex} (Figure 4.13b) resulting in an

increase in I_{ex}/I_m with increasing temperature (Figure 4.14b). Cooling results in lower values of I_{ex}/I_m than those observed at the same temperatures in the heating cycle.

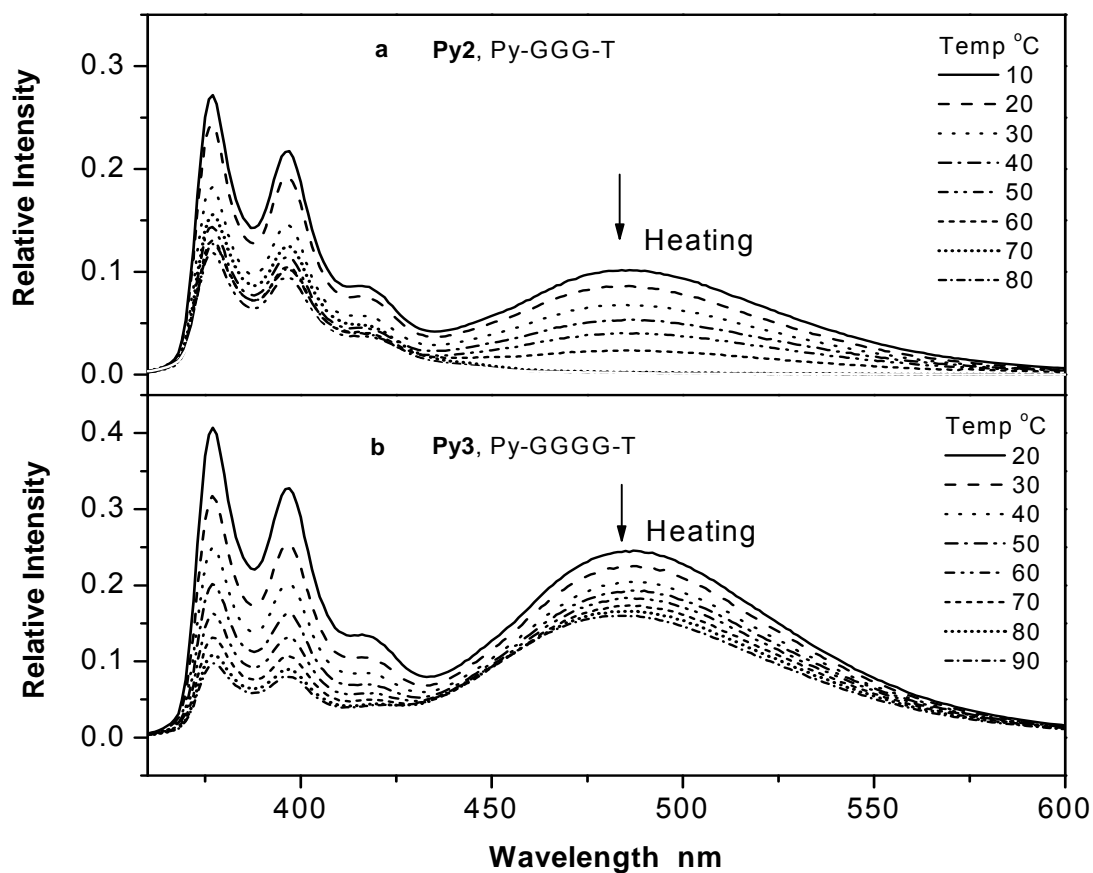


Figure 4.13 Temperature dependent fluorescence spectra of conjugates **Py2** and **Py3**, heating rate: 1.5 min / °C. (a) 5×10^{-6} M **Py2** in 10 mM potassium phosphate with 0.1 M KCl and (b) 1×10^{-6} M **Py3** in 10 mM potassium phosphate.

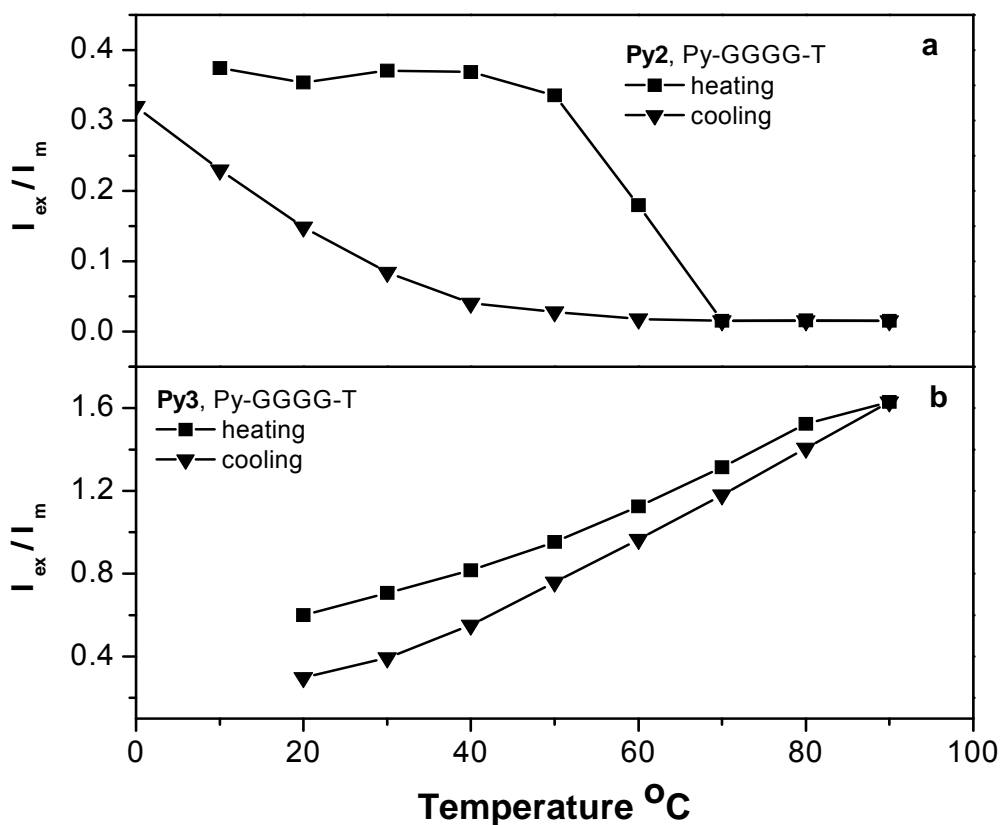


Figure 4.14 Excimer/monomer fluorescence intensity ratio for conjugates **Py2** and **Py3**, heating and cooling rate: 1.5 min / °C. (a) 5×10^{-6} M **Py2** in 10 mM potassium phosphate with 0.1 M KCl and (b) 1×10^{-6} M **Py3** in 10 mM potassium phosphate.

4.2.4 Gel electrophoresis

Excimer fluorescence can also be used to visually detect G-aggregate formation using non-denaturing PAGE under a UV transilluminator, the eye being more sensitive to pyrene excimer vs. monomer fluorescence. Electrophoresis of conjugates **Py2** and **Py3** (3.5×10^{-5} M or 0.3 mM in 0.1 M KCl) yields a single strongly fluorescent band, **Py2** having the higher migration rate. In contrast, the faster moving band from **Py1** cannot be detected visually.

4.3 Discussion

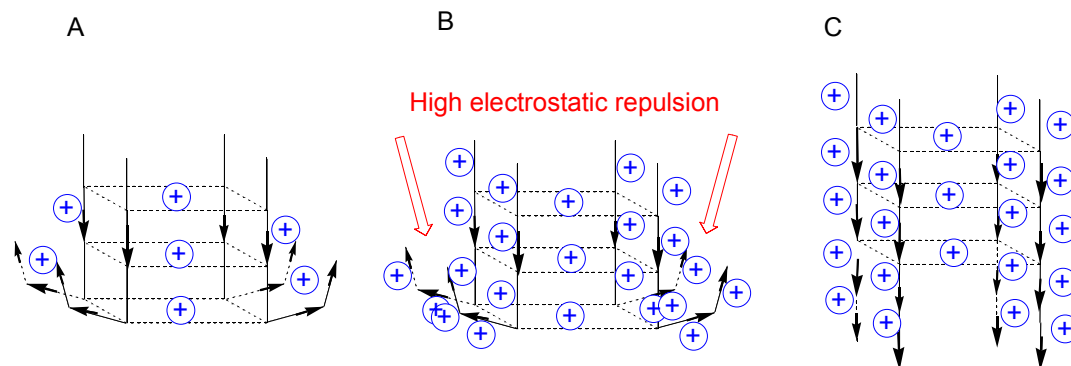
4.3.1 Structures of quadruplexes formed from conjugate Py1-Py4

The conjugates **Py1-Py3** are designed with the 5' end functionalized with pyrenebutanol and 3' end capped with T or TT to prevent the formation of higher aggregates. Previous studies have shown the oligonucleotides d(TGGGT) and d(TGGGGT) form stable parallel G-quadruplex structures in the presence of potassium cation.^{19, 20} Parallel quadruplex formation has not been reported for d(TGGT), however hairpin dimer and intramolecular G-quadruplex structures possessing only two G-quartets have been reported.^{21, 22} The 200-300 nm region of the CD spectra of **Py2** and **Py3** in the presence of KCl (Figure 4.6) are identical, respectively, to those reported for d(TGGGT)₄ and for a G-quadruplex in which the 3'-thymines are connected by a branched linker which enforces a parallel structure.²³⁻²⁵ The relative stronger CD signal for conjugate **Py2** in potassium solution than that in sodium solution is consistent with the observation of higher melting temperature in K⁺ than in Na⁺ for d(TGGGT)¹⁹. The pocket size of the cavity formed by carbonyl groups from four guanines is estimated at 3.36 to 3.87 Å in diameter, varying with the substrate sequences forming the quadruplexes.²⁶⁻²⁹ The radius of potassium cation, about 1.33 Å, is a good match for the size of the cavity, similar to the “snug-fitting” selectivity of potassium ions in potassium channel *KcsA*.³⁰ However if sodium cation ($r = 0.95$ Å) chelates with four carbonyl groups, the phosphorus atoms from the corner strands will be brought into a distance that they in potassium solution. This will increase the repulsion between the four phosphorus backbones, which causes a relatively unstable structure.

The structure of **Py3** is assumed to be similar to that of the conjugate d(TGGGG)-FL (FL = fluorescein) recently studied by Merkina and Fox.³¹ They observe that the quadruplex formed by this conjugate is resistant to melting in the presence of 5 mM potassium. The extra stabilization of FL-labeled quadruplex in sodium buffer compared to unlabeled quadruplex is attributed to the stacking effect of the fluorophore on the 5' terminal face of quadruplex. Similar stacking has been observed in the complexes formed between G-quadruplexes and planar hydrophobic molecule daunomycin.³² Our observation of the lack of change in the CD spectrum of **Py3** upon heating to 90 °C in the presence or absence of 10 mM potassium (Figure 4.8) is in accord with the high thermal stability for d(TGGGGT) or d(TGGGG)-FL.^{31, 33} The failure of **Py1** to form a G-quadruplex structure even at high salt concentration or at low temperature indicates that the hydrophobic association of four pyrenes is not sufficient to provide the extra stabilization necessary for two G-quartets to form an intermolecular G-quadruplex structure.

The CD spectra of **Py4** under constant buffer conditions as a function of salt concentration (10 mM, 100 mM, and 1 M K⁺) are displayed in Figure 4.9. The CD spectra in the presence of K⁺ show a negative band at 235 nm and two positive bands at 265 nm and 290 nm when the concentration of KCl is below 0.5 M. A positive band near 265 nm and a negative band near 238 nm are characteristic of parallel quadruplexes. The positive peak at 290 nm might arise from an antiparallel structure, which has characteristic positive peak at 290 nm and negative peak at 260 nm. Upon increasing the concentration of K⁺, the positive peak at 290 nm decreases, while the positive peak at 260 nm increases. When the concentration of potassium ions reaches to 1 M,

only the positive peak at 260 nm remains. However, in Na environment, only one positive peak at 260 nm is observed when the concentration of Na⁺ changes from 0.1 M to 0.75 M. The different behavior for K⁺ and Na⁺ might be due to the presence of two terminal Ts at each single strand, which increase the possibility of a different orientation on flanking ends. Studies of vertebrate telomere repeats have found that a parallel quadruplex is formed with external loops in antiparallel alignment when the concentration of KCl increases to 0.1 M.³⁴ Since external loops are antiparallel with four corner strands forming a quadruplex scaffold, an additional 290 nm positive peak is observed as a shoulder of 265 nm peak. In our system having two terminal Ts, it is possible that the Ts are back-folding antiparallely with four corner strands, resulting a 290 nm shoulder. A suggested folding model for conjugate **Py4** in different salt conditions is shown in Scheme 4.1.



Scheme 4.1 Proposed folding of conjugate **Py4** in different salt conditions. A) The folding of **Py4** at low K^+ condition. The density of K^+ ions binding on the backbones is relative low at this concentration condition, so the back-folding of two terminal Ts is possible, which causes the 290 nm positive peak in CD spectra. B) Binding of K^+ to the backbone of conjugate **Py4** in high concentration of KCl. Due to the high positive charge density on the surface of backbone and relative bigger radius of potassium cations, back-folding of terminal Ts will be decreased due to the increased repulsive energy, which will change the structure from A to C. C) The assembly of conjugate **Py4** when the concentration of K^+ is high. This is also the assembly mode of conjugate **Py4** in NaCl solution.

As seen in scheme 4.1, when the concentration of K^+ increases, the surface binding of K^+ on the backbone increases. The increased positive charges in back-folding areas caused from two terminal Ts lead to increased charge repulsion, which consequently causes unfavored surface potential energy. To minimize the energy, the back-folding terminals intend to form the structure shown in scheme 4.1C. This hypothesis might be supported by observing a similar result for a strand with three terminal Ts or for a strand with four G-quartets and two terminal Ts. In the case of sodium, since sodium ions have higher surface binding ability than potassium ions, plus the advantage of small radius of sodium ions, four single strands more likely adopt the structure in scheme 4.1C in either low or high Na concentration. Studies have shown the different affinity of

monovalent cations for quartet surface sites, which follows the order $\text{NH}_4^+ > \text{Na}^+ > \text{Cs}^+ >$

$\text{Rb}^+ > \text{K}^+$.³⁵ The higher excimer emission intensity of conjugate **Py4** in 0.5 M KCl than in NaCl

(Figure 4.15) indicates parallel quadruplex structures are formed in both NaCl and KCl

conditions.

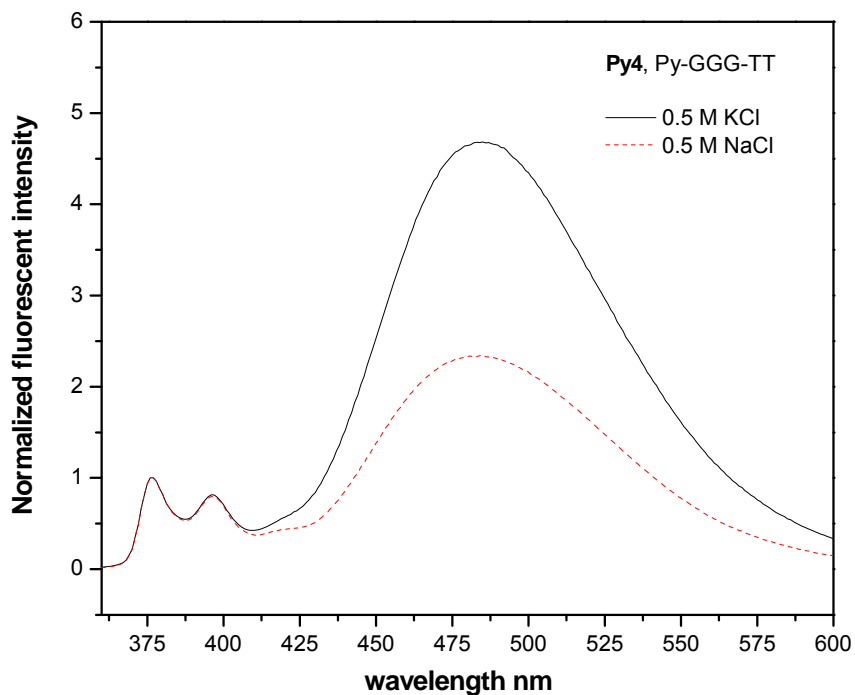


Figure 4.15 Fluorescence spectra of 1×10^{-6} M conjugate **Py4** in 0.5 M NaCl and KCl.

The fluorescence spectra of **Py2** and **Py3** show mixtures of monomer and excimer fluorescence, even though the CD spectra are indicative of the formation of stable parallel G-quadruplexs. It is possible that monomer and excimer fluorescence arise from different

structures. However, PAGE gels for **Py2** and **Py3** display a single band, which shows light green visible pyrene excimer fluorescence, even though the operative concentration of the samples are 35 times higher than that of CD and fluorescent studies. Low pyrene excimer/monomer fluorescence ratios have previously been observed upon duplex and triplex formation with pyrene end-labeled oligonucleotides.^{16, 17} A high excimer/monomer fluorescence ratio has been observed for oligomeric pyrene-containing C-nucleosides³³ and for an intramolecular G-quadruplex having pyrenes attached to both ends of a d(GGTTGGTGTGGTTGG) sequence.¹⁸ However, for several duplexes bearing pyrene as pendant groups on multiple adjacent dU bases, only broadened monomer emission is observed.^{36, 37} These observations show proximity is a necessary, but not sufficient condition for the observation of pyrene excimer emission. Early studies of the fluorescence of conformationally constrained pyrene cyclophanes indicate that a full sandwich-like structure is required for the observation of long-wavelength excimer fluorescence, whereas structures with partial overlap display small shifts or only broadened monomer emission.^{10, 38}

4.3.2 Monomer/excimer emission studies

Conjugates **Py1-Py4** were intended to have four pyrene chromophores occupying the 5'-face of the G-quartets, so that the hydrophobic interactions of both the G-quartet and pyrenes with water can be minimized. However, some of the pyrene chromophores have ground state geometries which disfavor formation of a sandwich excimer with a neighboring pyrene upon

electronic excitation. Evidence of the clustering of pyrenes on a single face of the G-quadruplex is provided by the effect of added salts on the excimer/monomer fluorescence ratio (Figure 4.12). Both added KCl and LiCl cause an increase in the I_{ex}/I_m ratio, even though 0.01 M KCl is sufficient to effect G-quadruplex formation, as evidenced by the CD spectra. Since LiCl is unable to stabilize G-quadruplex structures,^{35, 39, 40} its influence on I_{ex}/I_m most likely is a consequence of a hydrophobic salt effect on the structure of the assembled pyrenes.⁴¹ LiCl and KCl have similar hydrophobic effects on the solubility of nonpolar molecules such as benzene in aqueous solution.⁴¹ Solvation of small ions by water results in collapse of the water molecules around the ions.⁴² This phenomenon, known as electrostriction, increases the energy required for creation of a space for a hydrophobic molecule such as pyrene and would force the four pyrenes attached to the quadruplex to occupy a smaller volume, plausibly favoring excimer formation.

4.4 Conclusion

Conjugates possessing a 5'-pyrenebutanol covalently linked to a poly(dG) sequence can form quadruplex structures. Conjugate **Py3** which possesses a GGGG sequence forms a stable quadruplex even in the absence of added salt and does not dissociate upon heating to 90 °C. In the presence of added KCl conjugate **Py2** forms a quadruplex structure which is stable at room temperature but undergoes thermal dissociation above 60 °C. Evidence based on circular dichroism spectra indicates that both **Py2** and **Py3** form parallel quadruplex structures in which the appended pyrenes occupy the 5'-face of the quadruplex. Conjugate **Py1** fails to form a stable

quadruplex structure even at low temperature in the presence of KCl. Conjugate **Py4** forms well aligned parallel quadruplex in the presence of NaCl and high concentrations of KCl. A salt-dependent folding mechanism has been proposed for conjugate **Py4** at low KCl. Further experiments need to be carried out in order to confirm this proposal.

The fluorescence spectra of the quadruplexes formed by conjugates **Py2-Py4** display both monomer and excimer bands. Upon heating the excimer/monomer band ratio for **Py2** decreases sharply above 50 °C, concomitant with thermal dissociation of the quadruplex. In contrast the excimer/monomer ratio for **Py3** increases with temperature, indicative of a change in pyrene aggregate structure in a manner that favors the face-to-face geometry required for pyrene excimer fluorescence. The effect of added salts (KCl or LiCl) on the pyrene excimer monomer ratio is attributed to electrostriction, which confines the hydrophobic pyrenes to a small volume.

Chapter 5

Design and thermal stability studies of modified thrombin binding agents

5.1 Introduction

In 1992 a study of a pool of DNA containing 60 nucleotides of random sequence have found that 32 of them that inhibit thrombin-catalyzed fibrin-clot formation have a highly conserved 14-17 base region, d(GGTTGGNNNGTTGG).¹ This observation of single strands acting as an aptamer has attracted more and more structural studies focused on these single strand DNAs. Structural studies of thrombin binding agent (**TBA**), d(GGTTGGTGTGGTTGG) using NMR have shown that the **TBA** strand forms a unimolecular DNA quadruplex, as displayed in Figure 5.1.^{2,3} The oligonucleotide folds such that it forms two guanine quartets connected by a central three-base TGT loop and two TT side loops having a potential T · T bp formed between the two TT loops across the diagonal of the top G-quartet, as illustrated in Figure 5.2. In the folded chair conformation, an edge-looped quadruplex structure, is adopted, instead of the diagonal looped structure. X-ray studies of this sequence have shown the quadruplex structure is sandwiched between two different positively charged regions of two symmetry-related thrombin molecules via ionic and hydrophobic interactions.⁴

Studies have found that fibrin formation and polymerization are essential to some neurodegenerative and neurological diseases,⁵ such as mad-cow or Alzheimer disease, and to cardiovascular disease and operation, while fibrin polymerization deflection is found in HIV-infected patients.⁶ Thus molecules or analogues of **TBA** the can either inhibit or enhance the activity of thrombin are be considered as potential targets as therapeutic drugs. Studies of aptamer selection have found oligonucleotides possessing both quadruplex and duplex motifs

show higher binding and inhibitory activity toward thrombin.^{7, 8} A selected highly stable intramolecular four-stranded DNA structure containing two stacked guanine-quartets have been reported to inhibit the replication of the human immunodeficiency virus type 1 (HIV-1) via against HIV integrase.^{9, 10} Selected aptamers inhibit to neutrophil elastase.¹¹ Quadruplex structures also show arginine binding activity.¹²

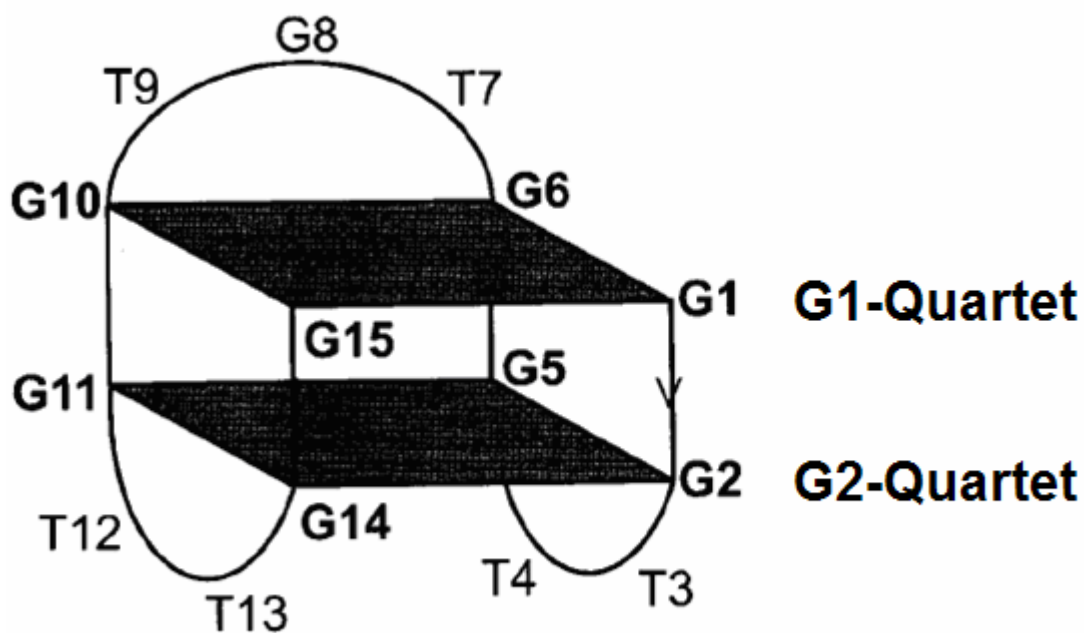


Figure 5.1 schematic drawing of the thrombin aptamer structure. Shaded squares represent guanine quartets (as shown in chapter 1.)

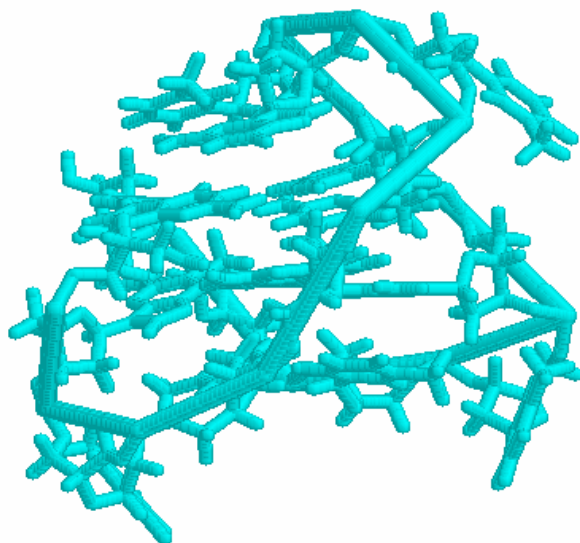


Figure 5.2 NMR structure of oligonucleotide d(G₂T₂G₂TGTG₂T₂G₂). Figure obtained from ref.²

These selected oligonucleotides have shown that their function has a close relationship with their structure and stability, which indicates that two fundamental criteria need to be considered for designing new aptamers; thermal stability and target binding ability. Modified **TBA** has been studied with these considerations in mind. A synthetic three quartet aptamer has been reported to exhibit similar thrombin binding activity similar to that of **TBA**.¹³ Thermodynamic stabilities of modified **TBA** aptamer sequences are dependent upon modifications in the various loop domains of the aptamer, as well as the effect of adding an additional quartet.¹⁴

Previous studies of stilbenediether-containing hairpins in our group have shown increased thermal stability compared to hairpins with natural nucleobase loops. In the work presented here, we examine a series of modified **TBA** aptamer sequences in which the various loop domains replaced by stilbenediether (**Sd**) linkers, as shown in Table 5.1. The thermodynamic stability and structures of these sequences were studied by UV-melting and temperature-dependent CD spectra. The electronic properties of modified sequences have studied by UV-Vis spectroscopy.

Table 5.1 Structure of **TBA** and designed **Sd**-containing sequences.

Name	Sequence
TBA	5' GG-TT-GG-TGT-GG-TT-GG 3'
HTS-1	5' GG-TT-GG- Sd -GG-TT-GG 3'
HTS-2	5' GG- Sd -GGTGTGG- Sd -GG 3'
HTS-3	5' GG- Sd -GG- Sd -GG- Sd -GG 3'
HTS4	5' GG- Sd -GG-TGT-GG-TT-GG 3'

5.2 Results

5.2.1 Synthesis and purification of modified thrombin binding agent

Stilbenediether linker was prepared as described in experiment chapter 6.3.2. Modified conjugates in Table 5.1 are prepared by means of conventional phosphoramidite chemistry.¹⁵ Experiments show that removal of protecting groups of guanines is not fully completed under general ammonium treatment. Therefore the deprotection procedure has been either carried out in longer time or at higher temperature. Isopropyl-phenoxyacetyl protected dG also provides an alternative method. Sequences are purified by HPLC and characterized by UV and by MALDI-TOF mass spectrometry using 3-hydroxypicolinic acid (3-HPA) matrix, as described in Experimental section 6.5.2. Due to the presence of four GG domains in designed sequences, they are stored in ddH₂O at 4 °C.

5.2.2 Electronic absorption spectra and thermal dissociation of Sd-conjugates

The UV absorption spectra of **Sd**-containing oligonucleotides are shown in Figure 5.3. Absorption in 300 – 350 nm is due to the stilbenediether linker. The strand concentration was measured by the extinction coefficient of **Sd**. Thus with increasing the number of **Sd** linkers from **HTS-1** to **HTS-3**, an increased UV absorption in this region is observed. The absorption at 260 nm is dominated by nucleobases. A shoulder has been observed at 280 nm with increasing the number of **Sd** linkers in conjugates.

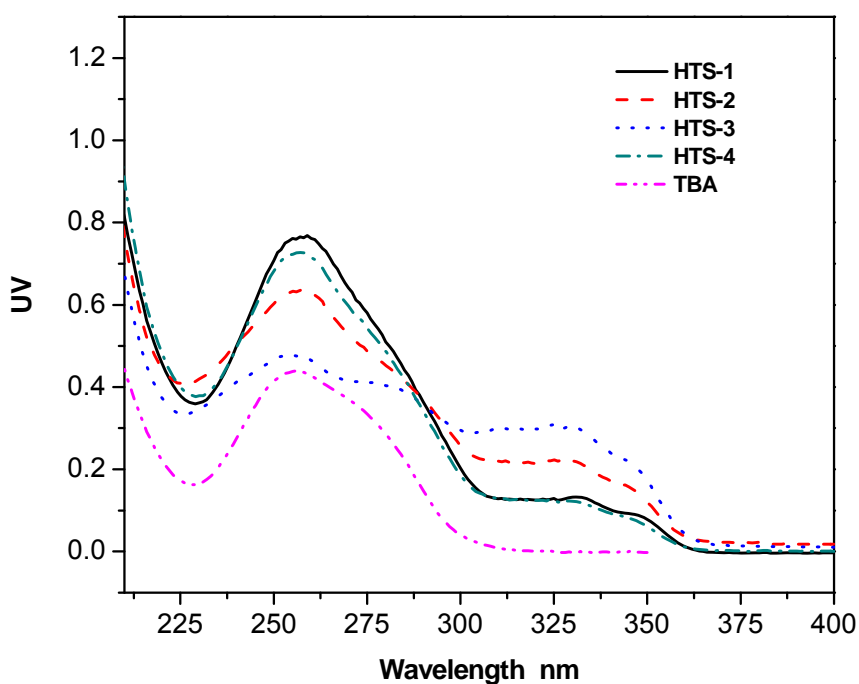


Figure 5.3 UV spectra of **TBA** and **Sd**-linked oligonucleotide conjugates. (3×10^{-6} M conjugate in ddH₂O)

The 295 nm thermal dissociation of **TBA** sequence in 0.1 M KCl has been obtained at 295 nm, as shown in Figure 5.4. Between 0 °C and 60 °C, hypochroism is observed as reported in the literature.^{14, 16} With continuously increasing temperature, a hyperchromism is observed, which has not been reported in literature. Considering the absorption of stilbenediether linker, the thermal dissociation behavior of **Sd**-containing sequences has been recorded at both 295 nm and 324 nm shown in Figure 5.5. UV-melting profiles of **HTS-1** and **HTS-4** at 295 nm are similar to that of **TBA**. At 324 nm, both samples show a well defined hyperchromism curve followed by a continuous absorption increase. However for both **HTS-2** and **HTS-3**, neither wavelength gives

well defined melting curves due to the absence of a fully melted state. Interestingly, unlike **HTS-1** and **HTS-4**, at the wavelength of 295 nm **HTS-2** and **HTS-3** show increased UV absorption with increasing temperature. Melting temperatures (T_m) obtained from first derivative of the profiles of **TBA**, **HTS-1** and **HTS-4** at 295 nm are summarized in Table 5.2.

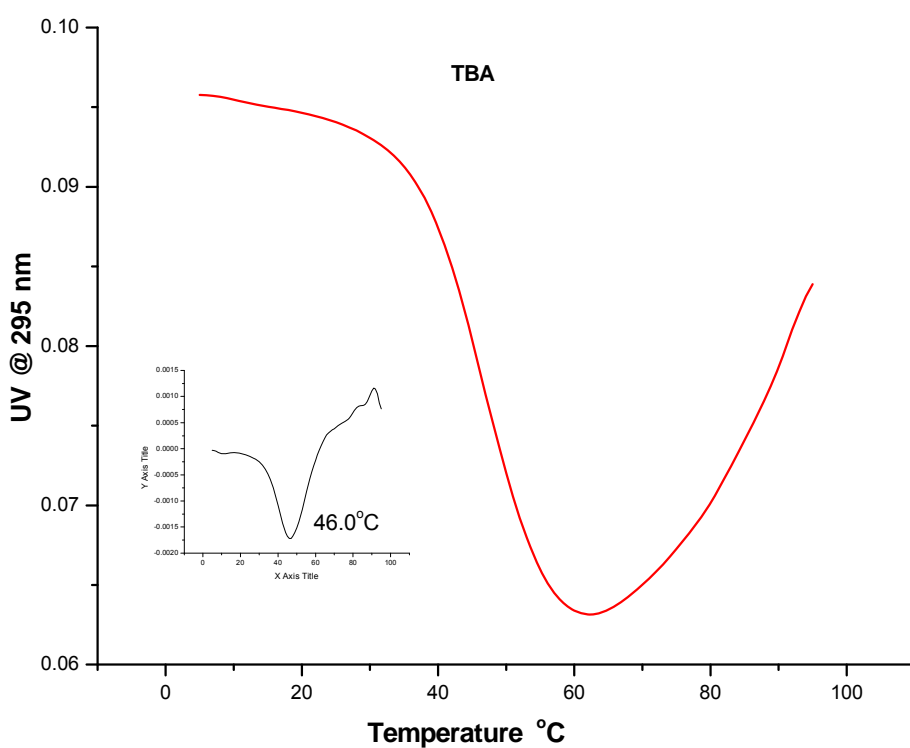


Figure 5.4 Thermal dissociation profile of 3 μ M **TBA** sequence in 0.1 M KCl, 0.01 phosphate buffer, pH 7.0. Data obtained at monitoring UV absorption change at 295 nm with a heating rate of 0.5 $^{\circ}$ C/min. Inset plot shows a melting temperature of 46.0 $^{\circ}$ C

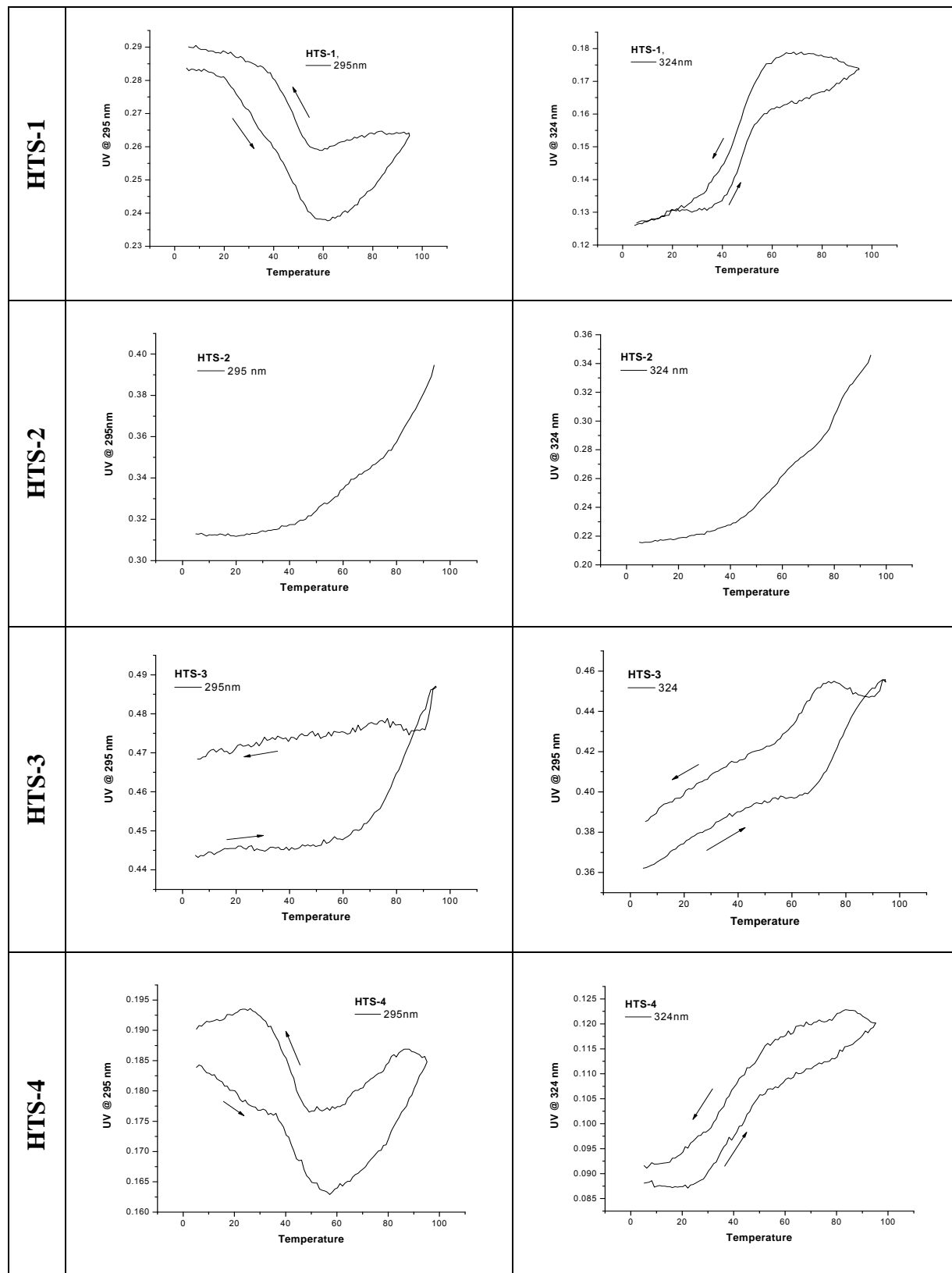


Figure 5.5 Thermal dissociation profiles of 3×10^{-6} M **Sd**-containing conjugates in 0.1 M KCl,

0.01 M Li phosphate buffer, pH=7.0. Data obtained at 295 nm and 324 nm with a heating rate of 0.5 °C/min. Arrows show UV change according to the change of temperature.

Table 5.2 Summary of UV-T_m and CD-T_m values for **TBA** and **Sd**-containing sequences obtained from UV melting curves and CD melting curves.

	UV-T _m		CD-T _m (°C)
	@ 295 nm (°C)	@ 324 nm (°C)	
HTS-1	40.5	47.5	44.3
HTS-2	NA ^b	55.0/80.9 ^a	N/A ^b
HTS-3	NA ^b	NA/76.9 ^a	N/A ^b
HTS-4	42.0	40.3	45.7
TBA	46.0		47.0

^a Two melting temperatures obtained at 324 nm with tentative assignment of melting curves in two transition states. ^b data not available.

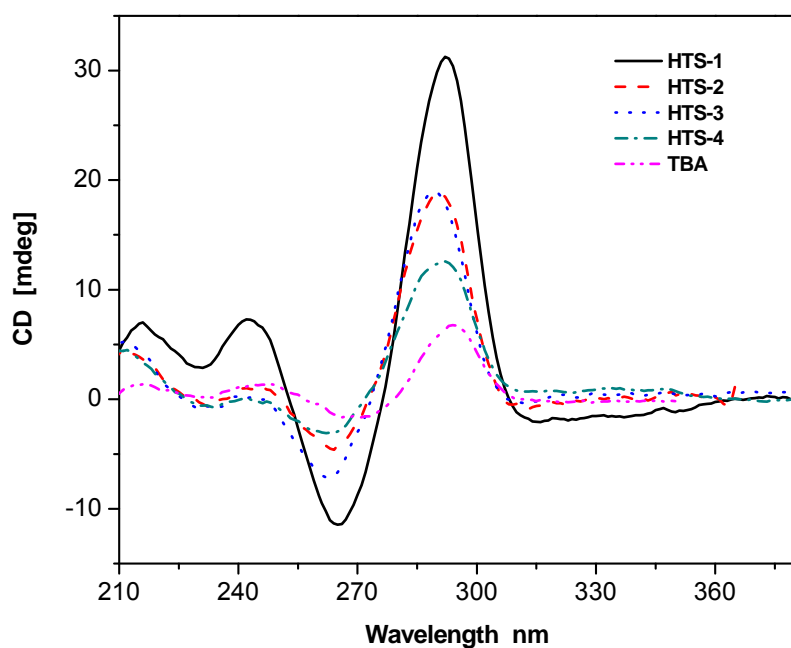


Figure 5.6 CD spectra of 3×10^{-6} M **Sd**-containing sequences and **TBA** sequence in 0.1 M KCl, 0.01 M Li phosphate buffer, pH 7.0. Spectra were recorded at 5 °C.

Table 5.3 The positions of CD peaks of 3×10^{-6} **TBA** and **Sd**-containing sequences in 0.1 M KCl solution.

Name	Position of positive peak	Δ (blue shift) ^a	Position of negative peak	Δ (blue shift) ^a
TBA	294	-	270	-
HTS-1	292	-2	265	-5
HTS-2	290	-4	264	-6
HTS-3	289	-5	263	-7
HTS-4	291	-3	263	-7

^a Δ (blue shift) obtained from subtracting the corresponding **TBA** position from that of **SD**-containing sequences.

5.2.3 CD spectra of TBA and Sd-containing conjugates HTS-1 to HTS-4

CD spectra of **TBA** and **Sd**-containing conjugates in 0.1 M KCl are shown in Figure 5.6. The CD structure of **TBA** sequence shows a positive peak at 294 nm and negative peak at 270 nm, which are the characteristic of an antiparallel quadruplex formed via intramolecular folding of the **TBA** sequence in the presence of potassium. **Sd**-containing conjugates have similar positive and negative peaks with a small blue shift compared to **TBA** (Table 5.3) **Sd**-containing sequences have higher CD intensities than that of **TBA**. **HTS-1** has the highest CD intensity of the **Sd**-containing conjugates. Due to the incorporation of stilbenediether linker CD signals in the 300-350 nm range have been observed for **Sd**-containing sequences (Figure 5.6). Sample **HTS-1** has a negative peak at this range, while other 3 samples show positive peaks.

5.2.4 Temperature dependent CD study of TBA and Sd-containing sequences

For purposes of comparison with our modified **Sd**-containing sequences with native thrombin binding agent **TBA**, a temperature dependent CD study has been carried out, as shown in Figure 5.7a. The CD melting profile of **TBA** at 295 nm is presented in Figure 5.7b and the T_m value is reported shown in Table 5.2.

Thermal stabilities and structure changes of loop modified sequences were studied using temperature dependent CD spectra as well, as shown in Figure 5.8 for **HTS-1**, Figure 5.9 for **HTS-2**, Figure 5.10 for **HTS-3**, Figure 5.11 for **HTS-4**. The CD-melting curves at 295 nm are provided in Figure 5.12. Both **HTS-1** and **HTS-4** show well defined equilibrium states before and after dissociation process. The behavior of non-clear transition in **HTS-2** and **HTS-3** is

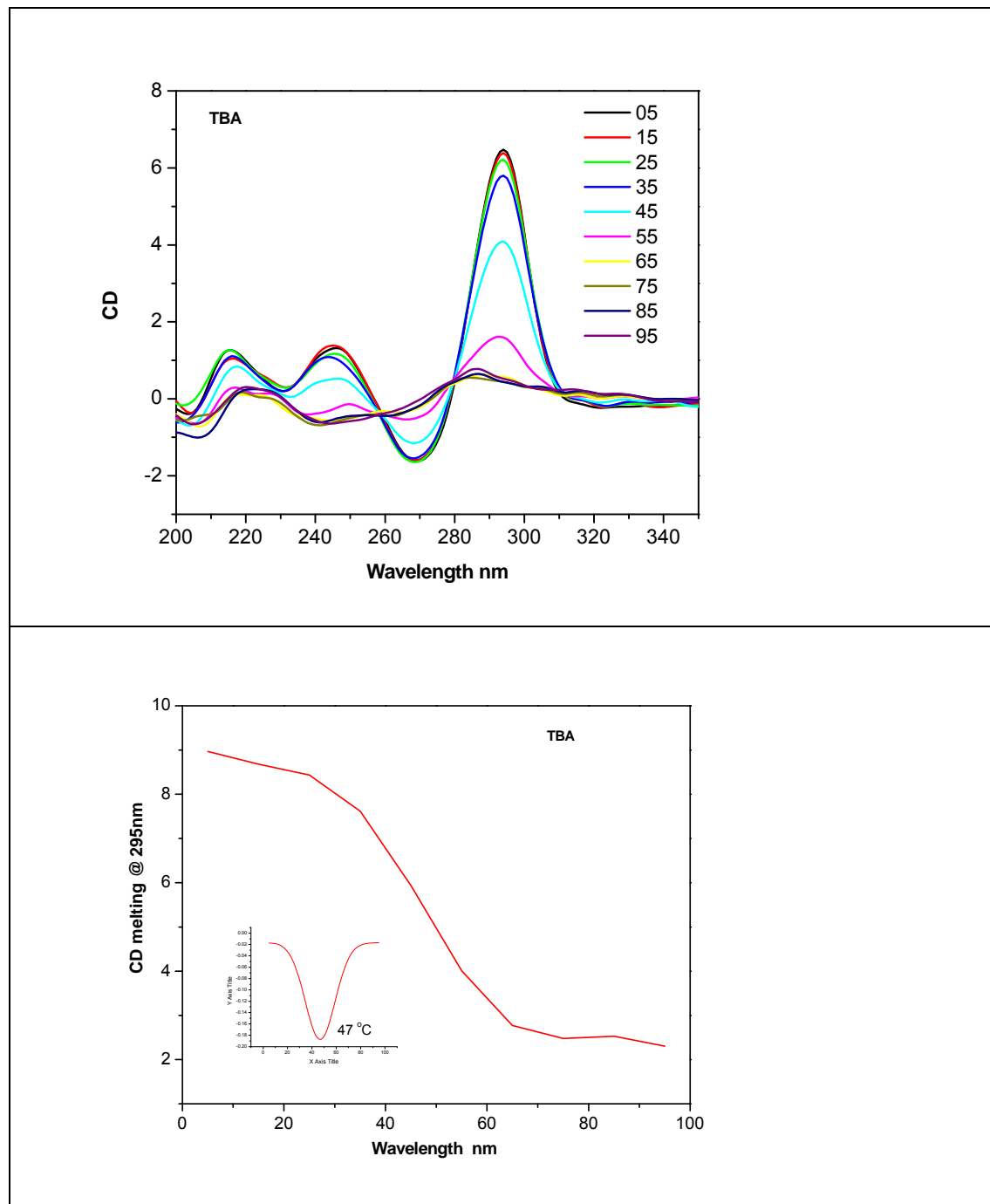


Figure 5.7 a, top) Temperature dependent CD dissociation of 3 μM **TBA** in 25 mM KCl, 0.01 M phosphate buffer, pH 7.0 b, bottom) CD melting profile of TBA obtained at 295 nm. Inserted plot shows a T_m value of 47.0 $^{\circ}\text{C}$.

similar to the observation in UV-melting profiles. The CD intensities at 295 nm of **HTS-1**, **HTS-2**, and **HTS-3** can be mostly recovered after one heating and cooling cycle, while **HTS-4** lost nearly half of intensity (Figure 5.12).

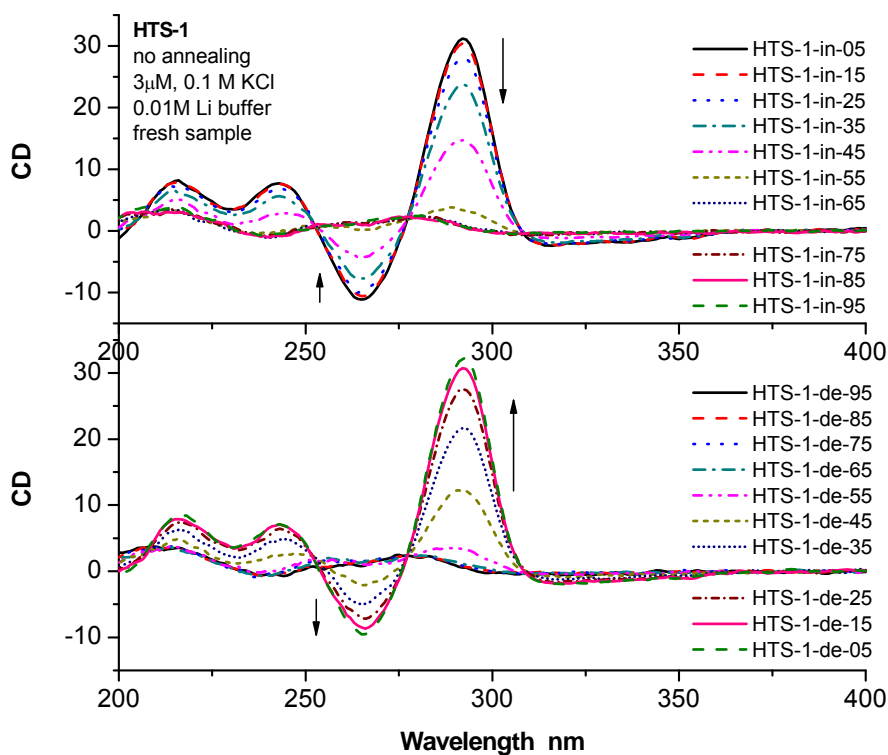


Figure 5.8 Temperature dependent CD spectra of 3×10^{-6} M **HTS-1** in 0.1 M KCl, 0.01 M Li phosphate buffer, pH 7.0, with a heating/cooling rate 0.5 $^{\circ}$ C/min.

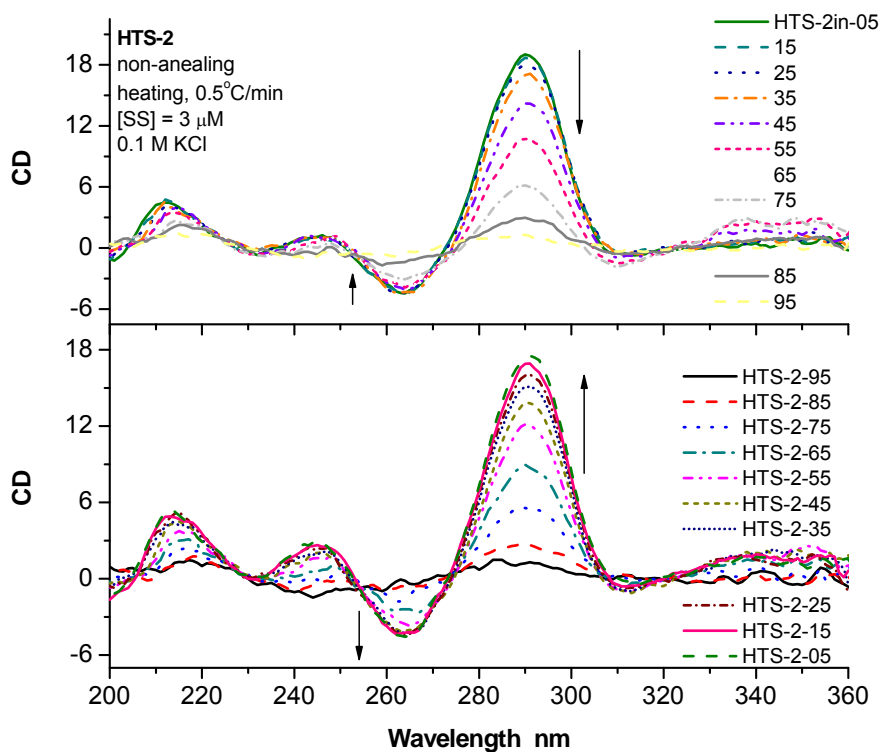


Figure 5.9 Temperature dependent CD spectra of 3×10^{-6} M **HTS-2** in 0.1 M KCl, 0.01 M Li phosphate buffer, pH 7.0, with a heating/cooling rate 0.5 °C/min.

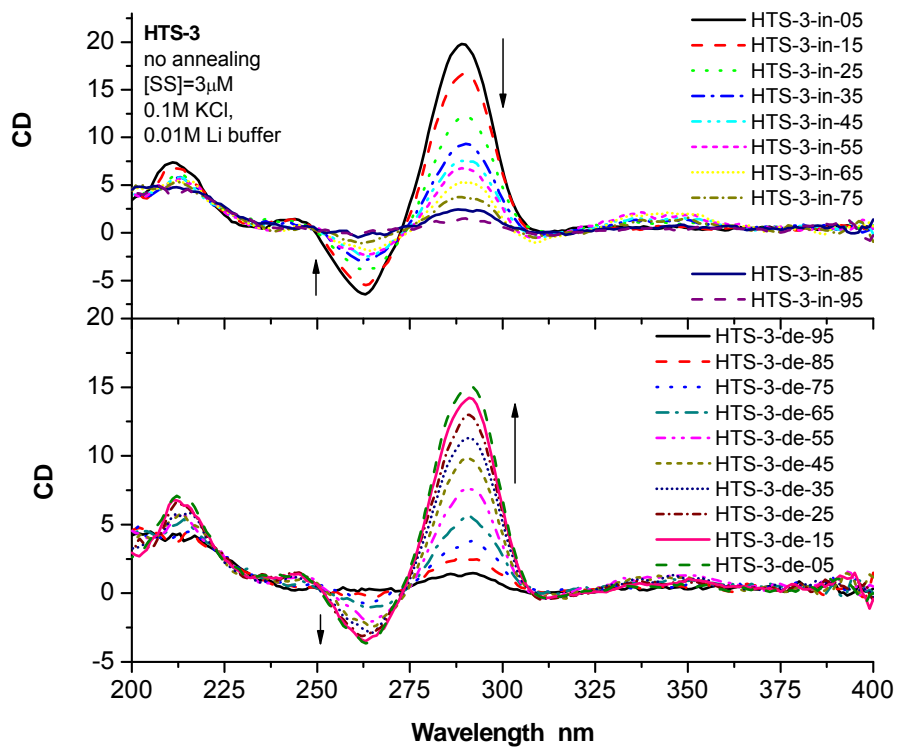


Figure 5.10 Temperature dependent CD spectra of 3×10^{-6} M HTS-3 in 0.1 M KCl, 0.01 M Li phosphate buffer, pH 7.0, with a heating/cooling rate 0.5 $^{\circ}$ C/min.

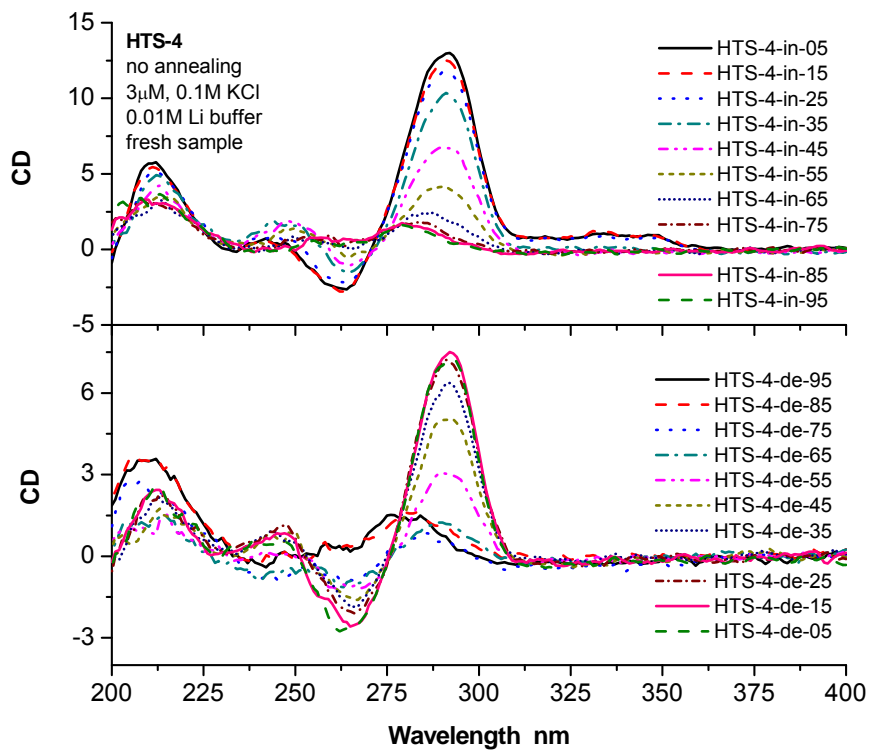


Figure 5.11 Temperature dependent CD spectra of 3×10^{-6} M HTS-4 in 0.1 M KCl, 0.01 M Li phosphate buffer, pH 7.0, with a heating/cooling rate 0.5 $^{\circ}$ C/min.

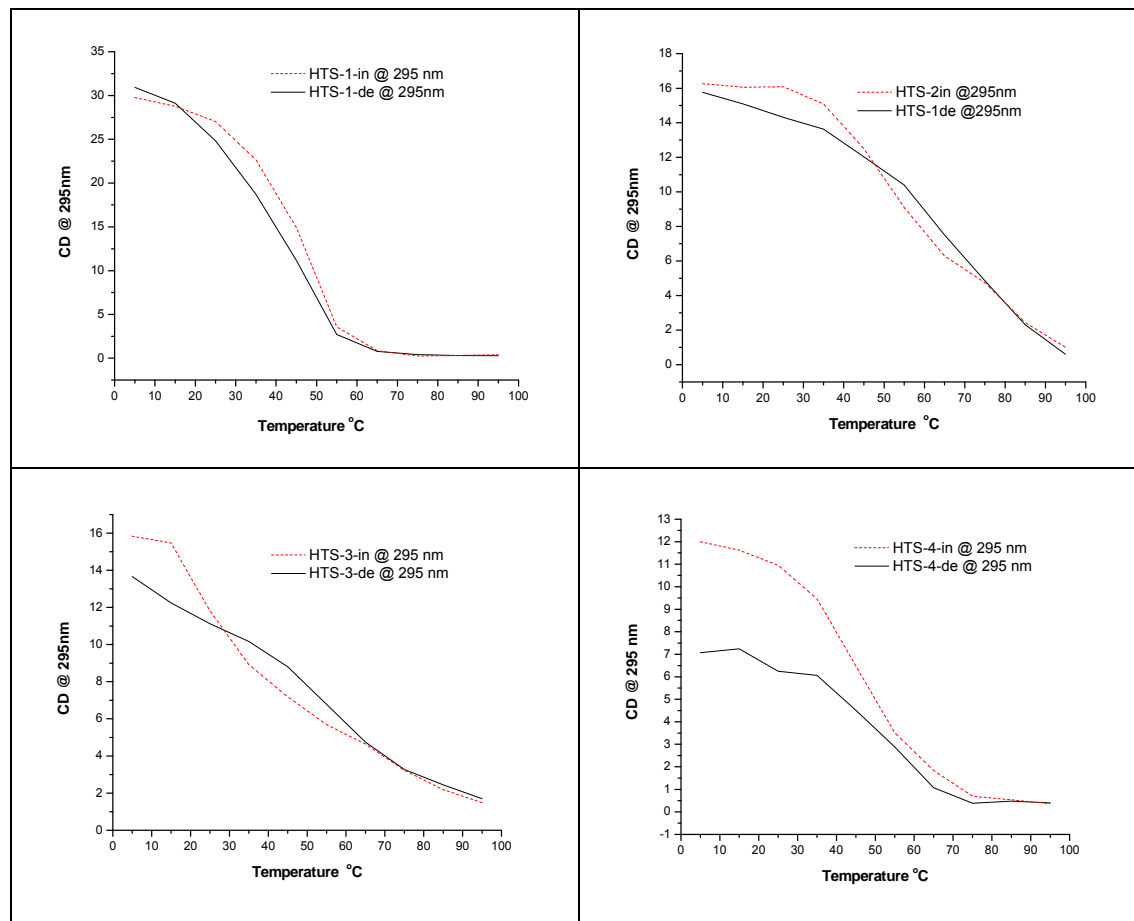


Figure 5.12 CD-melting profiles of of 3×10^{-6} M **Sd**-containing conjugates in 0.1 M KCl, 0.01 M Li phosphate buffer, pH=7.0, with a heating/cooling rate 0.5 °C/min. The CD melting measurements were recorded at 295 nm.

5.3 Discussion

5.3.1 Structures of Sd-modified thrombin binding agent sequences

The similarity of the spectra CD of Sd modified sequences (Figure 5.6) to that of **TBA** sequence indicates that they all form antiparallel quadruplex structures via intramolecular folding. Studies have shown that in the folded **TBA** structure (Figures 5.1 and 5.2), there are two G-quartets (G1-quartet and G2 quartet) stacking with each other.² There is also diagonal T4 · T13

base pairing between two side loops. The G8 and T9 in central loop region stack on the G1-quartet, while T7 is binding in a major groove. The oxygen-oxygen (O-O) distances between two strands of a G-quaduplex are obtained from crystal structure of d(G₄T₄G₄), which is formed through dimerization of two hairpins.¹⁷ The O-O distance for the two strands positioned on one edge of the G-quartet is 17.4 Å, while the O-O diagonal distance for the two diagonal strands is 22.4 Å. The 18.1 Å length of stilbenediether linker makes it be able to span the distance of two adjacent strands in order to replace the three natural edge loops in **TBA** sequences, as modeled in Figure 5.13. As shown in the model, the incorporation of stilbenediether linkers in any loop region can result in a hydrophobic interaction between stilbenediether linker and the adjacent G-quartet. This interaction may lead to induced CD or exciton coupled CD (EC-CD) signal in stilbenediether absorption range. Our observation of a weak band in the 300-350 nm range provides additional evidence that quadruplex structures have been formed from all four stilbenediether linked sequences.

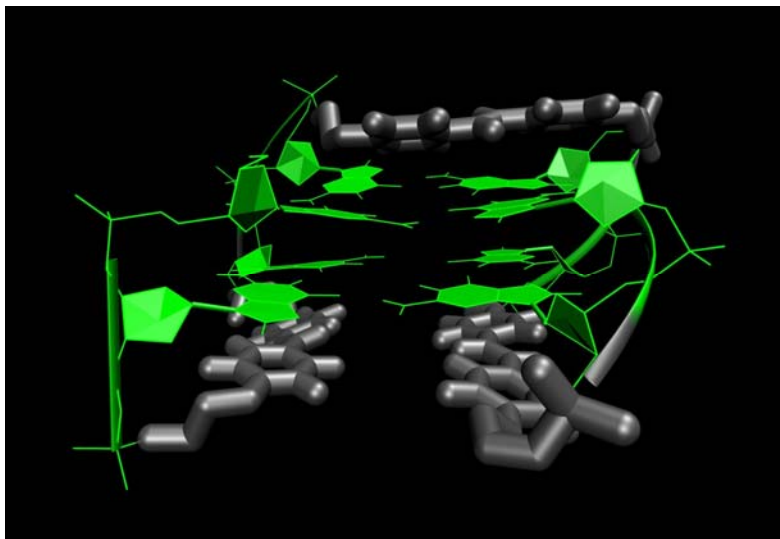


Figure 5.13 Molecular modeling of **HTS-3**. Stilbenediether linkers shown in gray, guartets in green.

5.3.2 Thermal stability of Sd-containing sequences

For the well defined melting curves of **HTS-1**, **HTS-4**, and **TBA**, thermodynamics parameters have been calculated by Van't Hoff analysis, as summarized in Table 5.4. The free energy value of **TBA** sequence matches the value of $-1.57 \text{ kcal mol}^{-1}$ at $37 \text{ }^{\circ}\text{C}$ in the literature.¹⁸ The increased ΔG_{VH} values of **HTS-1** and **HTS-4** are consistent with our observation of a slightly decrease in melting temperatures from both UV melting and CD melting processes.

Table 5.4 Thermodynamics formation of quadruplexes from **Sd**-containing thrombin binding sequences and **TBA** sequence by Van't Hoff analysis of UV melting curves at 295 nm.^a

sequences	T_m (°C)	ΔH_{VH} (Kcal mol ⁻¹)	ΔS_{VH} (cal mol ⁻¹ K ⁻¹)	$\Delta G_{VH}(37^\circ\text{C})$ (kcal mol ⁻¹)
HTS-1	40.54	-21.8	-69	-0.24
HTS-2	N/A			
HTS-3	N/A			
HTS-4	42.03	-52.4	-166	-0.83
TBA	46.0	-54.4	-170	-1.53
TBA ^b	46.4	-39.7	-123	-1.57

^a The oligos were prepared at 3 μM strand concentration in 0.1 M KCl, 0.01 M Li phosphate buffer at pH 7.0. Van't Hoff enthalpy and entropy changes (ΔH_{VH} and ΔS_{VH}) for the thermal transitions were calculated according to the equation $\ln K(T) = -\Delta H_{VH}/RT + \Delta S_{VH}/R$, where K is the equilibrium constant for the G-quadruplex transition and was determined by the UV-thermal curve. Plotting of $\ln K(T)$ versus $1/T$ allowed to obtain the values of ΔH_{VH} and ΔS_{VH} , respectively, from the slope and the intercept of the linear regression. Free energies (ΔG_{VH}) were calculated at 37°C using the Gibbs equation $\Delta G_{VH}(T) = \Delta H_{VH} - T\Delta S_{VH}$.

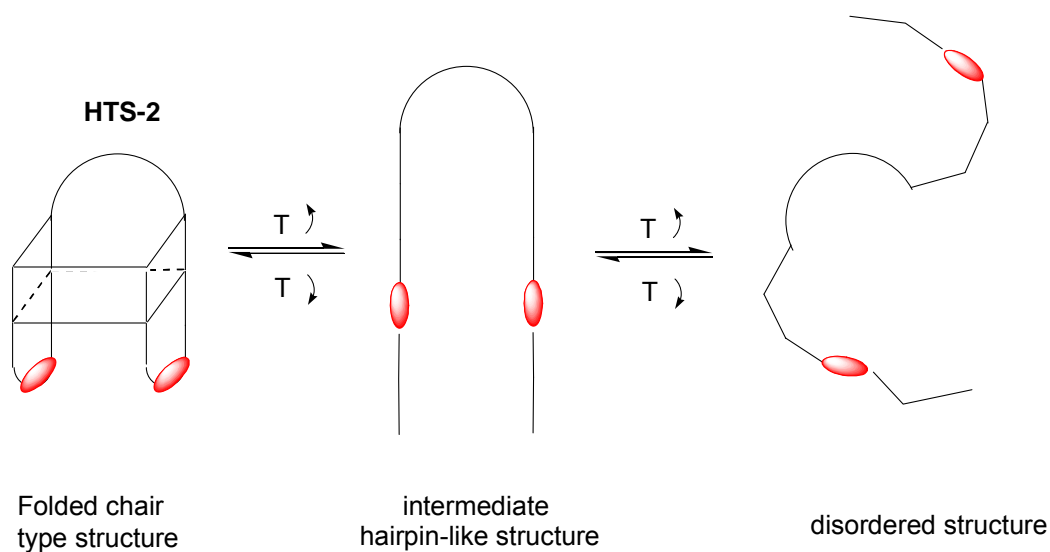
^b Data obtained from ref¹⁸

The melting curves in temperature dependent UV studies of **HTS-2** and **HTS-3** at both 295 and 324 nm, are indicating that they might have higher stabilities than sequences with only one loop replacement. Increased stability is attributed to π -stacking from more than one stilbenediether linker. Also since more than one loop region has been replaced by stilbenediether linker in **HTS-2** and **HTS-3**, the absorption of stilbenediether at 295 nm will be competitive with that of G-quadruplexes, which might result in the observation of net hyperchromism at 295 nm in the UV melting curves for both **HTS-2** and **HTS-3** (Figure 5.5). This competitive absorption may also affect the appearance of temperature dependent CD spectra for **HTS-2** and **HTS-3**, both of which have a continuous decrease in CD signal at 295 nm.

5.3.3 Proposed two-step dissociation mechanism for DNA aptamer TBA

Interestingly, the CD-melting curves in the 300-350 nm region of both **HTS-2** and **HTS-3** show an initial increase in intensity and then a decrease in intensity when the temperature is increased from 5 °C to 95 °C. The intensity reaches maximum between 55-65 °C (Data not shown). The tandem rise and decay in this wavelength range has been observed for both samples when the temperature has been decreased from 95 °C to 5 °C (data not shown). This indicates there is a change in the interaction of stilbenediether linkers in **HTS-2** and **HTS-3**. When only one loop region is replaced, as in **HTS-1** or **HTS-4**, there is only a single collapse during heating and a single reforming during cooling in 300-350 nm CD band. Therefore we propose a mechanism of two-step dissociation process of this chair type quadruplex formed from two

quartets as presented in Scheme 5.1, which is different from the reported unfolding mechanism of **TBA** in the presence of Sr^{2+} .¹⁹



Scheme 5.1 Proposed two-step dissociation mechanism of unfolding of chair type quadruplexes formed from two quartets. Molecule **HTS-2** is used for illustrating the unfolding process. The dihedral angle in between two stilbenediether linkers in the intermediate hairpin-like structure could be flexible.

In this mechanism, the intermediate hairpin-like structure may increase the flexibility of the conformation of two stilbenediether linkers at side loop positions, which enables them to have exciton coupled CD signals (EC-CD). This two-step dissociation mechanism may also explain the observation of the change from hypochromism to hyperchromism in the UV-melting profile of **TBA** sequence.

5.4 Conclusion

We have studied the thermal stabilities of newly designed analogues of the thrombin binding aptamer having stilbenediether loop regions. Studies have found that the nucleobase sequence of the central loop and two side loops are essential to maintain the stability of the quadruplex structure formed from the TBA sequence. Modified conjugates with incorporation of one stilbenediether linker in either central loop region or one side loop region maintain the thermal stability of the quadruplex structures. With two side loops replaced by stilbenediether linkers or three loops replaced by stilbenediether linkers, the thermal stability is greatly increased according to the UV-melting profiles. Based on the change of CD signal in stilbenediether absorption region in **HTS-2** and **HTS-3**, a two-step unfolding mechanism has been proposed for chair type quadruplexes with two quartets. Hydrophobic interaction of the stilbenediether linker with the G-quartets is assumed to be able to stabilize the quadruplex structures in this study, however further experiments using modified sequences with non-hydrophobic linkers, such as polyethylene chains, alkyl chain, or abasic nucleotides, need to be carried out. Considering the

increased thermal stability of newly designed **TBA** analogous, in vitro studies of binding abilities to thrombin may prove interesting.

Chapter 6

Experimental section

6.1 Materials

All chemicals for intermediate synthesis were purchased from Aldrich, unless otherwise stated and were used without further purification. Anhydrous reagents and solvents were supplied by Aldrich in Sure-Seal bottles. Nucleotide phosphoramidites and solid supports for solid phase DNA synthesis were purchased from Glen Research. Reagents for gel electrophoresis were purchased from BioRad Laboratories. TLC was carried out on Sorbent silica G plates. Column chromatography was performed on silica gel.

All oligonucleotides were purified by RP-HPLC and stored in ddH₂O. Concentrations of oligonucleotide solutions were measured by UV absorption by 260 nm, 350 nm for Sa-Sd-hairpins, or 334 nm for pyrene-containing oligonucleotides. Extinction coefficients of oligonucleotides were calculated by the nearest neighbor method. Extinction coefficient of pyrenebutanol was determined in THF solution. Extinction coefficients of stilbenediether and stilbenediamide were measured in methanol solution.

6.2 Instrumental

NMR: ¹H and ³¹P 1-D NMR spectra data were measured on a Varian Mercury 400-MHz or a Varian INOVA-500 MHz NMR Spectrometer, and VNMR operation software was used to process the NMR data.

DNA Synthesizer: Solid phase DNA synthesis was carried out on the Millipore Expedite nucleic acid synthesizer. An Expedite 1.1 workstation was used to control and program the solid

phase DNA synthesis.

HPLC: Reverse phase (RP) HPLC, Dionex (Sunnyvale, CA) DX 500 PEEK system with GP 40 gradient pump, AD 20 detector, and Peakner 1.1 workstation, or Summit SST system with P580 LPG gradient pump, UVD 340S photodiode array detector, and chromeleon 6.00 workstation, or Waters series 600 HPLC system with Empower workstation was used to carry out the analysis and purification of all oligonucleotides. HyperClone (5 μm , 250-4.6) columns from Phenomenex were used in RP-HPLC system. Aqueous triethylammonium acetate (TEAA) and acetonitrile were used as mobile phases. DNA and EG-hairpins were monitored at 260 nm. Sa-Sd-containing DNA was monitored at both 334 nm and 260 nm.

MS: High resolution mass spectral data for synthetic DNAs were obtained by means of electron spray ionization mass spectroscopy. The mass spectra were measured on a Micromass Quattro II atmospheric pressure ionization (API) triple quadrupole mass spectrometer. Matrix assisted laser desorption ionization time of flight mass spectra (MALDI-TOF) were obtained on a Perseptive Biosystem Voyager Pro DE spectrometer. Authentic poly(T) strands were employed as calibration standards. A mixture of 2,4,6-trihydroxyacetophenone (THAP) and ammonium citrate was used as matrix.

UV-Vis: UV-Vis spectra were recorded on a Perkin-Elmer lambda 2 spectrometer. Thermal dissociation experiments were carried out using the Perkin-Elmer spectrometer equipped with a Peltier PTP-1 temperature programmer and a NESlab RTE-100 refrigerated circulator for automatically increasing the temperature at the rate of 0.5°C/min.

Circular Dichroism Spectroscopy (CD): CD spectra were obtained using a Jasco J-715 spectropolarimeter with 165-900 nm photomultiplier tube with a Jasco Peltier type temperature controller and a NESlab RTE-100 refrigerated circulator for automatically increasing the temperature at the rate of 0.5°C/min.

Fluorescence Spectroscopy: Fluorescence spectra were measured on a Spex FluoroMax Fluorometer with temperature control provided by a Quantum Northwest TC 125 Peltier controller. Fluorescent spectra were collected after samples were deoxygenated by purging with dry nitrogen gas for 15 minutes. Fluorescence spectra of Sa-containing DNA samples were excited at 340 nm and monitored from 300 nm to 700 nm. Pyrene-containing DNA samples were excited at 336 nm and monitored from 360 nm to 600 nm. The integration time was 0.1 s and slits for both excitation and emission were 5.0 nm. Temperature dependent fluorescent spectra were collected with heating or cooling rate of 40°C/hr. All spectra were obtained on freshly prepared samples within 30 minutes of preparation.

Gel electrophoresis: Gel electrophoresis was performed using a BioRad vertical gel casting system equipped with a BioRad PowerPac 3000 power supply. Acrylamide storage solution was prepared as a 50% (w/v) aqueous solution of 29:1 acrylamide: bisacrylamide (w/w) and was diluted to proper concentrations before polymerization.

TEM: Transmission electron microscopic images were recorded on a Hitachi HF-2000 instrument. TEM samples were prepared by approaching a Holey Carbon copper grid (400 mesh, SPI supplies) to droplet of DNA solution (10-100 mM) on a clean glass slide for 45 seconds. The

grid was rinsed with water for 10 seconds and stained by uranyl acetate solution for 30 seconds. Excessive liquids were removed by touching the grid with the edge of a piece of filter paper. The grid was air dried and submitted for TEM observation.

Fluorescence Decay: Picosecond (ps) fluorescence decay measurements were carried out by Dr. Vladimir Shafirovich in New York University. In the picosecond single photon counting system the sample is excited by a Coherent Mira 900 femtosecond Ti:Sp laser that is pumped by an Innova 310 argon ion laser. The output of the Ti:Sp laser (700 nm) is passed through a Conoptics electro-optic light modulator system consisting of a Model 350-160 Modulator, a Model 25D Digital Amplifier, and a M305 Synchronous countdown electronics, to reduce the laser pulse frequency from 76 MHz to 12 MHz, which is then doubled to provide excitation at 350 nm. Fluorescence emission is registered at 390 nm using an Aries FF250 monochromator. A Time Harp 100 PC card (PicoQuant, Germany) controlled by an IBM PC computer provide registration of the counts with rates of up to 80 MHz. After deconvolution (PicoQuant FluoFit software), the time-resolution of this apparatus is ca. 35 ps. All experiments, including data collection and analysis, are controlled by an IBM PC computer using PicoQuant software.

Femtosecond broadband pump-probe spectroscopy: femtosecond and picosecond transient spectra were measured by Milen Raytchev and Qiang Wang in Boston College. The changes in optical density were probed by a femtosecond white-light continuum (WLC) generated by tight focusing of a small fraction of the output of a commercial Ti:Sp based pump laser (CPA-2010, Clark-MXR) into a 3 mm calcium fluoride (CaF_2) plate. The WLC provides a

usable probe source between 300 and 750 nm. The WLC was split into two beams (probe and reference) and focused into the sample using reflective optics. After passing through the sample both probe and reference beams were spectrally dispersed and simultaneously detected on a CCD sensor. The pump pulse (1 kHz, 400 nJ) was generated by frequency doubling of the compressed output of a home-built NOPA system (from 666 nm to 708 nm respectively, 7 μ J, 40 fs). To compensate for group velocity dispersion in the UV-pulse an additional prism compressor was used. The overall time resolution of the setup is determined by the cross correlation function between pump and probe pulses which is typically 120 – 150 fs (fwhm, assuming a Gaussian lineshape). A spectral resolution of 7-10 nm was obtained. All measurements were performed with magic angle (54.7°) setting for the polarization of pump with respect to the polarization of the probe pulse. A sample cell with 1.25 mm fused silica windows and an optical path of 1 mm was used for all measurements. A wire stirrer was used to ensure fresh sample volume was continuously used during the measurement.

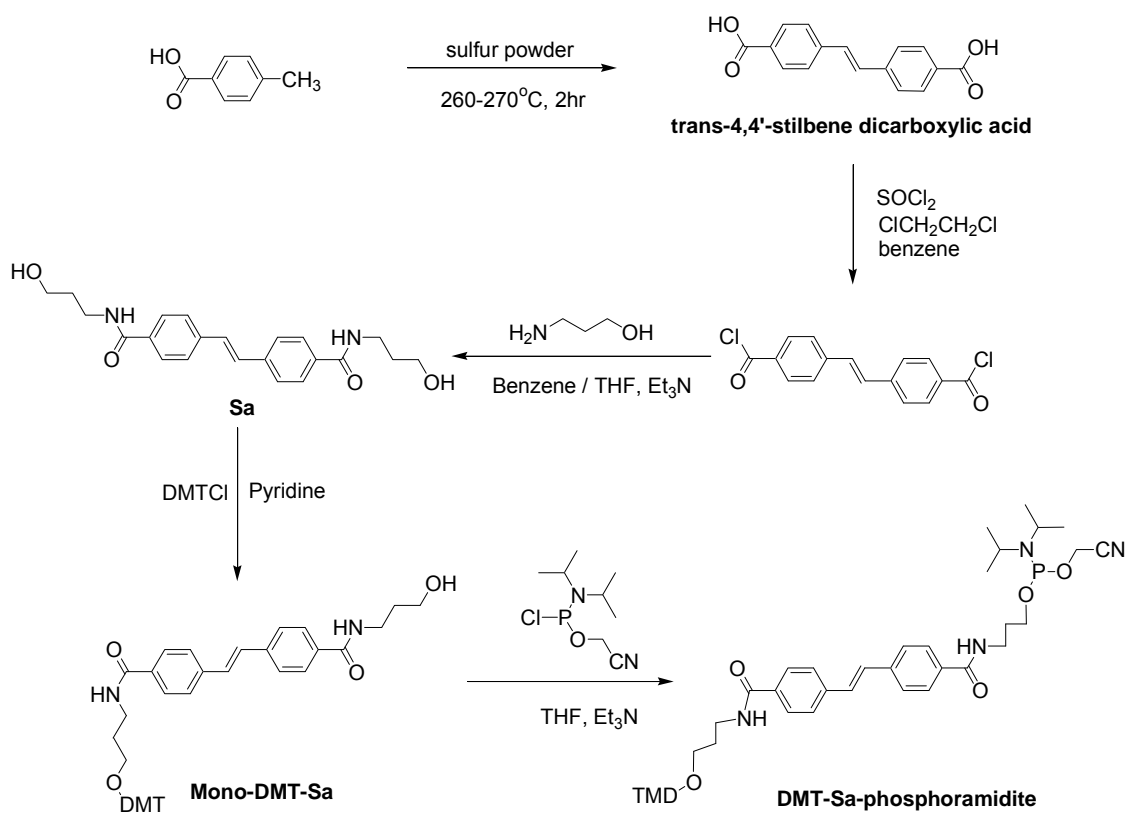
Nanosecond Transient Absorption Spectra. Nanosecond transient spectra were recorded by Dr. Vladimir Shafirovich in New York University. The transient absorption spectra and kinetics of the radical ions were monitored directly using a fully-computerized kinetic spectrometer system (\sim 7 ns response time). A 355 nm nanosecond Nd-YAG (Continuum Surelite II) laser pulses (\sim 6 ns pulse width, 10 Hz repetition rate, \sim 10 mJ pulse⁻¹ cm⁻²) was used as the excitation source. The sample excitation frequency was reduced to 1 Hz by an electromechanical shutter and used to excite sample solutions (0.25 mL) of the oligonucleotides saturated with

argon. The transient absorbance was probed along a 1 cm optical path by light from a pulsed 75 W xenon arc lamp with its light beam oriented perpendicular to the laser beam. The signal was recorded by a Tektronix TDS 5052 oscilloscope operating in its high resolution mode. Satisfactory signal/noise ratios were obtained even after a single laser shot.

6.3 Chemical synthesis

6.3.1 Synthesis of *trans-N, N'*-bis(3-hydroxypropyl)stilbene-4,4'-dicarboxamide (Sa) linker and corresponding phosphoramidite

The preparation of phosphoramidite of *trans-N, N'*-bis(3-hydroxypropyl)stilbene-4,4'-dicarboxamide is described in Scheme 6.1. *trans*-4,4'-stilbene dicarboxylic acid was synthesized from toluic acid via free radical reaction at high temperature,¹ and then transferred to phosphoramidite product following the procedure of Letsinger and Wu.²



Scheme 6.1 Synthesis outline of *trans*-4,4'-stilbene dicarboxylic acid, stilbenedicarboxamide diol (Sa) and phosphoramidite.

***trans*-4,4'-stilbene dicarboxylic acid.** A mixture of 4-toluic acid (100 g, 0.74 mol) and sulphur powers (11.8 g, 0.36 mol) was placed in a 1-litre flask, and stirred and heated on a sand bath between 260 and 280 °C for 2 h. After the resultant mixture was cooled to about 140 °C, and hot xylene (400 mL) was added. With an air condenser, the mixture was boiled under reflux for 30 min., then filtered hot. The collected solid was boiled with dioxane (150 mL) for 30 min., then filtered, washed with hot dioxane (100 mL) and dried under vacuum, resulting a crude dicarboxylic acid as a yellow powder. The crude product was boiled in a solution of potassium hydroxide (14.0 g) in water (600 mL). The dissolved solution was concentrated to 200 mL and crystallized to yellow plates as dipotassium salt. The dipotassium salt was boiled in water (500 mL), and then neutralized by adding conc. HCl (30 mL). The precipitate was washed with water and dried under reduced pressure to give a yellow powder as the final product of *trans*-4,4'-stilbene dicarboxylic acid (13.5g, yield 28%)

***trans*-N, N'-bis(3-hydroxypropyl)stilbene- 4,4'-dicarboxamide (Sa).** A suspension of approximately 1g *trans*-4,4'-stilbene dicarboxylic acid and 100 mg benzyl triethyl ammonium chloride in 40 ml anhydrous 1,2-dichloroethane and 20 ml anhydrous benzene was heated and refluxed for 1.5 h under N₂. Then 2ml thionyl chloride was added slowly. The reaction mixture was refluxed overnight, then cooled to room temperature. Removal of solvent via vacuum distillation yielded 4,4'-stilbene dicarboxylic chloride as yellow-brown solid.

About 30 ml anhydrous benzene and 40 ml anhydrous tetrahydrofuran were added to the 4,4'-stilbene dicarboxylic chloride and the resulting slurry was slowly added into a well-stirred

clear solution of 3-aminopropanol (0.7 ml), anhydrous triethylamine (4ml, Fischer) and anhydrous methanol (27 ml) at 0 °C. The mixture was stirred overnight at room temperature under N₂ and a white suspension was obtained. The solvent was removed by rotavap. The resulting solid was collected and washed with water and methanol to give 1.03g light yellow product of **Sa**, with a yield of 78%. ¹H NMR (DMSO-d₆, ppm) δ 1.68 (m, 4H), 3.45 (m, 4H), 4.49 (t, 2H), 7.42 (s, 2H), 7.72 (d, 4H), 7.84 (d, 4H), 8.46 (m, 2H).

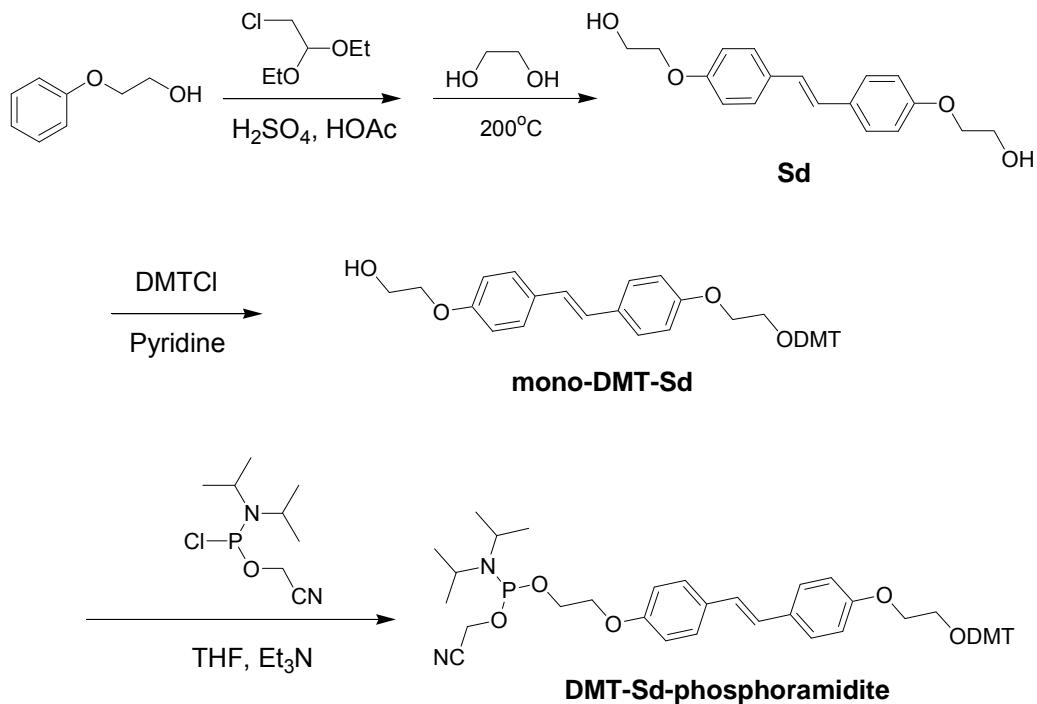
Mono-4,4'-dimethoxytrityl protected Sa (Mono-DMT-Sa) Suspension solution of 180 mg **Sa** in 20 ml anhydrous pyridine was heated and refluxed until the mixture turned to yellow clear solution. A red solution of 215 mg dimethoxytrityl chloride in 5 ml anhydrous pyridine was slowly added to the mixture under N₂. The reaction mixture was stirred and allowed to cool to room temperature. After 3h stirring at room temperature, TLC (CHCl₃: MeOH = 20:1 plus 5% triethylamine) indicated three fluorescent spots: starting **Sa**, mono-DMT-Sa and bis-DMT-Sa. The mixture was poured into 20 ml saturated NaHCO₃ solution. Ethyl acetate was used to extract the mixture three times. The organic layers were collected, dried using anhydrous sodium sulfate and concentrated via rotavap. The yellow crude product was dissolved and purified by silica gel column using 20:1 CHCl₃/MeOH, plus 5% triethylamine eluent. A white solid product, Mono-DMT-Sa, was collected with a yield in the range of 20-50%.

Phosphoramidite of mono-4,4'-dimethoxytrityl protected stilbenedicarboxamide (DMT-Sa-phosphoramidite) 150 mg mono-DMT-Sa was dissolved in 5 ml anhydrous tetrahydrofuran, and 200 μl anhydrous diisopropylethylamine was then added, followed by the

addition of 100 μ l 2-cyanoethyl diisopropylchloro-phosphoramidite under N_2 . The reaction was complete at room temperature within an hour. The R_f value of the product was around 0.56 on TLC (ethyl acetate plus 5% triethylamine). Ethyl acetate (30 ml, pretreated with saturated $NaHCO_3$) was then poured to the reaction mixture following by the addition of 5 ml saturated $NaHCO_3$ solution. The aqueous layer was washed with ethyl acetate twice and the organic layers were combined, dried by sodium sulfate, and concentrated via rotavap. The residue was purified by silica gel column chromatography (ethyl acetate, 5% triethylamine). The collected eluent was dried on vacuum line for 2 to 3 hr to give a white solid, compound of DMT-SA-phosphoramidite, with a yield of 50-70%. ^{31}P NMR ($CDCl_3$, H_3PO_4 as external standard, ppm): δ 149.87

6.3.2 Synthesis of *trans*-bis(2-hydroxyethyl)stilbene-4,4'-diether (Sd) linker and corresponding phosphoramidite

The preparation of phosphoramidite of *trans*-bis(2-hydroxyethyl)stilbene-4,4'-diether is described in Scheme 6.2. *trans*-bis(2-hydroxyethyl)stilbene-4,4'-diether (Sd) was prepared by the method of Sieber,³ and transferred to phosphoramidite product following the procedure of Letsinger and Wu.²



Scheme 6.2 Synthesis outline of *trans*-bis(2-hydroxyethyl)stilbene-4,4'-diether (Sd), mono-DMT-Sd and DMT-Sd-phosphoramidite.

***trans*-bis(2-hydroxyethyl)stilbene-4,4'-diether (Sd).** 20 mmol 2-phenoxyethanol and 10 mmol chloroacetaldehyde diethyl acetal was dissolved in 4 ml acetic acid and kept in ice-water bath. Pre-ice-cooled 1:1 acetic acid and sulfuric acid was added slowly, while stirring. The reaction mixture was stirred at 0-4 °C for 6 hr and then at room temperature overnight. R_f value of the product on TLC (1:5 CHCl₃ and ethyl acetate) plate is about 0.7. The fluid was poured on ice and extracted with ether thrice. Organic layer was collected, washed with saturated Na₂CO₃ solution, dried over anhydrous Na₂SO₄, and concentrated via rotavap. 15 ml ethylene glycol was added to the colorless residue and the mixture in a vacuum distillation glassware set-up was heated in 170-250 °C sand bath for 50 min and then cooled to room temperature. Small amount

of distillate came out at 90 °C and after cooled to room temperature a large amount of white solid was observed. The solvent was removed via vacuum filtration, and the solid was recrystallized in pyridine (~35% yield). ¹H NMR (DMSO-d₆, ppm): δ 3.55 (m, 4H), 4.04 (t, 4H), 4.56 (t, 2H), 6.91 (d, 4H), 7.02 (s, 2H), 7.48 (d, 4H).

Mono-4,4'-dimethoxytrityl protected Sd (mono-DMT-Sd) similar preparation procedure as described in 6.3.1 for mono-DMT-Sa. The R_f value for mono-DMT-Sd is 0.3 (4:6 hexane / ethyl acetate) on TLC. Mono-DMT-Sd was collected as white solid, with a yield range of 25-40%. ¹H NMR (CDCl₃, ppm): δ 3.43 (t, 2H), 3.8 (s, 6H), 3.95 (t, 2H), 4.15 (m, 4H), 6.82 (d, 4H), 6.92 (m, 6H), 7.2-7.5 (m, 13H).

Phosphoramidite of mono-4,4'-dimethoxytrityl protected stilbenediether (DMT-Sd-phosphoramidite). The preparation of DMT-Sd-phosphoramidite was conducted as the procedure of DMT-Sa-phosphoramidite. The product was obtained as a white solid (yield 50-70%). ¹H NMR (CDCl₃, ppm): δ 1.2 (d, 12H), 2.6 (t, 2H), 3.45 (t, 2H), 3.65 (m, 2H), 3.80 (s, 6H), 4.18 (m, 4H), 6.90 (m, 10H), 7.2-7.5 (m, 13 H); ³¹P NMR (CDCl₃, H₃PO₄ as external standard, ppm): δ 149.87

6.3.3 Synthesis the phosphoramidite of pyrenebutanol

100 mg pyrenebutanol was dissolved in 5.2 ml anhydrous THF, and 200 µl anhydrous diisopropylethylamine was then added, followed by the addition of 100 µl 2-cyanoethyl diisopropylchloro-phosphoramidite under N₂. The reaction was complete at room temperature

within an hour. The R_f value of the product was around 0.7 on TLC (1:4 of hexane / ethyl acetate plus 5% triethylamine). Ethyl acetate (30 ml, pretreated with saturated NaHCO_3) was then poured to the reaction mixture following by the addition of 5 ml saturated NaHCO_3 solution. The aqueous layer was washed with ethyl acetate twice and the organic layers were combined, dried by sodium sulfate, and concentrated via rotavap. The residue was purified by silica gel column chromatography (1:4 of hexane / ethyl acetate plus 5% triethylamine). The collected eluent was dried on vacuum line for 2 to 3 hr to give a white solid, compound of phosphoramidite of pyrenebutanol, with a yield range of 80-90%. ^{31}P NMR (CDCl_3 , H_3PO_4 as external standard, ppm): δ 148.369

6.4 Solid phase phosphoramidite oligonucleotide synthesis and sample purification

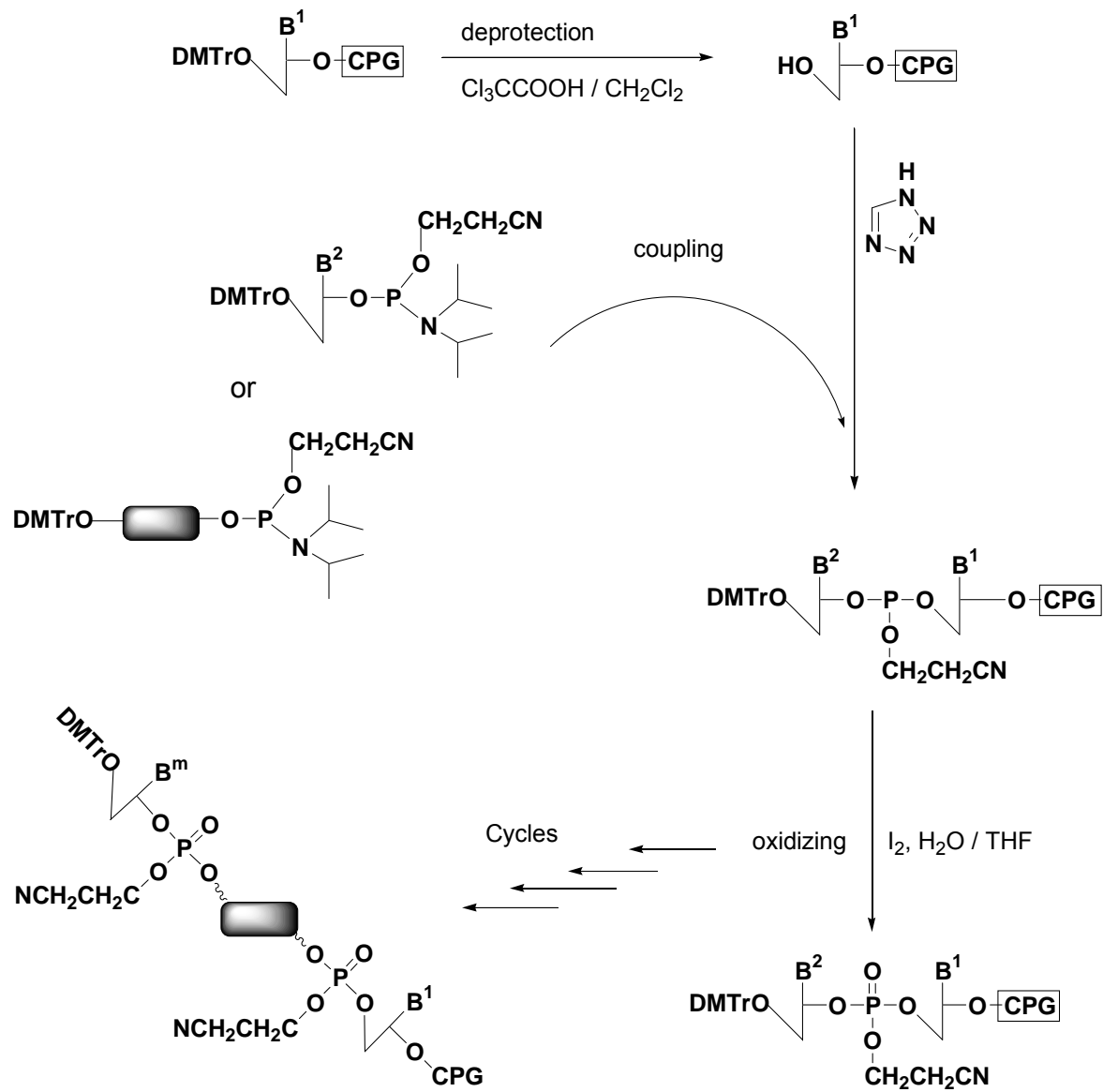
6.4.1 General synthesis and purification

The conventional β -cyanoethyl phosphoramidite solid phase oligonucleotide synthesis is outlined in Scheme 6.3. All oligonucleotide-chromophore conjugates in this work were prepared by automated solid phase synthesis carried on Millipore Expedite nucleic acid synthesizer on a 1 μmole scale. The sequences containing only natural bases or inosine (I) and chromophore were synthesized using standard solid phase synthesis methods and reagents. But for sequences containing 7-deazaguanine (Z) base, a milder oxidizing reagent and a modified procedure were used. Instead of the routinely used oxidizing reagent (I_2 in water and THF), 1 g 10-camphorsulphonyl oxaziridine dissolved in 10 ml anhydrous acetonitrile was used as the

oxidant. A longer oxidation time (180 s compared to standard 10 s) was also used.

In all the cases, the 4,4'-dimethoxytrityl (DMT) protecting group at 5' end of oligonucleotides was retained during auto solid phase synthesis. The DMT group increases the retention time in RP-HPLC and thus help the purification of oligonucleotides. After solid phase synthesis, the CPG was treated with 1 ml concentrated ammonium hydroxide at 55 °C for 17 hr or at room temperature for 24 hr. Removal of NH₃ was accomplished by using N₂ bubbling. The ammonium hydroxide not only cleaved the oligonucleotide from the solid support but also removed the protecting groups on nucleobases. Pure water was added to rinse the solid support and dissolve the crude oligonucleotides. The mixture was filtered through a 0.2 µm syringe filter (Waterman) and about 1 to 1.5 ml solution was collected, ready for RP-HPLC purification.

An analytical injection of the synthetic oligonucleotide on RP-HPLC was run first to locate the target peak, and then preparative injections accomplished the purification. The collected eluent from the target peaks were first dried by Speedvac (Savant speed vac SC 100 and refrigerated condensation trap RT 100), and then detritylated using 80% acetic acid/water solution for 30 min at room temperature. After this reaction, the acetic acid was completely removed by Speedvac and 1 ml pure water was added. The solution was extracted by ethyl ether for trice, while the organic layers were disposed and the aqueous layer was dried by Speedvac. The deprotected sample was analyzed by RP-HPLC. A second HPLC purification was carried out as needed.



Scheme 6.3 Conventional 3' DNA solid phase synthesis.

6.4.2 Treatment of G-rich sequences

Protecting groups on G-rich sequences have been observed to be robust under general ammonium treatment. Experience has found that increasing deprotection time or deprotection temperature (55 °C) provides high yields.

6.5 Characterization of DNA conjugates

6.5.1 General procedure

Characterization of samples was carried out via MALDI-TOF mass spectrometry. The MALDI-TOF mass spectrometry matrix was a 8:1 mixture of 0.3 M aqueous ammonium citrate solution and 0.1 M 2',4',6'-trihydroxyacetophenone in 1:1 CH₃CN: H₂O. DNA samples were mixed with the matrix in a 1:1 (v/v) ratio. The mixture (1 µL) was spotted on the MALDI-TOF MS sample plate. The sample plate was dried under N₂ flow, and analyzed by MALDI-TOF mass spectrometry.

6.5.2 3-hydroxypicolinic acid (3-HPA) matrix

G-rich sequences have been observed to form adduct product with one of matrix components, 2',4',6'-trihydroxyacetophenone. Therefore alternative matrix has been used. Mixture of 0.3 M 3-hydroxypicolinic acid (3-HPA) and 3 mM ammonium citrate tribasic has been tried and observed with decreased adduct peak of target molecules with components of matrix.

References

Chapter 1

1. Blackburn, G. M.; Gait, M. J.; Loakes, D.; Williams, D. M., *Nucleic acids in chemistry and biology* Royal Society of Chemistry: Oxford, UK, **2006**.
2. Shabarova, Z.; Bogdanov, A., *Advanced organic chemistry of nucleic acids* 1st ed.; John Wiley & Sons: New York, **1994**.
3. Stevens, A.; Grossman, L.; Kivie, M., Demonstration of DNA-dependent amino acid incorporation. *Methods in Enzymology* **1968**, *12*, 791-794.
4. Nisman, B.; Lawrence Grossman and Kivie, M., Techniques for demonstrating DNA-dependent protein synthesis. In *Methods in Enzymology*, Academic Press: 1968; Vol. Volume 12, Part 2, pp 794-820.
5. Ezziane, Z., DNA computing: applications and challenges. *Nanotechnology* **2006**, *17*, R27-R29.
6. Roelfes, G.; Feringa, B. L., DNA-based asymmetric catalysis. *Angew. Chem. Int. Ed.* **2005**, *44*, 3230-3232.
7. Sherman, W. B.; Seeman, N. C., A precisely controlled DNA biped walking device. *Nano Lett.* **2004**, *4*, 1203-1207.
8. Steckl, A. J., DNA - a new material for photonics? *Nature Photonics* **2007**, *1*, 3-5.
9. Vogtle, F., *Cyclophane chemistry: Synthesis, structures and reactions*. John Wiley & Sons: New York, **1993**.
10. Eley, D. D.; Spivey, D. I. T., Semiconductivity of organic substances. Part 9.—Nucleic acid in the dry state. *Trans. Faraday Soc.* **1962**, *58*, 411-415.
11. Murphy, C. J.; Arkin, M. R.; Ghatlia, N. D.; Bossmann, S.; Turro, N. J.; Barton, J. K., Fast photoinduced electron transfer through DNA Intercalation. *Proc. Natl. Acad. Sci. U.S.A.* **1994**, *91*, 5315-5319.
12. Murphy, C. J.; Arkin, M. R.; Jenkins, Y.; Ghatlia, N. D.; Bossmann, S. H.; Turro, N. J.; Barton, J. K., Long-range photoinduced electron transfer through a DNA helix. *Science* **1993**,

262, 1025-1029.

13. Turro, N. J.; Barton, J. K., Paradigms, supermolecules, electron transfer and chemistry at a distance. What's the problem? The science or the paradigm? *J. Biol. Inorg. Chem.* **1998**, *3*, 201-209.
14. Heelis, P. F.; Hartman, R. F.; Rose, S. D., Photoenzymic repair of UV-damaged DNA: a chemist's perspective. *Chem. Soc. Rev.* **1995**, *24*, 289-297.
15. Sancar, A., Structure and function of DNA photolyase. *Biochemistry* **1994**, *33*, 2-9.
16. Jortner, J.; Bixon, M.; Langenbacher, T.; Michel-Beyerle, M. E., Charge transfer and transport in DNA. *Proc. Natl. Acad. Sci. U.S.A.* **1998**, *95*, 12759-12765.
17. Hecht, S. M., *Bioorganic Chemistry: Nucleic Acids*. Oxford Univ. Press **1996**.
18. Drew, H. R.; Wing, R. M.; Takano, T.; Broka, C.; Tanaka, S.; Itakura, K.; Dickerson, R. E., Structure of a B-DNA dodecamer: Conformation and dynamics. *Proc. Natl. Acad. Sci. U.S.A.* **1981**, *78*, 2179-2183.
19. Salunkhe, M.; Wu, T.; Letsinger, R. L., Control of folding and binding of oligonucleotides by use of a nonnucleotide linker. *J. Am. Chem. Soc.* **1992**, *114*, 8768-8772.
20. Laughlan G.; Murchie A. I, N. D. G. M. M. H. M. P. C. L. D. M. L. B., The high-resolution crystal structure of a parallel-stranded guanine tetraplex. *Science* **1994**, *265*, 520-524.
21. Williamson, J. R., *Annu. Rev. Biophys. Biomol. Struct.* **1994**, *23*, 703-730.
22. Zahler, A. M.; Williamson, J. R.; Cech, T. R.; Prescott, D. M., Inhibition of telomerase by G-quartet DNA structures. *Nature* **1991**, *350*, 718-720.
23. Yu, G-L.; Bradley, J. D.; Attardi, L. D.; Blackburn, E. H., In vivo alteration of telomere sequences and senescence caused by mutated Tetrahymena telomerase RNAs. *Nature* **1990**, *344*, 126-132.
24. Siddiqui-Jain, A.; Grand, C. L.; Bearss, D. J.; Hurley, L. H., Direct evidence for a G-quadruplex in a promoter region and its targeting with a small molecule to repress c-MYC transcription. *Proc. Natl. Acad. Sci. U.S.A.* **2002**, *99*, 11593-11598.
25. Tauchi, T.; Shin-ya, K.; Sashida, G.; Sumi, M.; Nakajima, A.; Shimamoto, T.; Ohyashiki, J.

- H.; Ohyashiki, K., Activity of a novel G-quadruplex-interactive telomerase inhibitor, telomestatin (SOT-095), against human leukemia cells: involvement of ATM-dependent DNA damage response pathways. *Nature: Oncogene* **2003**, *22*, 5338-5347.
26. Shammas, M. A.; Shmookler Reis, R. J.; Akiyama, M.; Koley, H.; Chauhan, D.; Hideshima, T.; Goyal, R. K.; Hurley, L. H.; Anderson, K. C.; Munshi, N. C., Telomerase inhibition and cell growth arrest by G-quadruplex interactive agent in multiple myeloma. *Mol. Cancer Ther.* **2003**, *2*, 825-833.
27. Jing, N.; Hogan, M. E., Structure-activity of tetrad-forming oligonucleotides as a potent anti-HIV therapeutic drug. *J. Biol. Chem.* **1998**, *273*, 34992-34999.
28. Davis, J. T.; Spada, G. P., Supramolecular architectures generated by self-assembly of guanosine derivatives. *Chem. Soc. Rev.* **2007**, *36*, 296-313.
29. Gubala, V.; Betancourt, J. E.; Rivera, J. M., Expanding the hoogsteen edge of 2'-deoxyguanosine: Consequences for G-quadruplex formation. *Org. Lett.* **2004**, *6*, 4735-4738.
30. Nagatoishi, S.; Nojima, T.; Galezowska, E.; Juskowiak, B.; Takenaka, S., G quadruplex-based FRET Probes with the Thrombin-Binding Aptamer (TBA) Sequence Designed for the Efficient Fluorometric Detection of the Potassium Ion. *ChemBioChem* **2006**, *7*, 1730-1737.
31. Rinaldi, R.; Maruccio, G.; Biasco, A.; Arima, V.; Cingolani, R.; Giorgi, T.; Masiero, S.; Spada, G. P.; Gottarelli, G., Hybrid molecular electronic devices based on modified deoxyguanosines. *Nanotechnology* **2002**, *13*, 398-403.
32. Wang, Y.; Patel, D. J., Guanine residues in d(T2AG3) and d(T2G4) form parallel-stranded potassium cation stabilized G-quadruplexes with anti-glycosidic torsion angles in solution. *Biochemistry* **1992**, *31*, 8112-8119.
33. Phillips, K.; Dauter, Z.; Murchie, A. I. H.; Lilley, D. M. J.; Luisi, B., The crystal structure of a parallel-stranded guanine tetraplex at 0.95Å resolution. *Journal of Molecular Biology* **1997**, *273*, 171-182.
34. Han, H.; Langley, D. R.; Rangan, A.; Hurley, L. H., Selective interactions of cationic porphyrins with G-quadruplex structures. *J. Am. Chem. Soc.* **2001**, *123*, 8902-8913.
35. Wang, Y.; Patel, D. J., Solution structure of the human telomeric repeat d[AG3(T2AG3)3] G-tetraplex. *Structure* **1993**, *1*, 263-282.

36. Haider, S.; Parkinson, G. N.; Neidle, S., Crystal structure of the potassium form of an oxytricha nova G-quadruplex. *J. Mol. Biol.* **2002**, *320*, 189-200.
37. Schultze, P.; Smith, F. W.; Feigon, J., Refined solution structure of the dimeric quadruplex formed from the Oxytricha telomeric oligonucleotide d(GGGGTTTTGGGG). *Structure* **1994**, *2*, 221-233.
38. Kang, C.; Zhang, X.; Ratliff, R.; Moyzis, R.; Rich, A., Crystal structure of four-stranded Oxytricha telomeric DNA. *Nature* **1992**, *356*, 126-131.
39. Schultze, P.; Macaya, R. F.; Feigon, J., Three-dimensional solution structure of the thrombin-binding DNA aptamer d(GGTTGGTGTGGTTGG). *J. Mol. Biol.* **1994**, *235*, 1532-1547.
40. Neidle, S., *Oxford handbook of nucleic acid structure*. Oxford Univ. Press: Oxford, UK, **1999**.
41. Callis, P. R., Electronic states and luminescence of nucleic acid systems. *Ann. Rev. Phys. Chem.* **1983**, *34*, 329-357.
42. Malone, R. J.; Miller, A. M.; Kohler, B., Singlet excited-state lifetimes of cytosine derivatives measured by femtosecond transient absorption. *Photochem. Photobiol.* **2003**, *77*, 158-164.
43. Gustavsson, T.; Sarkar, N.; Lazzarotto, E.; Markovitsi, D.; Improta, R., Singlet excited state dynamics of uracil and thymine derivatives: A femtosecond fluorescence upconversion study in acetonitrile. *Chem. Phys. Lett.* **2006**, *429*, 551-557.
44. Kohler, B., Symposium-in-print: DNA photodynamics introduction. *Photochem. Photobiol.* **2007**, *83*, 592-594.
45. Pecourt, J. M. L.; Peon, J.; Kohler, B., Ultrafast internal conversion of electronically excited RNA and DNA nucleosides in water. *J. Am. Chem. Soc.* **2000**, *122*, 9348-9349.
46. Georghiou, S.; Ababneh, A. In *Dynamics and solvation of DNA from intrinsic fluorescence studies*, American Physical Society, Ann. APS Mar Meeting, , Indianapolis, IN, **2002**; Indianapolis, IN, 2002.
47. Schreier, W. J.; Schrader, T. E.; Koller, F. O.; Gilch, P.; Crespo-Hernandez, C. E.; Swaminathan, V. N.; Carell, T.; Zinth, W.; Kohler, B., Thymine dimerization in DNA is an

ultrafast photoreaction. *Science* **2007**, *315*, 625-629.

48. Canuel, C.; Mons, M.; Piuze, F.; Tardivel, B.; Dimicoli, I.; Elhanine, M., Excited states dynamics of DNA and RNA bases: Characterization of a stepwise deactivation pathway in the gas phase. *J. Chem. Phys.* **2005**, *122*, 074316-074322.

49. Lewis, F. D.; Zhang, L.; Liu, X.; Zuo, X.; Tiede, D. M.; Long, H.; Schatz, G. C., DNA as helical ruler: Exciton-coupled circular dichroism in DNA conjugates. *J. Am. Chem. Soc.* **2005**, *127*, 14445-14453.

50. Parkinson, G. N.; Lee, M. P. H.; Neidle, S., Crystal structure of parallel quadruplexes from human telomeric DNA. *Nature* **2002**, *417*, 876-880.

51. Wang, K. Y.; Krawczyk, S. H.; Bischofberger, N.; Swaminathan, S.; Bolton, P. H., The tertiary structure of a DNA aptamer which binds to and inhibits thrombin determines activity. *Biochemistry* **1993**, *32*, 11285-11292.

52. Phan, A. T.; Patel, D. J., Two-repeat human telomeric d(TAGGGTTAGGGT) sequence forms interconverting parallel and antiparallel G-quadruplexes in solution: Distinct topologies, thermodynamic properties, and folding / unfolding kinetics. *J. Am. Chem. Soc.* **2003**, *125*, 15021-15027.

53. Rujan, I. N.; Meleney, J. C.; Bolton, P. H., Vertebrate telomere repeat DNAs favor external loop propeller quadruplex structures in the presence of high concentrations of potassium. *Nucl. Acids Res.* **2005**, *33*, 2022-2031.

54. Seidel, C. A. M.; Schulz, A.; Sauer, M. H. M., Nucleobase-specific quenching of fluorescent dyes. 1. nucleobase one-electron redox potentials and their correlation with static and dynamic quenching efficiencies. *J. Phys. Chem.* **1996**, *100*, 5541-5553.

55. Steenken, S.; Telo, J. P.; Novais, H. M.; Candeias, L. P., One-electron-reduction potentials of pyrimidine bases, nucleosides, and nucleotides in aqueous solution. Consequences for DNA redox chemistry. *J. Am. Chem. Soc.* **1992**, *114*, 4701-4709.

56. Saito, I.; Takayama, M.; Sugiyama, H.; Nakatani, K.; Tsuchida, A.; Yamamoto, M., Photoinduced DNA cleavage via electron transfer: Demonstration that guanine residues located 5' to guanine are the most electron-donating sites. *J. Am. Chem. Soc.* **1995**, *117*, 6406-6407.

57. Sugiyama, H.; Saito, I., Theoretical Studies of GG-Specific Photocleavage of DNA via Electron Transfer: Significant Lowering of Ionization Potential and 5'-Localization of HOMO of

Stacked GG Bases in B-Form DNA. *J. Am. Chem. Soc.* **1996**, *118*, 7063-7068.

58. Yoshioka, Y.; Kitagawa, Y.; Takano, Y.; Yamaguchi, K.; Nakamura, T.; Saito, I., Experimental and theoretical studies on the selectivity of GGG triplets toward one-electron oxidation in B-form DNA. *J. Am. Chem. Soc.* **1999**, *121*, 8712-8719.

59. Sonntag, C. V., *The chemical basis of radiation biology* Taylor & Francis: London, **1987**.

60. Hieda, K., DNA damage induced by vacuum and soft X-ray photons from synchrotron radiation. *Int. J. Radiat. Biol.* **1994**, *66*, 561-567.

61. Spothem-Maurizot, M.; Charlier, M.; Sabattier, R., DNA radiolysis by fast neutrons. *Int. J. Radiat. Biol.* **1990**, *57*, 301-313.

62. Mambo, E.; Gao, X.; Cohen, Y.; Guo, Z.; Talalay, P.; Sidransky, D., Electrophile and oxidant damage of mitochondrial DNA leading to rapid evolution of homoplasmic mutations. *Proc. Natl. Acad. Sci. U.S.A.* **2003**, *100*, 1838-1843.

63. Shafirovich, V.; Geacintov, N. E., *Proton-coupled electron transfer reactions at a distance in DNA duplexes*. **2004**; p 129-158.

64. IUPAC Compendium of Chemical Terminology.
<http://www.iupac.org/goldbook/E02011.pdf>

65. Welinder, K. G.; Mikkelsen, L., The oxygen binding site of cytochrome oxidase : Structural predictions on subunit I from amino acid sequences. *FEBS Lett.* **1983**, *157*, 233-239.

66. Myllykallio, H.; Drepper, F.; Mathis, P.; Daldal, F., Electron-transfer supercomplexes in photosynthesis and respiration. *Trends in Microbiology* **2000**, *8*, 493-494.

67. Schiff, M.; Froissart, R.; Olsen, R. K. J.; Acquaviva, C.; Vianey-Saban, C., Electron transfer flavoprotein deficiency: Functional and molecular aspects. *Mol. Gen. Metabol.* **2006**, *88*, 153-158.

68. Koopman, W. J. H.; Verkaart, S.; Visch, H.-J.; van der Westhuizen, F. H.; Murphy, M. P.; van den Heuvel, L. W. P. J.; Smeitink, J. A. M.; Willems, P. H. G. M., Inhibition of complex I of the electron transport chain causes O₂⁻ mediated mitochondrial outgrowth. *Am. J. Physiol. Cell Physiol.* **2005**, *288*, C1440-1450.

69. Weller, A., *Zeit. Phys. Chem. Neue. Folg.* **1982**, *133*, 93-98.

70. Balzani, V., *Electron transfer in chemistry*. WILEY-VCH: Weinheim, Germany, **2001**; Vol. 3.
71. Jortner, J.; Bixon, M.; Langenbacher, T.; Michel-Beyerle, M. E., Charge transfer and transport in DNA. *Proc. Natl. Acad. Sci. U.S.A.* **1998**, *95*, 12759-12765.
72. Katz, J. I.; Jortner, J.; Choi, S.; Rice, S. A., On excess electron and hole band structures and carrier mobility in naphthalene, anthracene, and several polyphenyls. *J. Chem. Phys.* **1963**, *39*, 1683-1697.
73. Pope, M.; Swenberg, C. E., *Electronic processes in organic crystals* Clarendon, Oxford, **1982**.
74. Simon, J.; André, J.-J., *Molecular semiconductors* Springer: Berlin, **1985**.
75. Bixon, M.; Giese, B.; Wessely, S.; Langenbacher, T.; Michel-Beyerle, M. E.; Jortner, J., Long-range charge hopping in DNA. *Proc. Natl. Acad. Sci. U.S.A.* **1999**, *96*, 11713-11716.
76. Brun, A. M.; Harriman, A., Dynamics of electron transfer between intercalated polycyclic molecules: effect of interspersed bases. *J. Am. Chem. Soc.* **1992**, *114*, 3656-3660.
77. Lewis, F. D.; Wu, T.; Zhang, Y.; Letsinger, R. L.; Greenfield, S. R.; Wasielewski, M. R., Distance-dependent electron transfer in DNA hairpins. *Science* **1997**, *277*, 673-676.
78. Fukui, K.; Tanaka, K., Distance dependence of photoinduced electron transfer in DNA. *Angew. Chem. Int. Ed.* **1998**, *37*, 158-161.
79. Ly, D.; Kan, Y.; Armitage, B.; Schuster, G. B., Cleavage of DNA by irradiation of substituted anthraquinones: Intercalation promotes electron transfer and efficient reaction at GG steps. *J. Am. Chem. Soc.* **1996**, *118*, 8747-8748.
80. Breslin, D. T.; Schuster, G. B., Anthraquinone photonucleases: Mechanisms for GG-selective and nonselective cleavage of double-stranded DNA. *J. Am. Chem. Soc.* **1996**, *118*, 2311-2319.
81. Dandliker, P. J.; Nunez, M. E.; Barton, J. K., Oxidative charge transfer to repair thymine dimers and damage guanine bases in DNA assemblies containing tethered metallointercalators. *Biochemistry* **1998**, *37*, 6491-6502.
82. Dandliker, P. J.; Holmlin, R. E.; Barton, J. K., Oxidative thymine dimer repair in the DNA helix. *Science* **1997**, *275*, 1465-1468.

83. Holmlin, R. E.; Dandliker, P. J.; Barton, J. K., Charge transfer through the DNA base stack. *Angew. Chem. Int. Ed.* **1997**, *36*, 2714-2730.

Chapter 2

1. Voityuk, A. A., Estimates of electronic coupling for excess electron transfer in DNA. *J. Chem. Phys.* **2005**, *123*, 34903-34905.

2. Murphy, C. J.; Arkin, M. R.; Ghatlia, N. D.; Bossmann, S.; Turro, N. J.; Barton, J. K., Fast photoinduced electron transfer through DNA intercalation. *Proc. Natl. Acad. Sci. U.S.A.* **1994**, *91*, 5315-5319.

3. Arkin, M. R.; Stemp, E. D. A.; Holmlin, R. E.; Barton, J. K.; Hormann, A.; Olson, E. J. C.; Barbara, P. F., Rates of DNA-mediated electron transfer between metallointercalators. *Science* **1996**, *273*, 475-480.

4. Benn, R.; Mynott, R.; Topalovic, I.; Scott, F., Fluxionality of (β -2-naphthalene)(iso-Pr₂P(CH₂)_n-iso-Pr₂P)Ni⁰ (n = 2,3) in the solid state and solution as studied by CP/MAS and 2D carbon-13 NMR spectroscopy. *Organometallics* **1989**, *8*, 2299-2305.

5. Scott, F.; Kruger, C.; Betz, P., Preparation of new nickel(0) naphthalene complexes, crystal structure of [Ni(C₁₀H₈)(i-C₃H₇)₂PCH₂CH₂P(i-C₃H₇)₂]. *J. Organomet. Chem.* **1990**, *387*, 113-121.

6. Stanger, A.; Weismann, H., Inter- vs. intramolecular rearrangement of a (Bu₃)₂ Ni moiety in its 9-alkyl and 9,10-dialkyl anthracene complexes. Limiting conditions and isomer stabilities. *J. Organomet. Chem.* **1996**, *515*, 183-191.

7. Meade, J. T.; Kayyem, F. J., Electron transfer through DNA: Site-specific modification of duplex DNA with ruthenium donors and acceptors. *Angew. Chem. Int. Ed.* **1995**, *34*, 352-354.

8. Lewis, F. D.; Wu, T.; Zhang, Y.; Letsinger, R. L.; Greenfield, S. R.; Wasielewski, M. R., Distance-dependent electron transfer in DNA hairpins. *Science* **1997**, *277*, 673-676.

9. Lewis, F. D.; Liu, X.; Miller, S. E.; Wasielewski, M. R., Electronic interactions between stacked DNA base pairs and diphenylacetylene-4,4'-dicarboxamide in hairpin DNA. *J. Am. Chem. Soc.* **1999**, *121*, 9746-9747.

10. Lewis, F. D.; Liu, X.; Wu, Y.; Miller, S. E.; Wasielewski, M. R.; Letsinger, R. L.; Sanishvili,

- R.; Joachimiak, A.; Tereshko, V.; Egli, M., Structure and photoinduced electron transfer in exceptionally stable synthetic DNA hairpins with stilbenediether linkers. *J. Am. Chem. Soc.* **1999**, *121*, 9905-9906.
11. Lewis, F. D.; Wu, T.; Liu, X.; Letsinger, R. L.; Greenfield, S. R.; Miller, S. E.; Wasielewski, M. R., Dynamics of photoinduced charge separation and charge recombination in synthetic DNA hairpins with stilbenedicarboxamide linkers. *J. Am. Chem. Soc.* **2000**, *122*, 2889-2902.
12. Lewis, F. D.; Kalgutkar, R. S.; Wu, Y.; Liu, X.; Liu, J.; Hayes, R. T.; Miller, S. E.; Wasielewski, M. R., Driving force dependence of electron transfer dynamics in synthetic DNA hairpins. *J. Am. Chem. Soc.* **2000**, *122*, 12346-12351.
13. Egli, M.; Tereshko, V.; Mushudov, G. N.; Sanishvili, R.; Liu, X.; Lewis, F. D., Face-to-face and edge-to-face π - π interactions in a synthetic DNA hairpin with a stilbenediether linker. *J. Am. Chem. Soc.* **2003**, *125*, 10842-10849.
14. Letsinger, R. L.; Wu, T., Use of a stilbenedicarboxamide bridge in stabilizing, monitoring, and photochemically altering folded conformations of oligonucleotides. *J. Am. Chem. Soc.* **1995**, *117*, 7323-7328.
15. Fukui, K.; Tanaka, K., Distance dependence of photoinduced electron transfer in DNA. *Angew. Chem. Int. Ed.* **1998**, *37*, 158-161.
16. Davis, W. B.; Naydenova, I.; Haselsberger, R.; Ogrodnik, A.; Giese, B.; Michel-Beyerle, M. E., Dynamics of hole trapping by G, GG, and GGG in DNA. *Angew. Chem. Int. Ed.* **2000**, *39*, 3649-3652.
17. Hess, S.; Gotz, M.; Davis, W. B.; Michel-Beyerle, M. E., On the apparently anomalous distance dependence of charge-transfer rates in 9-amino-6-chloro-2-methoxyacridine-modified DNA. *J. Am. Chem. Soc.* **2001**, *123*, 10046-10055.
18. William 燭. Davis, I. N. R. H. A. O. B. G. M. M.-B., Dynamics of Hole Trapping by G, GG, and GGG in DNA. *Angewandte Chemie* **2000**, *39*, 3649-3652.
19. Wan, C.; Fiebig, T.; Schiemann, O.; Barton, J. K.; Zewail, A. H., Femtosecond direct observation of charge transfer between bases in DNA. *Proc. Natl. Acad. Sci. U.S.A.* **2000**, *97*, 14052-14055.
20. Kelley, S. O.; Barton, J. K., Electron transfer between bases in double helical DNA. *Science* **1999**, *283*, 375-381.

21. Wan, C.; Fiebig, T.; Kelley, S. O.; Treadway, C. R.; Barton, J. K.; Zewail, A. H., Femtosecond dynamics of DNA-mediated electron transfer. *Proc. Natl. Acad. Sci. U.S.A.* **1999**, *96*, 6014-6019.
22. Jortner, J.; Bixon, M.; Langenbacher, T.; Michel-Beyerle, M. E., Charge transfer and transport in DNA. *Proc. Natl. Acad. Sci. U.S.A.* **1998**, *95*, 12759-12765.
23. Felts, A. K.; Pollard, W. T.; Friesner, R. A., Multilevel redfield treatment of bridge-mediated long-range electron transfer: A mechanism for anomalous distance dependence. *J. Phys. Chem.* **1995**, *99*, 2929-2940.
24. Okada, T.; Migita, M.; Mataga, N.; Sakata, Y.; Misumi, S., Picosecond laser spectroscopy of intramolecular heteroexcimer systems. Time-resolved absorption studies of p-(CH₃)₂NC₆H₄(CH₂)_{n-1}-pyrenyl and 9-anthryl systems. *J. Am. Chem. Soc.* **1981**, *103*, 4715-4720.
25. Grozema, F.; Berlin, Y.; Siebbeles, L. D. A., Mechanism of charge migration through DNA: Molecular wire behavior, single-step tunneling or hopping? *J. Am. Chem. Soc.* **2000**, *122*, 10903-10909.
26. Giese, B.; Amaudrut, J.; Kohler, A.-K.; Spormann, M.; Wessely, S., Direct observation of hole transfer through DNA by hopping between adenine bases and by tunnelling. *Nature* **2001**, *412*, 318-320.
27. Berlin, Y. A.; Burin, A. L.; Ratner, M. A., Elementary steps for charge transport in DNA: thermal activation vs. tunneling. *Chem. Phys.* **2002**, *275*, 61-74.
28. Jortner, J.; Bixon, M.; Voityuk, A. A.; Rosch, N., Superexchange mediated charge hopping in DNA. *J. Phys. Chem. A* **2002**, *106*, 7599-7606.
29. Bixon, M.; Jortner, J., Long-range and very long-range charge transport in DNA. *Chem. Phys.* **2002**, *281*, 393-408.
30. Khalaf, A. I.; Pitt, A. R.; Scobie, M.; Suckling, C. J.; Urwin, J.; Waigh, R. D.; Fishleigh, R. V.; Young, S. C.; Wylie, W. A., The synthesis of some head to head linked DNA minor groove binders. *Tetrahedron* **2000**, *56*, 5225-5239.
31. Lewis, F. D.; Wu, Y.; Liu, X., Synthesis, structure, and photochemistry of exceptionally stable synthetic DNA hairpins with stilbene diether linkers. *J. Am. Chem. Soc.* **2002**, *124*, 12165-12173.

32. Lewis, F. D.; Wasielewski, M. R., Dynamics of photoinitiated hole and electron injection in duplex DNA. In *Charge Transfer in DNA*, Wagenknecht, H.-A., Ed. Wiley-VCH: Weinheim, Germany, **2005**.
33. Lewis, F. D.; Wu, T.; Burch, E. L.; Bassani, D. M.; Yang, J.-S.; Schneider, S.; Jaeger, W.; Letsinger, R. L., Hybrid oligonucleotides containing stilbene units. Excimer fluorescence and photodimerization. *J. Am. Chem. Soc.* **1995**, *117*, 8785-8792.
34. Lewis, F. D.; Liu, X.; Miller, S. E.; Hayes, R. T.; Wasielewski, M. R., Dynamics of electron injection in DNA hairpins. *J. Am. Chem. Soc.* **2002**, *124*, 11280-11281.
35. Lewis, F. D.; Wu, Y.; Zhang, L.; Zuo, X.; Hayes, R. T.; Wasielewski, M. R., DNA-mediated exciton coupling and electron transfer between donor and acceptor stilbenes separated by a variable number of base pairs. *J. Am. Chem. Soc.* **2004**, *126*, 8206-8215.
36. Lewis, F. D.; Zhu, H.; Daublain, P.; Fiebig, T.; Raytchev, M.; Wang, Q.; Shafirovich, V., Crossover from superexchange to hopping as the mechanism for photoinduced charge transfer in DNA hairpin conjugates. *J. Am. Chem. Soc.* **2006**, *128*, 791-800.
37. Frederick D. Lewis, Y. W. R. T. H. M. R. W., DNA-Mediated Electron Transfer across Synthetic T:A?T Triplex Structures. *Angewandte Chemie International Edition* **2002**, *41*, 3485-3487.
38. Mataga, N.; Nishikawa, S.; Asahi, T.; Okada, T., Femtosecond-picosecond laser photolysis studies on the photoinduced charge separation and charge recombination of a produced ion pair state of some typical intramolecular exciplex compounds in alkanenitrile solvents. *J. Phys. Chem.* **1990**, *94*, 1443-1447.
39. Gould, I. R.; Farid, S., Dynamics of bimolecular photoinduced electron-transfer reactions. *Acc. Chem. Res.* **1996**, *29*, 522-528.
40. Oevering, H.; Paddon-Row, M. N.; Heppener, M.; Oliver, A. M.; Cotsaris, E.; Verhoeven, J. W.; Hush, N. S., Long-range photoinduced through-bond electron transfer and radiative recombination via rigid nonconjugated bridges: distance and solvent dependence. *J. Am. Chem. Soc.* **1987**, *109*, 3258-3269.
41. Gould, I. R.; Young, R. H.; Mueller, L. J.; Albrecht, A. C.; Farid, S., Electronic structures of exciplexes and excited charge-transfer complexes. *J. Am. Chem. Soc.* **1994**, *116*, 8188-8199.
42. Lor, M.; Thielemans, J.; Viaene, L.; Cotlet, M.; Hofkens, J.; Weil, T.; Hampel, C.; Mullen,

- K.; Verhoeven, J. W.; Van der Auweraer, M.; De Schryver, F. C., Photoinduced electron transfer in a rigid first generation triphenylamine core dendrimer substituted with a peryleneimide acceptor. *J. Am. Chem. Soc.* **2002**, *124*, 9918-9925.
43. Rachofsky, E. L.; Osman, R.; Ross, J. B. A., Probing structure and dynamics of DNA with 2-aminopurine: Effects of local environment on fluorescence. *Biochemistry* **2001**, *40*, 946-956.
44. Lewis, F. D.; Zhang, L.; Liu, X.; Zuo, X.; Tiede, D. M.; Long, H.; Schatz, G. C., DNA as helical ruler: Exciton-coupled circular dichroism in DNA conjugates. *J. Am. Chem. Soc.* **2005**, *127*, 14445-14453.
45. Conwell, E. M., Charge transport in DNA in solution: The role of polarons. *Proc. Natl. Acad. Sci. U.S.A.* **2005**, *102*, 8795-8799.
46. Conwell, E. M.; Rakhmanova, S. V., Polarons in DNA. *Proc. Natl. Acad. Sci. U.S.A.* **2000**, *97*, 4556-4560.
47. Barnett, R. N.; Cleveland, C. L.; Joy, A.; Landman, U.; Schuster, G. B., Charge migration in DNA: Ion-gated transport. *Science* **2001**, *294*, 567-571.
48. Renger, T.; Marcus, R. A., Variable-range hopping electron transfer through disordered bridge states: Application to DNA. *J. Phys. Chem. A* **2003**, *107*, 8404-8419.
49. Seidel, C. A. M.; Schulz, A.; Sauer, M. H. M., Nucleobase-specific quenching of fluorescent dyes. 1. Nucleobase one-electron redox potentials and their correlation with static and dynamic quenching efficiencies. *J. Phys. Chem.* **1996**, *100*, 5541-5553.
50. Lewis, F. D.; Wasielewski, M. R., Dynamics and equilibrium for single step hole transport processes in duplex DNA. In *Topics in Current Chemistry*, **2004**; Vol. 236, pp 45-65.
51. Fiebig, T.; Wan, C.; Zewail, A. H., Femtosecond charge transfer dynamics of a modified DNA base: 2-aminopurine in complexes with nucleotides. *ChemPhysChem* **2002**, *3*, 781-788.
52. Nadeau, J. G.; Crothers, D. M., Structural basis for DNA bending. *Proc. Natl. Acad. Sci. U.S.A.* **1989**, *86*, 2622-2626.
53. Takada, T.; Kawai, K.; Cai, X.; Sugimoto, A.; Fujitsuka, M.; Majima, T., Charge separation in DNA via consecutive adenine hopping. *J. Am. Chem. Soc.* **2004**, *126*, 1125-1129.
54. Pope, M.; Swenberg, C. E., *Electronic processes in organic crystals and polymers* Oxford

University Press: Oxford, **1999**.

55. van de Craats, A. M.; Warman, J. M.; de Haas, M. P.; Adam, D.; Simmerer, J.; Haarer, D.; Schuhmacher, P., The mobility of charge carriers in all four phases of the columnar discotic material hexakis(hexylthio)triphenylene: Combined TOF and PR-TRMC results. *Adv. Mater.* **1996**, *8*, 823-826.
56. van de Craats, A. M.; Warman, J. M., The core-size effect on the mobility of charge in discotic liquid crystalline materials. *Adv. Mater.* **2001**, *13*, 130-133.
57. Grozema, F. C.; Siebbeles, L. D. A.; Berlin, Y. A.; Ratner, M. A., Hole mobility in DNA: Effects of static and dynamic structural fluctuations. *ChemPhysChem* **2002**, *3*, 536-539.
58. Basko, D. M.; Conwell, E. M., Effect of solvation on hole motion in DNA. *Phys. Rev. Lett.* **2002**, *88*, 098102-098106.
59. Gray, H. B.; Winkler, J. R., In *Electron Transfer in Chemistry*, Balzani, V., Ed. Wiley-VCH: Weinheim, Vol. 3, pp 3-23.
60. Shafirovich, V.; Dourandin, A.; Huang, W.; Luneva, N. P.; Geacintov, N. E., Electron transfer at a distance induced by site-selective photoionization of 2-aminopurine in oligonucleotides and investigated by transient absorption techniques. *Phys. Chem. Chem. Phys.* **2000**, *2*, 4399-4408.
61. Shafirovich, V.; Geacintov, Q. N. E., In *Top. Curr. Chem.*, **2004**; Vol. 237, pp 129-157.
62. Shafirovich, V.; Geacintov, N. E., In *Charge transfer in DNA*, Wagenknecht, H.-A., Ed. Wiley-VCH: **2005**; pp 175-196.
63. Takada, T.; Kawai, K.; Fujitsuka, M.; Majima, T., Direct observation of hole transfer through double-helical DNA over 100 Å. *Proc. Natl. Acad. Sci. U.S.A.* **2004**, *101*, 14002-14006.
64. Abdel Malak, R.; Gao, Z.; Wishart, J. F.; Isied, S. S., Long-range electron transfer across peptide bridges: The transition from electron superexchange to hopping. *J. Am. Chem. Soc.* **2004**, *126*, 13888-13889.
65. Paulson, B. P.; Miller, J. R.; Gan, W. X.; Closs, G., Superexchange and sequential mechanisms in charge transfer with a mediating state between the donor and acceptor. *J. Am. Chem. Soc.* **2005**, *127*, 4860-4868.

66. Lewis, F. D.; Liu, X.; Liu, J.; Hayes, R. T.; Wasielewski, M. R., Dynamics and equilibria for oxidation of G, GG, and GGG sequences in DNA hairpins. *J. Am. Chem. Soc.* **2000**, *122*, 12037-12038.
67. Lewis, F. D.; Liu, J.; Liu, X.; Zuo, X.; Hayes, R. T.; Wasielewski, M. R., Dynamics and energetics of hole trapping in DNA by 7-deazaguanine. *Angew. Chem. Int. Ed.* **2002**, *41*, 1026-1028.
68. Lewis, F. D.; Liu, J.; Weigel, W.; Rettig, W.; Kurnikov, I. V.; Beratan, D. N., Donor-bridge-acceptor energetics determine the distance dependence of electron tunneling in DNA. *Proc. Natl. Acad. Sci. U.S.A.* **2002**, *99*, 12536-12541.
69. Lewis, F. D.; Liu, X.; Miller, S. E.; Hayes, R. T.; Wasielewski, M. R., Formation and decay of localized contact radical ion pairs in DNA hairpins. *J. Am. Chem. Soc.* **2002**, *124*, 14020-14026.

Chapter 3

1. Marini, J. C.; Levene, S. D.; Crothers, D. M.; Englund, P. T., Bent helical structure in kinetoplast DNA. *Proc. Natl. Acad. Sci. U.S.A.* **1982**, *79*, 7664-7668.
2. Augustyn, K. E.; Wojtuszewski, K.; Hawkins, M. E.; Knutson, J. R.; Mukerji, I., Examination of the premelting transition of DNA A-tracts using a fluorescent adenosine analogue. *Biochemistry* **2006**, *45*, 5039-5047.
3. Dewey, T. G.; Turner, D. H., Laser temperature-jump study of stacking in adenylic acid polymers. *Biochemistry* **1979**, *18*, 5757-5762.
4. Meena; Sun, Z.; Mulligan, C.; McLaughlin, L. W., Removal of a single minor-groove functional group eliminates A-tract curvature. *J. Am. Chem. Soc.* **2006**, *128*, 11756-11757.
5. Schuster, G. B., Ed., The mechanism of long-distance radical cation transport in duplex DNA: Ion-gated hopping of polaron-like distortions. In *Long-Range Charge Transfer in DNA*, Springer-Verlag: Berlin, **2004**.
6. Crespo-Hernandez, C. E.; Cohen, B.; Hare, P. M.; Kohler, B., Ultrafast excited-state dynamics in nucleic acids. *Chem. Rev.* **2004**, *104*, 1977-2020.

7. Buchvarov, I.; Wang, Q.; Raytchev, M.; Trifonov, A.; Fiebig, T., Electronic energy delocalization and dissipation in single- and double-stranded DNA. *Proc. Natl. Acad. Sci. U.S.A.* **2007**, *104*, 4794-4797.
8. Salunkhe, M.; Wu, T.; Letsinger, R. L., Control of folding and binding of oligonucleotides by use of a nonnucleotide linker. *J. Am. Chem. Soc.* **1992**, *114*, 8768-8772.
9. Melnikova, V. O.; Ananthaswamy, H. N., Cellular and molecular events leading to the development of skin cancer. *Mutation Research-Fundamental and Molecular Mechanisms of Mutagenesis* **2005**, *571*, 91-106.
10. Schreier, W. J.; Schrader, T. E.; Koller, F. O.; Gilch, P.; Crespo-Hernandez, C. E.; Swaminathan, V. N.; Carell, T.; Zinth, W.; Kohler, B., Thymine dimerization in DNA is an ultrafast photoreaction. *Science* **2007**, *315*, 625-629.
11. Lewis, F. D.; Wu, Y.; Liu, X., Synthesis, structure, and photochemistry of exceptionally stable synthetic DNA hairpins with stilbene diether linkers. *J. Am. Chem. Soc.* **2002**, *124*, 12165-12173.
12. Durand, M.; Chevrie, K.; Chassignol, M.; Thuong, N. T.; Maurizot, J. C., Circular dichroism studies of an oligodeoxyribonucleotide containing a hairpin loop made of a hexaethylene glycol chain: conformation and stability. *Nucl. Acids Res.* **1990**, *18*, 6353-6359.
13. Rumney, S.; Kool, E. T., Structural optimization of non-nucleotide loop replacements for duplex and triplex DNAs. *J. Am. Chem. Soc.* **1995**, *117*, 5635-5646.
14. Letsinger, R. L.; Wu, T., Use of a stilbenedicarboxamide bridge in stabilizing, monitoring, and photochemically altering folded conformations of oligonucleotides. *J. Am. Chem. Soc.* **1995**, *117*, 7323-7328.
15. Arnott, S.; Campbell-Smith, P. J.; Chandrasekaran, R., Atomic Coordinates and Molecular Conformations for DNA-DNA, RNA-RNA, and DNA-RNA Helices;. In *Handbook of Biochemistry and Molecular Biology*, 3rd ed.; CRC Press: Cleveland, OH, **1976**; pp 411-422.
16. Cornell, W. D.; Cieplak, P.; Bayly, C. I.; Gould, I. R.; Merz, K. M.; Ferguson, D. M.; Spellmeyer, D. C.; Fox, T.; Caldwell, J. W.; Kollman, P. A., A secondgeneration force field for the simulation of proteins, nucleic acids, and organic molecules. *J. Am. Chem. Soc.* **1996**, *118*, 2309-2309.
17. Breslauer, K. J., Extracting thermodynamic data from equilibrium melting curves for

oligonucleotide order-disorder transitions. In *Protocols for oligonucleotide conjugates: Synthesis and analytical techniques* Agrawal, S., Ed. Humana Press: Totowa, NY, **1994**.

18. *Oligo analyzer*, 3.0; Intergrated DNA Technologies: Caralville, IA.

19. Landolt-Bornstein. In *Numerical data and functional relationships in science and technology*, Madelung, O., Ed. Springer-Verlag: Berlin, Vol. 1, p 15.

20. Guckian, K. M.; Schweitzer, B. A.; Ren, R. X. F.; Sheils, C. J.; Tahmassebi, D. C.; Kool, E. T., Factors contributing to aromatic stacking in water: evaluation in the context of DNA. *J. Am. Chem. Soc.* **2000**, *122*, 2213-2222.

21. Pohorille, A.; Ross, W. S.; Tinoco, I. J. R., DNA dynamics in aqueous solution: opening the double helix. *Int. J. High Performance Comput. Appl.* **1990**, *4*, 81-96.

22. Lam, S. L.; Ip, L. N., Low temperature solution structures and base pair stacking of souble helical d(CGTACG)₂. *J. Biomol. Struct. Dyn.* **2002**, *19*, 907-917.

23. Priyakumar, U. D.; MacKerell, A. D., NMR Imino proton exchange experiments on duplex DNA primarily monitor the opening of purine bases. *J. Am. Chem. Soc.* **2006**, *128*, 678-679.

24. Andreatta, D.; Sen, S.; PerezLustres, J. L.; Kovalenko, S. A.; Ernsting, N. P.; Murphy, C. J.; Coleman, R. S.; Berg, M. A., Ultrafast dynamics in DNA: "Fraying" at the end of the helix. *J. Am. Chem. Soc.* **2006**, *128*, 6885-6892.

Chapter 4

1. Henderson, E.; Hardin, C. C.; Walk, S. K.; Tinoco, I.; Blackburn, E. H., Telomeric DNA oligonucleotides form novel intramolecular structures containing guanine-guanine base pairs. *Cell* **1987**, *51*, 899-908.

2. Haider, S.; Parkinson, G. N.; Read, M. A.; Neidle, S., Design and analysis of G4 recognition compounds. In *Small Molecule DNA and RNA Binders*, Demeunynck, M.; Bailly, C.; Wilson, W. D., Eds. **2004**; pp 337-359.

3. Zahler, A. M.; Williamson, J. R.; Cech, T. R.; Prescott, D. M., Inhibition of telomerase by G-quartet DNA structures. *Nature* **1991**, *350*, 718-720.

4. Walsh, K.; Gualberto, A., MyoD binds to the guanine tetrad nucleic acid structure. *J. Biol. Chem.* **1992**, *267*, 13714-13718.
5. Liu, Z.; Frantz, J. D.; Gilbert, W.; Tye, B., Identification and characterization of a nuclease activity specific for G4 tetrastranded DNA. *Proc. Natl. Acad. Sci. U.S.A.* **1993**, *90*, 3157-3161.
6. Arimondo, P. B.; Riou, J.-F.; Mergny, J.-L.; Tazi, J.; Sun, J.-S.; Garestier, T.; Helene, C., Interaction of human DNA topoisomerase I with G-quartet structures. *Nucl. Acids Res.* **2000**, *28*, 4832-4838.
7. Fry, M.; Loeb, L. A., Human werner syndrome DNA helicase unwinds tetrahelical structures of the fragile X syndrome repeat sequence d(CGG)_n. *J. Biol. Chem.* **1999**, *274*, 12797-12802.
8. Sen, D.; Gilbert, W., Formation of parallel four-stranded complexes by guanine-rich motifs in DNA and its implications for meiosis. *Nature* **1988**, *334*, 364-366.
9. Anuradha, S.; Muniyappa, K., Meiosis-specific yeast Hop1 protein promotes synapsis of double-stranded DNA helices via the formation of guanine quartets. *Nucl. Acids Res.* **2004**, *32*, 2378-2385.
10. Winnik, F. M., Photophysics of preassociated pyrenes in aqueous polymer solutions and in other organized media. *Chem. Rev.* **1993**, *93*, 587-614.
11. Klessinger, M.; Michl, J., *Excited states and photochemistry of organic molecules*. VCH: New York, **1995**.
12. Hrdlicka, P. J.; Babu, B. R.; Sorensen, M. D.; Harrit, N.; Wengel, J., Multilabeled pyrene-functionalized 2'-amino-LNA probes for nucleic acid detection in homogeneous fluorescence assays. *J. Am. Chem. Soc.* **2005**, *127*, 13293-13299.
13. Kawai, K.; Yoshida, H.; Takada, T.; Tojo, S.; Majima, T., Formation of pyrene dimer radical cation at the internal site of oligodeoxynucleotides. *J. Phys. Chem. B* **2004**, *108*, 13547-13550.
14. Langenegger, S. M.; Haner, R., Excimer formation by interstrand stacked pyrenes. *Chem. Comm.* **2004**, 2792-2793.
15. Paris, P. L.; Langenhan, J. M.; Kool, E. T., Probing DNA sequences in solution with a monomer-excimer fluorescence color change. *Nucl. Acids Res.* **1998**, *26*, 3789-3793.
16. Mohammadi, S.; Slama-Schwok, A.; Leger, G.; El Manouni, D.; Shchyolkina, A.; Leroux, Y.;

- Taillandier, E., Triple helix formation and homologous strand exchange in pyrene-labeled oligonucleotides. *Biochemistry* **1997**, *36*, 14836-14844.
17. Rippe, K.; Fritsch, V.; Westhof, E.; Jovin, T. M., Alternating d(G-A) sequences form a parallel-stranded DNA homoduplex. *EMBO J.* **1992**, *11*, 3777-3786.
18. Nagatoishi, S.; Nojima, T.; Juskowiak, B.; Takenaka, S., A pyrene-labeled G-quadruplex oligonucleotide as a fluorescent probe for potassium ion detection in biological applications. *Angew. Chem. Int. Ed.* **2005**, *44*, 5067-5070.
19. Jin, R.; Gaffney, B. L.; Wang, C.; Jones, R. A.; Breslauer, K. J., Thermodynamics and structure of a DNA tetraplex: A spectroscopic and calorimetric study of the tetramolecular complexes of d(TG₃T) and d(TG₃T₂G₃T). *Proc. Natl. Acad. Sci. U.S.A.* **1992**, *89*, 8832-8836.
20. Wyatt, J. R.; Davis, P. W.; Freier, S. M., Kinetics of G-quartet-mediated tetramer formation. *Biochemistry* **1996**, *35*, 8002-8008.
21. Max, K. A., Quadruplex structures in nucleic acids. *Biopolymers* **2001**, *56*, 123-146.
22. Lewis, F. D.; Wu, Y.; Zhang, L., Reversible formation of DNA G-quadruplex hairpin dimers from stilbenediether conjugates. *Chem. Comm.* **2004**, 636-637.
23. Oliviero, G.; Amato, J.; Borbone, N.; Galeone, A.; Petraccone, L.; Varra, M.; Piccialli, G.; Mayol, L., Synthesis and characterization of monomolecular DNA G-quadruplexes formed by tetra-end-linked oligonucleotides. *Bioconjugate Chem.* **2006**, *17*, 889-898.
24. Oliviero, G.; Amato, J.; Borbone, N.; Galeone, A.; Varra, M.; Piccialli, G.; Mayol, L., Unusual monomolecular DNA quadruplex structures using bunch-oligonucleotides. *Nucleosides Nucleic Acids* **2005**, *24*, 739 - 741.
25. Oliviero, G.; Borbone, N.; Galeone, A.; Varra, M.; Piccialli, G.; Mayol, L., Synthesis and characterization of a bunched oligonucleotide forming a monomolecular parallel quadruplex structure in solution. *Tetrahedron Lett.* **2004**, *45*, 4869-4872.
26. Strahan, G. D.; Keniry, M. A.; Shafer, R. H., NMR structure refinement and dynamics of the K⁺-[d(G₃T₄G₃)₂] quadruplex via particle mesh Ewald molecular dynamics simulations. *Biophys. J.* **1998**, *75*, 968-981.
27. Han, H.; Langley, D. R.; Rangan, A.; Hurley, L. H., Selective interactions of cationic porphyrins with G-quadruplex structures. *J. Am. Chem. Soc.* **2001**, *123*, 8902-8913.

28. Kang, C.; Zhang, X.; Ratliff, R.; Moyzis, R.; Rich, A., Crystal structure of four-stranded Oxytricha telomeric DNA. *Nature* **1992**, *356*, 126-131.
29. Chowdhury, S.; Bansal, M., A nanosecond molecular dynamics study of antiparallel d(G)₇ quadruplex structures: Effect of the coordinated cations *J. Biomol. Struct. Dyn.* **2001**, *18*, 647-669.
30. Noskov, S. Y.; Berneche, S.; Roux, B., Control of ion selectivity in potassium channels by electrostatic and dynamic properties of carbonyl ligands. *Nature* **2004**, *431*, 830-834.
31. Merkina, E. E.; Fox, K. R., Kinetic stability of intermolecular DNA quadruplexes. *Biophys. J.* **2005**, *89*, 365-373.
32. Clark, G. R.; Pytel, P. D.; Squire, C. J.; Neidle, S., Structure of the first parallel DNA quadruplex-drug complex. *J. Am. Chem. Soc.* **2003**, *125*, 4066-4067.
33. Cuppoletti, A.; Cho, Y.; Park, J. S.; Strassler, C.; Kool, E. T., Oligomeric fluorescent labels for DNA. *Bioconjugate Chem.* **2005**, *16*, 528-534.
34. Rujan, I. N.; Meleney, J. C.; Bolton, P. H., Vertebrate telomere repeat DNAs favor external loop propeller quadruplex structures in the presence of high concentrations of potassium. *Nucl. Acids Res.* **2005**, *33*, 2022-2031.
35. Wong, A.; Wu, G., Selective binding of monovalent cations to the stacking G-quartet structure formed by guanosine 5'-monophosphate: A solid-state NMR study. *J. Am. Chem. Soc.* **2003**, *125*, 13895-13905.
36. Barbaric, J.; Wagenknecht, H.-A., DNA as a supramolecular scaffold for the helical arrangement of a stack of 1-ethynylpyrene chromophores. *Org. Biomol. Chem.* **2006**, *4*, 2088-2090.
37. Mayer-Enthart, E.; Wagenknecht, H.-A., Structure-sensitive and self-assembled helical pyrene array based on DNA architecture. *Angew. Chem. Int. Ed.* **2006**, *45*, 3372-3375.
38. Lewis, F. D.; Kurth, T. L., Intramolecular excimer fluorescence from folded ground state rotamers of N,N'-dimethyl-N,N'-dipyrenylurea protophanes. *Can. J. Chem.* **2003**, *81*, 770-776.
39. Risitano, A.; Fox, K. R., Influence of loop size on the stability of intramolecular DNA quadruplexes. *Nucl. Acids Res.* **2004**, *32*, 2598-2606.

40. Sen, D.; Gilbert, W., Guanine quartet structures. In *Methods in Enzymology*, David, M. J. L.; Dahlberg, J. E., Eds. Academic Press: **1992**; Vol. 211, pp 191-199.
41. Long, F. A.; McDevit, W. F., Activity coefficients of nonelectrolyte solutes in aqueous salt solutions. *Chem. Rev.* **1952**, *51*, 119-169.
42. Breslow, R., Hydrophobic effects on simple organic reactions in water. *Acc. Chem. Res.* **1991**, *24*, 159-164.

Chapter 5

1. Bock, L. C.; Griffin, L. C.; Latham, J. A.; Vermaas, E. H.; Toole, J. J., Selection of single-stranded DNA molecules that bind and inhibit human thrombin. *Nature* **1992**, *355*, 564-566.
2. Macaya, R. F.; Schultze, P.; Smith, F. W.; Roe, J. A.; Feigon, J., Thrombin-Binding DNA Aptamer Forms a Unimolecular Quadruplex Structure in Solution. *Proc. Natl. Acad. Sci. U.S.A.* **1993**, *90*, 3745-3749.
3. Schultze, P.; Macaya, R. F.; Feigon, J., Three-dimensional Solution Structure of the Thrombin-binding DNA Aptamer d(GGTTGGTGTGGTTGG). *J. Mol. Biol.* **1994**, *235*, 1532-1547.
4. Padmanabhan, K.; Padmanabhan, K. P.; Ferrara, J. D.; Sadler, J. E.; Tulinsky, A., The structure of alpha-thrombin inhibited by a 15-mer single-stranded DNA aptamer. *J. Biol. Chem.* **1993**, *268*, 17651-17654.
5. Wang, K. K. W., Therapeutic approaches with protease inhibitors in neurodegenerative and neurological diseases In *Role of Proteases in the Pathophysiology of Neurodegenerative Diseases*, Springer US: **2002**.
6. Toulon, P.; Frere, E.; Bachmeyer, C.; Candia, N.; Blanche, P.; Sereni, D.; Sicard, D., Fibrin polymerization defect in HIV-infected patients--evidence for a critical role of albumin in the prolongation of thrombin and reptilase clotting times. *Thromb-Haemost.* **1995**, *73*, 349-355
7. Macaya, R. F.; Waldron, J. A.; Beutel, B. A.; Gao, H.; Joesten, M. E.; Yang, M.; Patel, R.; Bertelsen, A. H.; Cook, A. F., Structural and Functional Characterization of Potent Antithrombotic Oligonucleotides Possessing Both Quadruplex and Duplex Motifs. *Biochemistry*

1995, 34, 4478-4492.

8. Tasset, D. M.; Kubik, M. F.; Steiner, W., Oligonucleotide inhibitors of human thrombin that bind distinct epitopes. *J. Mol. Biol.* **1997**, 272, 688-698.

9. Cherepanov, P.; Este, J. A.; Rando, R. F.; Ojwang, J. O.; Reekmans, G.; Steinfeld, R.; David, G.; De Clercq, E.; Debysers, Z., Mode of Interaction of G-Quartets with the Integrase of Human Immunodeficiency Virus Type 1. *Mol. Pharmacol.* **1997**, 52, 771-780.

10. Jing, N.; Xiong, W.; Guan, Y.; Pallansch, L.; Wang, S., Potassium-Dependent Folding: A Key to Intracellular Delivery of G-Quartet Oligonucleotides as HIV Inhibitors. *Biochemistry* **2002**, 41, 5397-5403.

11. Lin, Y.; Padmapriya, A.; Morden, K. M.; Jayasena, S. D., Peptide Conjugation to an in vitro-Selected DNA Ligand Improves Enzyme Inhibition. *Proc. Natl. Acad. Sci. U.S.A.* **1995**, 92, 11044-11048.

12. Harada, K.; Frankel, A. D., Identification of two novel arginine binding DNAs. *EMBO J.* **1995**, 14, 5798-5811.

13. Sumikura, K.; Yano, K.; Ikebukuro, K.; Karube, I., *Nucleic Acids Symp. Ser.* **1997**, 9, 257-258.

14. Smirnov, I.; Shafer, R. H., Effect of Loop Sequence and Size on DNA Aptamer Stability. *Biochemistry* **2000**, 39, 1462-1468.

15. Letsinger, R. L.; Wu, T., Use of a Stilbenedicarboxamide Bridge in Stabilizing, Monitoring, and Photochemically Altering Folded Conformations of Oligonucleotides. *J. Am. Chem. Soc.* **1995**, 117, 7323-7328.

16. Kumar, N.; Maiti, S., Quadruplex to Watson-Crick duplex transition of the thrombin binding aptamer: a fluorescence resonance energy transfer study. *Biochem. Biophys. Res. Commun.* **2004**, 319, 759-767.

17. Kang, C.; Zhang, X.; Ratliff, R.; Moyzis, R.; Rich, A., Crystal structure of four-stranded Oxytricha telomeric DNA. *Nature* **1992**, 356, 126-131.

18. Sacca, B.; Lacroix, L.; Mergny, J.-L., The effect of chemical modifications on the thermal stability of different G-quadruplex-forming oligonucleotides. *Nucl. Acids Res.* **2005**, 33, 1182-1192.

19. Mao, X.-A.; Gmeiner, W. H., NMR study of the folding-unfolding mechanism for the thrombin-binding DNA aptamer d(GGTTGGTGTGGTTGG). *Biophys. Chem.* **2005**, *113*, 155-160.

Chapter 6

1. Khalaf, A. I.; Pitt, A. R.; Scobie, M.; Suckling, C. J.; Urwin, J.; Waigh, R. D.; Fishleigh, R. V.; Young, S. C.; Wylie, W. A., The synthesis of some head to head linked DNA minor groove binders. *Tetrahedron* **2000**, *56*, 5225-5239.

2. Letsinger, R. L.; Wu, T., Use of a Stilbenedicarboxamide Bridge in Stabilizing, Monitoring, and Photochemically Altering Folded Conformations of Oligonucleotides. *J. Am. Chem. Soc.* **1995**, *117*, 7323-7328.

3. Sieber, R. H., *Liebigs Ann. Chem.* **1969**, *730*, 31-46.

Hairpins by Stilbene Capping of the Terminal Base Pairs, *J. Chin. Chem. Soc.*, **2006**, *53*, 1501-1507.

6. Jianguo Fang, Man Lu, Zhihua Chen, Huihe Zhu, Yan Li, Li Yang, Longmin Wu, and Zhongli Liu, Antioxidant Effects of Resveratrol and its Analogues against the Free Radical-Induced Peroxidation of Linoleic Acid in Micelles, *Chem. Eur. J.*, **2002**, *8*, 4191-4198.
7. Zhihua Chen, Bo Zhou, Huihe Zhu, Long-Min Wu, Li Yang, Zhong-Li Liu, Kinetic EPR study on reactions of vitamin E radicals, In *EPR in the 21st Century: Basics and Applications to Material, Life and Earth Sciences*, 1st ed.; Asako Kawamori, Jun Yamauchi, Hitoshi Ohta, Elsevier, Amsterdam, **2002**, 421-428.